Karlsruhe Institute of Technology

Best-Estimate Predictions through Consistent Experimental Data Assimilation: Methodology and Paradigm Reactor Physics Applications

Zur Erlangung des akademischen Grades

Doktor der Ingenieurwissenschaften

der Fakultät für Maschinenbau
Karlsruher Institut für Technologie (KIT)

genehmigte

Dissertation

von

Dipl.-Ing. Madalina Badea

Tag der mündlichen Prüfung:	03.11.2011
Hauptreferent:	Prof. Dr.Dr.h.c.mult. Dan G.Cacuci
Korreferent:	Prof. Dr.-Ing. E. Schnack

Best-Estimate Predictions through Consistent Experimental Data Assimilation: Methodology and Paradigm Reactor Physics Applications

Abstract

This work presents representative applications of a general mathematical framework for simultaneously calibrating model parameters and responses through the assimilation of experimental data, leading to "best-estimate" values with reduced uncertainties for both parameters and responses in a generic time-dependent system. This mathematical framework indicates the agreement between the computed and experimentally measured responses while performing: (i) simultaneous calibration of all parameters and responses; (ii) treatment of systems involving correlated parameters and responses; (iii) simultaneous calibration over all time intervals.

The salient features of the above methodology are highlighted by presenting a time-independent paradigm neutron diffusion problem and, respectively, a time-dependent radioactive decay problem, illustrating that the assimilation of consistent experimental information substantially reduces the uncertainties in the best estimate predictions for both model parameters and responses. This work also presents, in premiere, a large-scale application of assimilating experimental data from the OECD/NRC BWR Full-Size Fine-Mesh Bundle Tests (BFBT) benchmarks for the calibration of representative model parameters in the three-dimensional thermal-hydraulics code FLICA4, which is routinely used for the analysis and design of light-water reactors (LWR). The BFBT benchmarks were specifically designed by NUPEC to enable a systematic comparison between full-scale experimental data and predictions of numerical simulation models. In this work, the BFBT measurements are used for the calibration of model parameters in the thermal-hydraulics code FLICA4, for the following benchmark measurements: (i) pressure drops (steady one-dimensional simulations); (ii) axial void fractions distributions (transient one-dimensional simulations); and (iii) transversal void fraction distributions (steady three-dimensional simulations, at sub-channel level with cross-flows). By calibrating representative FLICA4-parameters, this work shows that the consistent assimilation of measurements reduces systematically uncertainties and improves in the predictions of large-scale thermal-hydraulics

codes. Further research is planned towards the consideration of multi-physics code systems comprising coupled thermal-hydraulics and reactor physics numerical simulation tools. Developing predictive experimentally validated “best-estimate” numerical models is particularly important for designing new technologies and facilities based on novel processes, while striving to avoid, as much as possible, the costly and lengthy procedures of building representative mock-up experiments, which might confirm -but would not necessarily explain- the predictions of simulation tools.

Kurzfassung

Diese Arbeit stellt den allgemeinen mathematischen Rahmen für das Kalibrieren von Modellparametern und Ergebnissen eines generischen zeitabhängigen Systems durch die Integration von experimentellen Daten, dar. Das Kalibrieren führt zu optimal geschätzten Werten mit reduzierten Unsicherheiten für Parameter und Ergebnisse.

Dieser mathematische Rahmen zeigt die Konsistenz zwischen den berechneten und experimentell gemessenen Ergebnissen bei: (i) gleichzeitigen Kalibrierung aller Parameter und Antworten; (ii) Behandlung von Systemen, die korrelierte Parameter und Antworten einschließen; (iii) gleichzeitigen Kalibrierung über allen Zeitintervallen, an.

Die wichtigsten Merkmale der oben genannten Methodologie sind hervorgehoben in ein zeitunabhängiges Paradigmenneutronendiffusionsproblem, und, beziehungsweise, ein zeitabhängiges Radioaktives-Zerfall Problem. Diese Beispiele zeigen wie die Integration von konsistenten experimentellen Informationen die Unsicherheiten für Parameter und Ergebnisse beträchtlich reduziert.

Diese Arbeit stellt auch das Kalibrieren, mit experimentellen Daten aus dem OECD/NRC BWR Fine-Mesh Bundle Tests (BFBT), von typischen Modellparametern im dreidimensionalen thermischen Hydraulikcode FLICA4 dar. FLICA4 ist ein Code welcher routinemäßig für die Analyse und das Design von Leichtwasserreaktoren (LWR) verwendet wird.

Die BFBT Experimenten wurden speziell von NUPEC dafür entworfen, um systematische Vergleiche zwischen experimentellen Daten und Voraussagen numerischer Simulationsmodellen zu ermöglichen. In dieser Arbeit werden die BFBT Messungen für die Kalibrierung von FLICA4-Parametern für die folgenden Fällen verwendet: (i) Druckabfälle; (ii) axiale Dampf-Bruchteile („Void-Fractions“) Verteilungen (zeitabhängige Simulationen); und (iii) transversalen Void-Fraction-Verteilungen (dreidimensionale Simulationen mit Kreuzströmungen).

Durch Kalibrierung von typischen FLICA4 Parametern zeigt diese Arbeit, dass die konsistente Integration von Messungen Unsicherheiten für Code-Parameter und Ergebnisse deutlich reduziert. Anschließende Forschung mit Multiphysik Codesystemen, welche die gekoppelte thermische Hydraulik und Reaktorphysik und numerische Simulationswerkzeuge umfassen, ist geplant.

TABLE OF CONTENTS

Introduction

Introduction

Repeated measurements of the same physical quantity yield values that differ from each other, as well as from the true but unknown value of that quantity. This variation in results is due to experimental errors, imperfect instruments, and imperfectly known calibration standards. Hence, around any reported experimental value, there always exists a range of values that may also be plausibly representative of the true value. In turn, this means that all inferences, predictions, engineering computations, and other applications of measured data are necessarily founded on weighted averages over all the possibly true values, with weights indicating the degree of plausibility of each value. Thus, since the true value of physical quantities cannot be measured exactly, nominally measured values are insufficient, by themselves, for applications; the quantitative uncertainties accompanying the measurements are also needed, along with the respective nominal values. Since the use of uncertain data may necessitate costly safety margins (in medicine, weather and climate prediction, or in the chemical, automotive, aerospace, or nuclear industries), working groups of the International Standards Organization have been developing uniform rules for reporting data uncertainties. Combination of data from different sources involves a weighted propagation (e.g., using sensitivities) of various uncertainties, requiring reasoning from incomplete information for extracting “best” values together with “best” uncertainties from often sparse, incomplete, error-afflicted, and occasionally discrepant experimental data.

The probabilistic description of possible future computational and experimental outcomes, based on all recognized errors and uncertainties, is the aim of predictive estimation. Predictive estimation comprises three key elements: model calibration, model extrapolation, and estimation of the validation domain. Model calibration involves the integration (assimilation) of new data for updating (i.e., “calibrating” or “adjusting”) the parameters characterizing a computational model. The procedures for model calibration must encompass the propagation of all relevant uncertainties, including:

(i) data uncertainties (input data, model parameters, initial and boundary conditions, forcing functions, etc);

(ii) numerical discretization errors;

(iii) discrepancies within the experimental data and/or discrepancies between data and model predictions; and

(iv) uncertainties in the physics of the modeled processes (e.g., due to incomplete knowledge).

The results of model calibration are best-estimated values for parameters and predicted responses, as well as best-estimate reduced uncertainties (i.e.,smaller values for the variance-covariance matrices of the predicted best-estimate parameters and responses, provided all elements involved in the calibration process are consistent with each other. Quantitative model extrapolation addresses the prediction of uncertainty in new environments or conditions of interest, including both untested parts of the parameter space and higher levels of system complexity in the validation hierarchy. Estimation of the validation domain addresses the estimation of contours of constant uncertainty in the high-dimensional space that characterizes the application of interest.

Perhaps the earliest systematic activities on finding best-estimate values for model parameters were initiated simultaneously in Europe [Cecchini et al, 1964], Israel [Humi et al, 1964], and the former Soviet Union [Usachhev, 1964], in the course of evaluating neutron cross sections by using time-independent reactor physics experiments for measuring “integral quantities” (also called “system responses”) such as reaction rates and multiplication factors. A decade later, these activities had reached conceptual maturity under the name of “cross-section adjustment” [see, e.g. Rowlands, 1973 and Gandini , 1973], which essentially amounted to using a weighted least-square procedure (with response sensitivities as weighting functions) for combining uncertainties in the model parameters with uncertainties in the experimental data, subject to the constraint imposed by the linearized reactor physics model. The resulting “adjusted” parameters and their “adjusted” uncertainties were then employed in the respective reactor physics model to predict better results (reaction rates, multiplication factors, Doppler coefficients) in an extended application domain (e.g., a new or improved reactor core design). By the late-1970s, the first-order response sensitivities, which appeared as weighting functions in the least squares adjustment procedure, were efficiently computed using adjoint neutron fluxes, as typified by the works of [Kuroi and Mitani, 1975, Dragt et al, 1977], and [Weisbin et al, 1978]. It is important to note that all of these works dealt with the time-independent linear neutron transport or diffusion equation, as encountered in reactor physics and shielding, for which the corresponding adjoint equations were already known and readily available. For nonlinear, time-dependent or stationary problems, the adjoint method for computing efficiently sensitivities was generally formulated in 1981 by [Cacuci, 1981] , while the first general formulation of a “data adjustment” like methodology for time-dependent nonlinear problems was presented in 1982 by [Barhen et al, 1982]. Regrettably, this advanced (for its time) data adjustment methodology stagnated in the field of nuclear engineering after 1982 and apparently failed to influence other scientific fields.

In the late 1980s and during the 1990s, the fundamental concepts underlying “data adjustment” seem to have been rediscovered while developing the so-called “data assimilation” procedure in the geophysical sciences, in that the concepts underlying data assimilation are the same as those underlying the (much older) “data adjustment” procedure. Since then, well over a thousand works on data assimilation have been published in the geophysical sciences alone, under the name of “3D-VAR” (for time-independent problems, and “4D-VAR” (for time-dependent problems). Although too numerous to cite extensively here, representative works can be found cited in the books by [Lewis et al, 2006, Lahoz et al, 2010, and Cacuci et al, 2011].

[Cacuci and Ionescu-Bujor, 2010] have recently published a comprehensive mathematical methodology for best-estimate predictions following the assimilation experimental data and simultaneous calibration of model parameters and responses, for large-scale nonlinear time-dependent systems. This methodology generalizes and significantly extends the results customarily used in nuclear engineering as well as those underlying 4D-VAR data assimilation procedures in the geophysical sciences [Lewis et al, 2006, Lahoz et al, 2010, and Cacuci et al, 2011]. This methodology also provides quantitative indicators constructed from sensitivity and covariance matrices for determining the consistency (agreement or disagreement) among the a priori computational and experimental data (parameters and responses). Once the inconsistent data, if any, is discarded, the methodology by [Cacuci and Ionescu-Bujor, 2010] yields best-estimate values for parameters and predicted responses, as well as best-estimate reduced uncertainties (i.e., “smaller” values for the variance-covariance matrices) for the predicted best-estimate parameters and responses.

[Petruzzi et al, 2010] have applied the methodology developed by [Cacuci and Ionescu-Bujor, 2010] to a blowdown thermal-hydraulics benchmark of interest to nuclear reactor safety, demonstrating that the assimilation of consistent experimental data leads to a significant reduction of uncertainties of the best estimate predicted results. Going significantly beyond the limited scope of the work by [Petruzzi et al, 2010], the present work presents a large-scale application of assimilating experimental data from the international OECD/NRC BWR Full-Size Fine-Mesh Bundle Tests (BFBT) benchmarks [Neykov et al., 2006] for the calibration of representative model parameters in the three-dimensional thermal-hydraulics code FLICA4 [Fillion et al., 2007]. This code is designed for the analysis of thermal-hydraulic phenomena in LWR cores.

This work is structured as follows: Section 2 reviews the methodology for data assimilation and simultaneous calibration of model parameters and responses, for a generic time-dependent physical system; of course, time independent systems are included as a particular case within this framework. This methodology also includes quantitative indicators (based on uncertainties and sensitivities) for determining the degree of agreement (or disagreement) relevant to the assimilation and best-estimate adjustment of parameters and responses, of computations and experiments. Furthermore, this methodology also provides the basic elements for quantitative model extrapolation (i.e., prediction of uncertainty in new environments or conditions of interest, including both untested parts of the parameter space and higher levels of system complexity in the validation hierarchy) and estimation of the validation domain.

Section 3 highlights the salient features of the above methodology by presenting a time-independent paradigm neutron diffusion problem and, respectively, a time-dependent radioactive decay problem. These problems clearly show that the assimilation of consistent experimental information substantially reduce the uncertainties in the best estimate predictions for both model parameters and responses. Section 3 also presents, in premiere, a large-scale application of assimilating experimental data from the OECD/NRC BWR Full-Size Fine-Mesh Bundle Tests (BFBT) benchmarks for the calibration of representative model parameters in the three-dimensional thermal-hydraulics code FLICA4. This code system has been designed by the Comissariat a l'Energie Atomique (France) and is routinely used for the analysis and design of light-water reactors (LWR). The BFBT benchmarks were specifically designed by NUPEC to enable a systematic comparison between full-scale experimental data and predictions of numerical simulation models. The BFBT experiments are particularly well suited for quantifying uncertainties in the prediction of detailed sub-channel void fraction distributions and critical powers. In this work, the BFBT measurements are used for the calibration of model parameters in the thermal-hydraulics code FLICA4, for the following benchmark measurements: (i) pressure drops (steady one-dimensional simulations); (ii) axial void fractions distributions (transient one-dimensional simulations); and (iii) transversal void fraction distributions (steady three-dimensional simulations, at sub-channel level with cross-flows).

Finally, Section 4 offers concluding remarks, addressing further work needed to alleviate the current limitations of the best-estimate predictive methodology presented in this work, as well as applications involving coupled thermal-hydraulics and reactor physics simulation tools.

1 Consistent Experimental Data Assimilation and Model Calibration: Mathemathical Formalism

This chapter presents a rigorous first-order methodology for computing best-estimate predictive results by combining experimental and computational information in conjunction with models of time-independent and time-dependent systems. This methodology uses Bayes' theorem in conjunction with information theory to assimilate consistently all available experimental and computational uncertainty-afflicted information (including discretization-modeling errors) for obtaining best-estimate calibrated model parameters and responses, together with correspondingly reduced uncertainties. This new methodology also provides quantitative indicators for assessing the consistency among parameters and responses, for consequent acceptance or rejection of information within the overall assimilation procedure. To facilitate the presentation of the fundamental concepts underlying this new methodology, its time-independent formalism is presented first, in Section 1.1 relegating the presentation of the full time-dependent formalism to Section 1.2.

1.1 Time-Independent Data Assimilation and Model Calibration

Mathematical models of physical processes comprise independent variables (e.g., time, space, energy, etc.), dependent variables (e.g., temperatures, pressures, velocities, fluxes, etc.), and model parameters (boundary and initial conditions, correlations, etc.). Specifically, consider that the mathematical model comprises N parameters (e.g., material properties, correlations, etc.), denoted by the components α_n of a vector $\boldsymbol{\alpha} = \left(\alpha_1,\ldots,\alpha_N\right)$. As a matter of convention, all vectors considered in this work are *column vectors*, unless specified otherwise. In practice, the parameters are experimentally determined quantities, so their exact values are unknown; usually, only their mean (or nominal) values, $\alpha_n^0 \equiv \left\langle \alpha_n \right\rangle$, and their covariances (uncertainties) are known. These covariances are usually represented in the form of a positive definite matrix called the *covariance matrix*, $\boldsymbol{C}_\alpha$, which is defined as

$$\boldsymbol{C}_\alpha \triangleq \left\langle \delta\boldsymbol{\alpha}\delta\boldsymbol{\alpha}^\dagger \right\rangle \triangleq \left\langle \left(\boldsymbol{\alpha}-\boldsymbol{\alpha}^0\right)\left(\boldsymbol{\alpha}-\boldsymbol{\alpha}^0\right)^\dagger \right\rangle, \tag{1.01}$$

where the components of the N-dimensional vector $\delta\boldsymbol{\alpha}$ are of the form $\delta\alpha_n \equiv \alpha_n - \alpha_n^0$, and where the dagger *(†)* signifies transposition. Note that "transposition" will be indicated only when necessary to avoid misinterpretation. The diagonal elements of $\boldsymbol{C}_\alpha$ are the variances, $\left(\boldsymbol{C}_\alpha\right)_{nn} = var\left(\alpha_n\right) = \left\langle \left(\delta\alpha_n\right)^2 \right\rangle$, of the N parameters, while the off-diagonal components are the covariances, $\left(\boldsymbol{C}_\alpha\right)_{mn} = cov\left(\alpha_m, \alpha_n\right) = \left\langle \delta\alpha_m \delta\alpha_n \right\rangle$, of the corresponding pairs of parameters.

The results computed using the mathematical model are customarily called *responses*, and will henceforth be denoted by the I-dimensional column vector $\boldsymbol{r} = \left(r_1, \ldots, r_I\right)$. Note that the actual values of these responses are also not known exactly, since $\boldsymbol{r}$ depends on the uncertain model parameters random quantities $\boldsymbol{\alpha} = \left(\alpha_1, \ldots, \alpha_N\right)$; hence, $\boldsymbol{r}$ is also considered to be a random quantity.

Consider, furthermore, that experimental measurements corresponding to the computed responses are also available. The nominal values for the *experimentally measured responses* will be denoted in the sequel by the components of an I-dimensional vector, $\boldsymbol{r}_m$ (the subscript "m" is used in this subsection to denote "experimentally measured" quantities). The associated uncertainty matrix for the experimentally measured responses will be denoted by $\boldsymbol{C}_m$, and is defined as

$$\boldsymbol{C}_m \triangleq \left\langle \delta\boldsymbol{r}_m \delta\boldsymbol{r}_m^\dagger \right\rangle \triangleq \left\langle \left(\boldsymbol{r} - \boldsymbol{r}_m\right)\left(\boldsymbol{r} - \boldsymbol{r}_m\right)^\dagger \right\rangle, \qquad \delta\boldsymbol{r}_m \equiv \boldsymbol{r} - \boldsymbol{r}_m. \tag{1.02}$$

In the most general case, the measured responses may be correlated to the parameters $\boldsymbol{\alpha} = \left(\alpha_1, \ldots, \alpha_N\right)$ through a response-parameter uncertainty (covariance) matrix of order $I \times N$, of the form

$$\boldsymbol{C}_{r\alpha} \equiv \left\langle \delta\boldsymbol{r} \delta\boldsymbol{\alpha}^\dagger \right\rangle = \left\langle \left(\boldsymbol{r} - \boldsymbol{r}_m\right)\left(\boldsymbol{\alpha} - \boldsymbol{\alpha}^0\right)^\dagger \right\rangle, \;\; \boldsymbol{C}_{\alpha r} = \left\langle \left(\boldsymbol{\alpha} - \boldsymbol{\alpha}^0\right)\left(\boldsymbol{r} - \boldsymbol{r}_m\right)^\dagger \right\rangle \tag{1.03}$$

By using the maximum entropy principle, Cacuci and Ionescu-Bujor (2010) have shown that the most objective prior probability distribution corresponding to the computational and experimental information described above is a multivariate Gaussian of the form:

$$p\left(z\,|\,\boldsymbol{C}\right)d\left(z\right)=\frac{exp\left[-\frac{1}{2}Q\left(z\right)\right]}{det\left(2\pi\boldsymbol{C}\right)^{1/2}}\,d\left(z\right),\quad Q\left(z\right)\equiv z^{\dagger}\boldsymbol{C}^{-1}z\,,-\infty<z_j<\infty, \qquad (1.04)$$

where the $\left(N+I\right)\times\left(N+I\right)$ partitioned matrix $\boldsymbol{C}$ represents the joint uncertainty matrix of the parameters and responses:

$$\boldsymbol{C}\equiv\begin{pmatrix}\boldsymbol{C}_{\alpha} & \boldsymbol{C}_{\alpha r}\\ \boldsymbol{C}_{r\alpha} & \boldsymbol{C}_{m}\end{pmatrix}, \qquad (1.05)$$

while z denotes the $\left(I+N\right)$-dimensional partitioned vector

$$z\equiv\begin{pmatrix}\boldsymbol{\alpha}-\boldsymbol{\alpha}^{0}\\ \boldsymbol{r}-\boldsymbol{r}_{m}\end{pmatrix} \qquad (1.06)$$

In general, the responses $\boldsymbol{r}=\left(r_1,\ldots,r_I\right)$ depend nonlinearly and implicitly (in an analytically intractable form) on the model parameters $\boldsymbol{\alpha}=\left(\alpha_1,\ldots,\alpha_N\right)$. Such a dependence can be generally represented in the vector-form $\boldsymbol{r}=\boldsymbol{R}\left(\boldsymbol{\alpha}\right)$. Furthermore, the uncertainties in parameters and modeling induce uncertainties in the computed responses, and can be computed either by means of statistical methods (for relatively simple models with few parameters) or deterministically, by using the propagation of moments (errors) method [see Cacuci, 2003]. In this method, the computed response is linearized via a functional Taylor-series expansion around the nominal values, $\boldsymbol{\alpha}^0$, of the parameters $\boldsymbol{\alpha}$, as follows:

$$\boldsymbol{r}=\boldsymbol{R}\left(\boldsymbol{\alpha}^{0}+\delta\boldsymbol{\alpha}\right)=\boldsymbol{R}\left(\boldsymbol{\alpha}^{0}\right)+\boldsymbol{S}\left(\boldsymbol{\alpha}^{0}\right)\left(\boldsymbol{\alpha}-\boldsymbol{\alpha}^{0}\right)+higher\ order\ terms\,, \qquad (1.07)$$

where $\boldsymbol{R}\left(\boldsymbol{\alpha}^{0}\right)$ denotes the computed response at the nominal parameter values $\boldsymbol{\alpha}^0$, while $\boldsymbol{S}\left(\boldsymbol{\alpha}^{0}\right)$ represents the $\left(N+I\right)$-dimensional matrix containing the *local sensitivites* (i.e., the first-order partial derivatives) of the computed responses with respect to the parameters, namely:

$$\boldsymbol{S}(\boldsymbol{\alpha}) \triangleq \begin{pmatrix} s_{11} & \cdots & s_{1N} \\ \vdots & \ddots & \vdots \\ s_{I1} & \cdots & s_{IN} \end{pmatrix} \triangleq \begin{pmatrix} \dfrac{\partial R_1(\boldsymbol{\alpha})}{\partial \alpha_1} & \cdots & \dfrac{\partial R_1(\boldsymbol{\alpha})}{\partial \alpha_N} \\ \vdots & \ddots & \vdots \\ \dfrac{\partial R_I(\boldsymbol{\alpha})}{\partial \alpha_1} & \cdots & \dfrac{\partial R_I(\boldsymbol{\alpha})}{\partial \alpha_N} \end{pmatrix} \tag{1.08}$$

Local sensitivities can be computed exactly only by using deterministic methods that involve some form of differentiation of the system under investigation. As first shown by [Cacuci,1981a and 1981b], the most general and comprehensive way of defining local sensitivities for operators (in the sense of nonlinear functional analysis) is in terms of the (first) Gâteaux-differential of the system's response, at the nominal value of the system's dependent variables and parameters. There are two general procedures for calculating exactly and efficiently the local sensitivities for any type of large-scale nonlinear systems (including feedback), namely the Forward Sensitivity Analysis Procedure (FSAP) and the Adjoint Sensitivity Analysis Procedure (ASAP). The FSAP is advantageous to employ only if the number of different responses of interest for the problem under consideration exceeds the number of system parameters and/or parameter variations. For large-scale systems, in which the number of system parameters and/or parameter variations to be considered exceeds the number of responses of interest, the ASAP is, by far, the most advantageous method to employ, even though its implementation requires an appropriately constructed adjoint sensitivity system. The remarkable efficiency of the ASAP stems from the fact that the adjoint sensitivity system is linear in the adjoint function, is independent of any parameter variations, and needs to be solved only once per response. In particular, if the original model is linear in the state (i.e., dependent) variables, then the adjoint sensitivity equation can be solved independently of the original model. In turn, once the adjoint function has been calculated, it is used to obtain the sensitivities to all system parameters by simple quadratures, without needing to solve repeatedly differential and/or integral equations.

In Eq. (1.07), the notation $\boldsymbol{S}\left(\boldsymbol{\alpha}^0\right)$ indicates that the sensitivity matrix is evaluated at the nominal parameter values $\boldsymbol{\alpha}^0$. It follows from Eq. (1.07) that the expectation value, $\langle \boldsymbol{r} \rangle$, of the response $\boldsymbol{r}$, and the corresponding covariance matrix, $\boldsymbol{C}_{rc}\left(\boldsymbol{\alpha}^0\right)$, are of the form

$$\langle \boldsymbol{r} \rangle = \boldsymbol{R}\left(\boldsymbol{\alpha}^0\right), \tag{1.09}$$

and

$$\begin{aligned} \boldsymbol{C}_{rc}\left(\boldsymbol{\alpha}^0\right) &\triangleq \left\langle \delta \boldsymbol{r} \delta \boldsymbol{r}^\dagger \right\rangle = \left[\boldsymbol{S}\left(\boldsymbol{\alpha}^0\right)\right] \left\langle \delta \boldsymbol{\alpha} \delta \boldsymbol{\alpha}^\dagger \right\rangle \left[\boldsymbol{S}\left(\boldsymbol{\alpha}^0\right)\right]^\dagger \\ &= \left[\boldsymbol{S}\left(\boldsymbol{\alpha}^0\right)\right] \boldsymbol{C}_\alpha \left[\boldsymbol{S}\left(\boldsymbol{\alpha}^0\right)\right]^\dagger . \end{aligned} \tag{1.10}$$

The next task is to condense the posterior information contained in Eqs. (1.04) and (1.07) into a recommended best-estimate value $\boldsymbol{z}^{be}$ for the parameters $\boldsymbol{\alpha} = \left(\alpha_1, \ldots, \alpha_N\right)$ and responses $\boldsymbol{r} = \left(r_1, \ldots, r_I\right)$, together with corresponding best-estimate recommended uncertainties for these quantities. If a loss function is given, decision theory indicates how these best-estimate quantities are to be computed. If no specific loss function is provided, the recommended best-estimate updated posterior mean vector $\boldsymbol{z}^{be}$ and its respective best-estimate posterior covariance matrix are usually evaluated by assuming "quadratic loss." In such a case, the bulk of the contribution to the distribution $p\left(\boldsymbol{z} \,|\, \boldsymbol{C}\right)$ in Eq. (1.04) is extracted by considering the point in phase space where the respective exponent attains its minimum, subject to the relation provided by Eq. (1.07). This constrained minimization problem is solved by introducing an I-dimensional vector of Lagrange multipliers, $\boldsymbol{\lambda}$, to obtain the following unconstrained minimization problem

$$\begin{aligned} & P\left(\boldsymbol{z}, \boldsymbol{\lambda}\right) \triangleq Q(\boldsymbol{z}) + 2\boldsymbol{\lambda}^\dagger \left[-\boldsymbol{r} + \boldsymbol{R}\left(\boldsymbol{\alpha}^0\right) + \boldsymbol{S}\left(\boldsymbol{\alpha}^0\right)\left(\boldsymbol{\alpha} - \boldsymbol{\alpha}^0\right)\right] = min, \\ & at\ \boldsymbol{z} = \boldsymbol{z}^{be} \equiv \begin{pmatrix} \boldsymbol{\alpha}^{be} - \boldsymbol{\alpha}^0 \\ \boldsymbol{r}^{be} - \boldsymbol{r}_m \end{pmatrix}. \end{aligned} \tag{1.11}$$

In the above expression, the superscript "*be*" denotes "*best estimated values*," and the factor "2" was introduced for convenience in front of $\boldsymbol{\lambda}$ in order to simplify the subsequent algebraic derivations. The point $\boldsymbol{z}^{be}$ where the functional $P\left(\boldsymbol{z}, \boldsymbol{\lambda}\right)$ attains its extremum (minimum) is defined as the point where its derivative with respect to $\boldsymbol{z}$ vanishes. This point can be conveniently determined by rewriting $P\left(\boldsymbol{z}, \boldsymbol{\lambda}\right)$ in the form

$$P\left(\boldsymbol{z},\boldsymbol{\lambda}\right) \equiv Q(\boldsymbol{z}) + 2\boldsymbol{\lambda}^{\dagger}\left\{\left[\boldsymbol{S}\left(\boldsymbol{\alpha}\right),-\boldsymbol{I}_{I}\right]\boldsymbol{z}+\boldsymbol{d}\right\} = min,\ \ at\ \boldsymbol{z}=\boldsymbol{z}^{be}, \tag{1.12}$$

where

$$\boldsymbol{d} \triangleq \boldsymbol{R}\left(\boldsymbol{\alpha}^{0}\right) - \boldsymbol{r}_{m} \tag{1.13}$$

is an I -dimensional vector of "deviations" reflecting the discrepancies between the nominal computations and the nominally measured responses.

Thus, $P(\boldsymbol{z})$ becomes stationary at the point $\boldsymbol{z}=\boldsymbol{z}^{be}$, which is defined implicitly through the conditions

$$\nabla_{z}P\left(\boldsymbol{z},\boldsymbol{\lambda}\right)=\boldsymbol{0},\ \ \nabla_{\lambda}P\left(\boldsymbol{z},\boldsymbol{\lambda}\right)=\boldsymbol{0},\ \ \ at\ \boldsymbol{z}=\boldsymbol{z}^{be}. \tag{1.14}$$

The condition $\nabla_{\lambda}P\left(\boldsymbol{z},\boldsymbol{\lambda}\right)=\boldsymbol{0}$ ensures that the constraint represented by Eq. (1.07) is fulfilled at $\boldsymbol{z}=\boldsymbol{z}^{be}$, while the condition $\nabla_{z}P\left(\boldsymbol{z},\boldsymbol{\lambda}\right)=\boldsymbol{0}$ yields

$$\begin{aligned}\nabla_{z}P\left(\boldsymbol{z},\boldsymbol{\lambda}\right) &= \nabla_{z}\left\{\boldsymbol{z}^{\dagger}\boldsymbol{C}^{-1}\boldsymbol{z}+2\left[\boldsymbol{\lambda}^{\dagger}\boldsymbol{S}\left(\boldsymbol{\alpha}\right),-\boldsymbol{\lambda}^{\dagger}\right]\boldsymbol{z}+2\boldsymbol{\lambda}^{\dagger}\boldsymbol{d}\right\}\\ &= 2\boldsymbol{C}^{-1}\boldsymbol{z}+2\begin{pmatrix}\boldsymbol{S}^{\dagger}\left(\boldsymbol{\alpha}\right)\boldsymbol{\lambda}\\ -\boldsymbol{\lambda}\end{pmatrix}=\boldsymbol{0},\ \ \ at\ \boldsymbol{z}=\boldsymbol{z}^{be}.\end{aligned} \tag{1.15}$$

Multiplying the last line of the above equation on the left by $\boldsymbol{C}$ and solving it for $\boldsymbol{z}^{be}$ gives:

$$\boldsymbol{z}^{be}=\boldsymbol{C}\begin{pmatrix}\boldsymbol{S}^{\dagger}\left(\boldsymbol{\alpha}\right)\boldsymbol{\lambda}\\ -\boldsymbol{\lambda}\end{pmatrix}=\begin{pmatrix}\boldsymbol{C}_{\alpha} & \boldsymbol{C}_{\alpha r}\\ \boldsymbol{C}_{r\alpha} & \boldsymbol{C}_{m}\end{pmatrix}\begin{pmatrix}\boldsymbol{S}^{\dagger}\left(\boldsymbol{\alpha}\right)\boldsymbol{\lambda}\\ -\boldsymbol{\lambda}\end{pmatrix}. \tag{1.16}$$

Writing the above expression in component form gives the following results for the calibrated best-estimate parameters and responses, respectively:

$$\boldsymbol{\alpha}^{be} = \boldsymbol{\alpha}^0 + \left(\boldsymbol{C}_{\alpha r} - \boldsymbol{C}_{\alpha} \left[\boldsymbol{S}\left(\boldsymbol{\alpha}^0\right) \right]^{\dagger} \right) \boldsymbol{\lambda}, \tag{1.17}$$

$$\boldsymbol{r}_c\left(\boldsymbol{\alpha}^{be}\right) = \boldsymbol{r}_m + \left(\boldsymbol{C}_m - \boldsymbol{C}_{r\alpha} \left[\boldsymbol{S}\left(\boldsymbol{\alpha}^0\right) \right]^{\dagger} \right) \boldsymbol{\lambda}. \tag{1.18}$$

Evaluating Eq. (1.07) at $\boldsymbol{z}^{be}$ while using Eqs. (1.17) and (1.18) yields the following important expression for the Lagrange multiplier $\boldsymbol{\lambda}$:

$$\boldsymbol{d} \equiv \boldsymbol{R}\left(\boldsymbol{\alpha}^0\right) - \boldsymbol{r}_m = \left[\boldsymbol{C}_{rc}\left(\boldsymbol{\alpha}^0\right) - \boldsymbol{C}_{r\alpha} \left[\boldsymbol{S}\left(\boldsymbol{\alpha}^0\right) \right]^{\dagger} - \left[\boldsymbol{S}\left(\boldsymbol{\alpha}^0\right) \right] \boldsymbol{C}_{\alpha r} + \boldsymbol{C}_m \right] \boldsymbol{\lambda}. \tag{1.19}$$

In Eq. (1.19), the matrix-valued expression that multiplies $\boldsymbol{\lambda}$ is actually the covariance-matrix, $\boldsymbol{C}_d\left(\boldsymbol{\alpha}^0\right)$, of the vector of response-deviations, $\boldsymbol{d}$, as shown below:

$$\begin{aligned} \boldsymbol{C}_d\left(\boldsymbol{\alpha}^0\right) &\triangleq \left\langle \boldsymbol{d}\boldsymbol{d}^{\dagger} \right\rangle = \left\langle \left(\delta\boldsymbol{r} - \boldsymbol{S}\left(\boldsymbol{\alpha}^0\right)\delta\boldsymbol{\alpha} \right) \left(\delta\boldsymbol{r}^{\dagger} - \delta\boldsymbol{\alpha}^{\dagger} \left[\boldsymbol{S}\left(\boldsymbol{\alpha}^0\right) \right]^{\dagger} \right) \right\rangle \\ &= \boldsymbol{C}_{rc}\left(\boldsymbol{\alpha}^0\right) - \boldsymbol{C}_{r\alpha} \left[\boldsymbol{S}\left(\boldsymbol{\alpha}^0\right) \right]^{\dagger} - \left[\boldsymbol{S}\left(\boldsymbol{\alpha}^0\right) \right] \boldsymbol{C}_{\alpha r} + \boldsymbol{C}_m . \end{aligned} \tag{1.20}$$

Hence, the expression of the Lagrange multiplier $\boldsymbol{\lambda}$ at $\boldsymbol{z}^{be}$ becomes

$$\boldsymbol{\lambda} = \left[\boldsymbol{C}_d\left(\boldsymbol{\alpha}^0\right) \right]^{-1} \boldsymbol{d}. \tag{1.21}$$

Note that the second and third terms in Eq. (1.20), which are transposes of each other, are square matrices of order I resulting from the multiplication of two rectangular matrices. Consequently, the matrix $\boldsymbol{C}_d\left(\boldsymbol{\alpha}^0\right)$ is a symmetric matrix of order I, which is important when computing its inverse since, in practical problems, the number of computed or measured responses is typically much less than the number N of model parameters.

Replacing now Eq. (1.21) in Eqs. (1.17) and (1.18), respectively, yields the following expressions for the nominal values of the calibrated (adjusted) best-estimate responses and parameters:

$$\boldsymbol{\alpha}^{be} = \boldsymbol{\alpha}^{0} + \left(\boldsymbol{C}_{\alpha r} - \boldsymbol{C}_{\alpha}\left[\boldsymbol{S}\left(\boldsymbol{\alpha}^{0}\right)\right]^{\dagger}\right)\left[\boldsymbol{C}_{d}\left(\boldsymbol{\alpha}^{0}\right)\right]^{-1}\boldsymbol{d}, \tag{1.22}$$

$$\boldsymbol{r}^{be} \triangleq \boldsymbol{r}\left(\boldsymbol{\alpha}^{be}\right) = \boldsymbol{r}_{m} + \left(\boldsymbol{C}_{m} - \boldsymbol{C}_{r\alpha}\left[\boldsymbol{S}\left(\boldsymbol{\alpha}^{0}\right)\right]^{\dagger}\right)\left[\boldsymbol{C}_{d}\left(\boldsymbol{\alpha}^{0}\right)\right]^{-1}\boldsymbol{d}. \tag{1.23}$$

Using Eqs. (1.21), (1.16) and (1.7) in Eq. (1.11) yields the following expression for the minimum of $Q\left(\boldsymbol{z}\right)$:

$$\begin{aligned} Q_{min} &\equiv Q\left(\boldsymbol{z}^{be}\right) = \left[-\boldsymbol{\lambda}^{\dagger}\boldsymbol{Z}\left(\boldsymbol{\alpha}^{0}\right)\boldsymbol{C}\right]\boldsymbol{C}^{-1}\boldsymbol{z}^{be} \\ &= -\boldsymbol{\lambda}^{\dagger}\boldsymbol{Z}\left(\boldsymbol{\alpha}^{0}\right)\boldsymbol{z}^{be} = \boldsymbol{\lambda}^{\dagger}\boldsymbol{d} = \boldsymbol{d}^{\dagger}\left[\boldsymbol{C}_{d}\left(\boldsymbol{\alpha}^{0}\right)\right]^{-1}\boldsymbol{d}. \end{aligned} \tag{1.24}$$

The new, best-estimate covariances, $\boldsymbol{C}_{\alpha}^{be}$ and $\boldsymbol{C}_{r}^{be}$, corresponding to the best-estimate parameters $\boldsymbol{\alpha}^{be}$ and responses $\boldsymbol{r}\left(\boldsymbol{\alpha}^{be}\right)$, together with the new best-estimate parameter-response covariance matrix $\boldsymbol{C}_{\alpha r}^{be}$ are defined as follows:

$$\boldsymbol{C}_{\alpha}^{be} \triangleq \left\langle\left(\boldsymbol{\alpha} - \boldsymbol{\alpha}^{be}\right)\left(\boldsymbol{\alpha} - \boldsymbol{\alpha}^{be}\right)^{\dagger}\right\rangle, \tag{1.25}$$

$$\boldsymbol{C}_{r}^{be} \triangleq \left\langle\left(\boldsymbol{r} - \boldsymbol{r}\left(\boldsymbol{\alpha}^{be}\right)\right)\left(\boldsymbol{r} - \boldsymbol{r}\left(\boldsymbol{\alpha}^{be}\right)\right)^{\dagger}\right\rangle, \tag{1.26}$$

$$\boldsymbol{C}_{\alpha r}^{be} \triangleq \left\langle\left(\boldsymbol{\alpha} - \boldsymbol{\alpha}^{be}\right)\left(\boldsymbol{r} - \boldsymbol{r}\left(\boldsymbol{\alpha}^{be}\right)\right)^{\dagger}\right\rangle. \tag{1.27}$$

The explicit expression of $\boldsymbol{C}_{\alpha}^{be}$ is obtained by replacing Eq. (1.22) in Eq. (1.25), carrying out the respective averaging procedure, and recalling from Eqs. (1.07) and (1.12) that

$$\boldsymbol{d} \triangleq \boldsymbol{R}\left(\boldsymbol{\alpha}^{0}\right) - \boldsymbol{r}_{m} = \boldsymbol{r} - \boldsymbol{r}_{m} - \boldsymbol{S}\left(\boldsymbol{\alpha}^{0}\right)\left(\boldsymbol{\alpha} - \boldsymbol{\alpha}^{0}\right). \tag{1.28}$$

Thus, replacing Eq. (1.22) in Eq. (1.25) gives

$$\begin{aligned}\boldsymbol{C}_{\alpha}^{be} \triangleq & \left\langle \left(\boldsymbol{\alpha}-\boldsymbol{\alpha}^{0}\right)\left(\boldsymbol{\alpha}-\boldsymbol{\alpha}^{0}\right)^{\dagger} \right\rangle - \left\langle \left(\boldsymbol{\alpha}-\boldsymbol{\alpha}^{0}\right)\boldsymbol{d}^{\dagger} \right\rangle \left[\boldsymbol{C}_{d}\left(\boldsymbol{\alpha}^{0}\right)\right]^{-1}\left(\boldsymbol{C}_{\alpha r}-\left[\boldsymbol{S}\left(\boldsymbol{\alpha}^{0}\right)\right]\boldsymbol{C}_{\alpha}\right) \\ & -\left(\boldsymbol{C}_{\alpha r}-\boldsymbol{C}_{\alpha}\left[\boldsymbol{S}\left(\boldsymbol{\alpha}^{0}\right)\right]^{\dagger}\right)\left[\boldsymbol{C}_{d}\left(\boldsymbol{\alpha}^{0}\right)\right]^{-1}\left\langle \boldsymbol{d}\left(\boldsymbol{\alpha}-\boldsymbol{\alpha}^{0}\right)^{\dagger} \right\rangle \\ & +\left(\boldsymbol{C}_{\alpha r}-\boldsymbol{C}_{\alpha}\left[\boldsymbol{S}\left(\boldsymbol{\alpha}^{0}\right)\right]^{\dagger}\right)\left[\boldsymbol{C}_{d}\left(\boldsymbol{\alpha}^{0}\right)\right]^{-1}\left\langle \boldsymbol{d}\boldsymbol{d}^{\dagger} \right\rangle \left[\boldsymbol{C}_{d}\left(\boldsymbol{\alpha}^{0}\right)\right]^{-1}\left(\boldsymbol{C}_{\alpha r}-\left[\boldsymbol{S}\left(\boldsymbol{\alpha}^{0}\right)\right]\boldsymbol{C}_{\alpha}\right).\end{aligned} \tag{1.29}$$

The above expression can be simplified by recalling Eq. (1.20), and by noting that

$$\boldsymbol{C}_{\alpha d}\left(\boldsymbol{\alpha}^{0}\right) \triangleq \left\langle \left(\boldsymbol{\alpha}-\boldsymbol{\alpha}^{0}\right)\boldsymbol{d}^{\dagger} \right\rangle = \left(\boldsymbol{C}_{\alpha r}-\boldsymbol{C}_{\alpha}\left[\boldsymbol{S}\left(\boldsymbol{\alpha}^{0}\right)\right]^{\dagger}\right), \tag{1.30}$$

$$\boldsymbol{C}_{d\alpha}\left(\boldsymbol{\alpha}^{0}\right) \triangleq \left\langle \boldsymbol{d}\left(\boldsymbol{\alpha}-\boldsymbol{\alpha}^{0}\right)^{\dagger} \right\rangle = \left(\boldsymbol{C}_{\alpha r}-\left[\boldsymbol{S}\left(\boldsymbol{\alpha}^{0}\right)\right]\boldsymbol{C}_{\alpha}\right) = \left[\boldsymbol{C}_{\alpha d}\left(\boldsymbol{\alpha}^{0}\right)\right]^{\dagger} \tag{1.31}$$

Replacing Eqs. (1.29) through (1.31) in the expression of $\boldsymbol{C}_{\alpha}^{be}$ leads to

$$\begin{aligned}\boldsymbol{C}_{\alpha}^{be} &= \boldsymbol{C}_{\alpha}-\left(\boldsymbol{C}_{\alpha r}-\boldsymbol{C}_{\alpha}\left[\boldsymbol{S}\left(\boldsymbol{\alpha}^{0}\right)\right]^{\dagger}\right)\left[\boldsymbol{C}_{d}\left(\boldsymbol{\alpha}^{0}\right)\right]^{-1}\left(\boldsymbol{C}_{\alpha r}-\left[\boldsymbol{S}\left(\boldsymbol{\alpha}^{0}\right)\right]\boldsymbol{C}_{\alpha}\right) \\ &= \boldsymbol{C}_{\alpha}-\left[\boldsymbol{C}_{\alpha d}\left(\boldsymbol{\alpha}^{0}\right)\right]\left[\boldsymbol{C}_{d}\left(\boldsymbol{\alpha}^{0}\right)\right]^{-1}\left[\boldsymbol{C}_{\alpha d}\left(\boldsymbol{\alpha}^{0}\right)\right]^{\dagger}.\end{aligned} \tag{1.32}$$

Furthermore, noting that

$$\boldsymbol{C}_{rd}\left(\boldsymbol{\alpha}^{0}\right) \triangleq \left\langle \left(\boldsymbol{r}-\boldsymbol{r}_{m}\right)\boldsymbol{d}^{\dagger} \right\rangle = \left(\boldsymbol{C}_{m}-\boldsymbol{C}_{r\alpha}\left[\boldsymbol{S}\left(\boldsymbol{\alpha}^{0}\right)\right]^{\dagger}\right),\; \boldsymbol{C}_{dr}\left(\boldsymbol{\alpha}^{0}\right) \triangleq \left\langle \boldsymbol{d}\left(\boldsymbol{r}-\boldsymbol{r}_{m}\right)^{\dagger} \right\rangle = \left(\boldsymbol{C}_{m}-\left[\boldsymbol{S}\left(\boldsymbol{\alpha}^{0}\right)\right]\boldsymbol{C}_{r\alpha}\right) \tag{1.33}$$

and replacing the above expressions in Eq. (1.26) gives the following expression for the best-estimate parameter covariance matrix:

$$\begin{aligned}\boldsymbol{C}_{r}^{be} &= \boldsymbol{C}_{m}-\left(\boldsymbol{C}_{m}-\boldsymbol{C}_{r\alpha}\left[\boldsymbol{S}\left(\boldsymbol{\alpha}^{0}\right)\right]^{\dagger}\right)\left[\boldsymbol{C}_{d}\left(\boldsymbol{\alpha}^{0}\right)\right]^{-1}\left(\boldsymbol{C}_{m}-\left[\boldsymbol{S}\left(\boldsymbol{\alpha}^{0}\right)\right]\boldsymbol{C}_{\alpha r}\right) \\ &= \boldsymbol{C}_{m}-\left[\boldsymbol{C}_{rd}\left(\boldsymbol{\alpha}^{0}\right)\right]\left[\boldsymbol{C}_{d}\left(\boldsymbol{\alpha}^{0}\right)\right]^{-1}\left[\boldsymbol{C}_{rd}\left(\boldsymbol{\alpha}^{0}\right)\right]^{\dagger}.\end{aligned} \tag{1.34}$$

A similar sequence of computations leads to the following expression for the best-estimate response-parameter covariance matrix:

$$\begin{aligned} \boldsymbol{C}_{r\alpha}^{be} &= \boldsymbol{C}_{\alpha r}^{be} \\ &= \boldsymbol{C}_{r\alpha} - \left(\boldsymbol{C}_{m} - \boldsymbol{C}_{r\alpha}\left[\boldsymbol{S}\left(\boldsymbol{\alpha}^{0}\right)\right]^{\dagger}\right)\left[\boldsymbol{C}_{d}\left(\boldsymbol{\alpha}^{0}\right)\right]^{-1}\left(\boldsymbol{C}_{\alpha r} - \left[\boldsymbol{S}\left(\boldsymbol{\alpha}^{0}\right)\right]\boldsymbol{C}_{\alpha}\right) \\ &= \boldsymbol{C}_{r\alpha} - \left[\boldsymbol{C}_{rd}\left(\boldsymbol{\alpha}^{0}\right)\right]\left[\boldsymbol{C}_{d}\left(\boldsymbol{\alpha}^{0}\right)\right]^{-1}\left[\boldsymbol{C}_{\alpha d}\left(\boldsymbol{\alpha}^{0}\right)\right]^{\dagger}. \end{aligned} \tag{1.35}$$

Note in Eq. (1.32) that a symmetric positive matrix is subtracted from the initial parameter covariance matrix $\boldsymbol{C}_{\alpha}$. In this sense, therefore, the best-estimate parameter uncertainty matrix $\boldsymbol{C}_{\alpha}^{be}$ has been reduced by the calibration (adjustment) procedure, which has introduced new information from experiments. Similarly, in Eq. (1.34), a symmetric positive matrix is subtracted from the initial covariance matrix $\boldsymbol{C}_{m}$ of the experimentally measured responses. Hence, the best-estimate response covariance matrix $\boldsymbol{C}_{r}^{be}$ has also been improved (reduced) through the addition of new experimental information. Furthermore, Eq. (1.35) indicates that the calibration (adjustment) procedure will introduce correlations between the calibrated (adjusted) parameters and responses even if the parameters and response were initially uncorrelated, since $\boldsymbol{C}_{r\alpha}^{be} \neq 0$ even if $\boldsymbol{C}_{r\alpha} = 0$, i.e.,

$$\boldsymbol{C}_{r\alpha}^{be} = \boldsymbol{C}_{m}\left[\boldsymbol{C}_{rc}\left(\boldsymbol{\alpha}^{0}\right) + \boldsymbol{C}_{m}\right]^{-1}\left[\boldsymbol{S}\left(\boldsymbol{\alpha}^{0}\right)\right]\boldsymbol{C}_{\alpha}\text{, when } \boldsymbol{C}_{r\alpha} = 0\,. \tag{1.36}$$

As the above expression indicates, the adjustment (calibration) modifies the correlations among the parameters through couplings introduced by the sensitivities of the participating responses; these sensitivities relate the initial parameter-covariances and experimental-response covariances. Furthermore, the incorporation of additional (experimental) information in the adjustment (calibration) process reduces the variances of the adjusted parameters and responses while also modifying their correlations.

Note that Eq. (1.34) expresses the best-estimate response covariance matrix $\boldsymbol{C}_r^{be}$ in terms of the initial covariance matrix $\boldsymbol{C}_m$ of the experimental-responses. Alternatively, it is of interest to derive the expression of the computed best-estimate response covariance matrix, $\boldsymbol{C}_{rc}^{be}$, by using the propagation of moments (errors) method directly on the calibrated model, in which the nominal parameter values $\boldsymbol{\alpha}^0$ are replaced by their "best estimated" values $\boldsymbol{\alpha}^{be}$. Here, the subscript "rc" attached to $\boldsymbol{C}_{rc}^{be}$ refers to "computed response", to emphasize that $\boldsymbol{C}_{rc}^{be}$ is to be computed by using the propagation of errors on the calibrated model, and thus distinguish it from the covariance $\boldsymbol{C}_r^{be}$ (which results directly from the calibration/adjustment process applied to the nominal model). In order to compute $\boldsymbol{C}_{rc}^{be}$ using the propagation of moments method, the model is linearized around $\boldsymbol{\alpha}^{be}$ (instead of $\boldsymbol{\alpha}^0$), i.e.

$$\boldsymbol{r} = \boldsymbol{R}\left(\boldsymbol{\alpha}^{be}\right) + \boldsymbol{S}\left(\boldsymbol{\alpha}^{be}\right)\left(\boldsymbol{\alpha} - \boldsymbol{\alpha}^{be}\right) + \textit{higher order terms}\,. \tag{1.37}$$

It follows from Eqs. (1.37) that

$$\begin{aligned}
\boldsymbol{C}_{rc}^{be} &= \left\langle \left(\boldsymbol{r} - \boldsymbol{R}\left(\boldsymbol{\alpha}^{be}\right)\right)\left(\boldsymbol{r} - \boldsymbol{R}\left(\boldsymbol{\alpha}^{be}\right)\right)^{\dagger} \right\rangle \\
&= \left[\boldsymbol{S}\left(\boldsymbol{\alpha}^{be}\right)\right]\left\langle \left(\boldsymbol{\alpha} - \boldsymbol{\alpha}^{be}\right)\left(\boldsymbol{\alpha} - \boldsymbol{\alpha}^{be}\right)^{\dagger} \right\rangle \left[\boldsymbol{S}\left(\boldsymbol{\alpha}^{be}\right)\right]^{\dagger} \\
&= \left[\boldsymbol{S}\left(\boldsymbol{\alpha}^{be}\right)\right]\boldsymbol{C}_{\alpha}^{be}\left[\boldsymbol{S}\left(\boldsymbol{\alpha}^{be}\right)\right]^{\dagger} \\
&= \left[\boldsymbol{S}\left(\boldsymbol{\alpha}^{be}\right)\right]\left\{\boldsymbol{C}_{\alpha} - \left[\boldsymbol{C}_{\alpha d}\left(\boldsymbol{\alpha}^0\right)\right]\left[\boldsymbol{C}_d\left(\boldsymbol{\alpha}^0\right)\right]^{-1}\left[\boldsymbol{C}_{\alpha d}\left(\boldsymbol{\alpha}^0\right)\right]^{\dagger}\right\}\left[\boldsymbol{S}\left(\boldsymbol{\alpha}^{be}\right)\right]^{\dagger}.
\end{aligned} \tag{1.38}$$

Comparing Eq. (1.38) to Eq. (1.34) reveals that, in general, $\boldsymbol{C}_{rc}^{be} \neq \boldsymbol{C}_r^{be}$ since $\boldsymbol{S}\left(\boldsymbol{\alpha}^{be}\right) \neq \boldsymbol{S}\left(\boldsymbol{\alpha}^0\right)$. However, when the model is exactly linear, the sensitivity matrix $\boldsymbol{S}$ is independent of the parameter values $\boldsymbol{\alpha}$, i.e.,

$$\boldsymbol{S}\left(\boldsymbol{\alpha}^{be}\right) = \boldsymbol{S}\left(\boldsymbol{\alpha}^0\right) = \boldsymbol{S}\,, \text{ for linear models.} \tag{1.39}$$

It consequently follows that

$$\begin{aligned} \boldsymbol{C}_{rc}^{be} &= \boldsymbol{S}\left[\boldsymbol{C}_{\alpha} - \left(\boldsymbol{C}_{\alpha r} - \boldsymbol{C}_{\alpha}\boldsymbol{S}^{\dagger}\right)\boldsymbol{C}_{d}^{-1}\left(\boldsymbol{C}_{\alpha r} - \boldsymbol{S}\boldsymbol{C}_{\alpha}\right)\right]\boldsymbol{S}^{\dagger} \\ &= \boldsymbol{C}_{rc} - \left(\boldsymbol{C}_{rc} - \boldsymbol{S}\boldsymbol{C}_{\alpha r}\right)\left[\boldsymbol{C}_{rc} + \boldsymbol{C}_{e} - \boldsymbol{C}_{r\alpha}\boldsymbol{S}^{\dagger} - \boldsymbol{S}\boldsymbol{C}_{\alpha r}\right]^{-1}\left(\boldsymbol{C}_{rc} - \boldsymbol{C}_{\alpha r}\boldsymbol{S}^{\dagger}\right) \\ &= \boldsymbol{C}_{r}^{be}, \quad \textbf{\textit{for linear models.}} \end{aligned} \tag{1.40}$$

The above equality can be demonstrated by using the following identity which holds for regular square matrices $\boldsymbol{A}$, $\boldsymbol{B}$ and $\boldsymbol{C}$:

$$\begin{aligned} &\boldsymbol{A} - \left(\boldsymbol{A} - \boldsymbol{C}^{\dagger}\right)\left(\boldsymbol{A} + \boldsymbol{B} - \boldsymbol{C} - \boldsymbol{C}^{\dagger}\right)^{-1}\left(\boldsymbol{A} - \boldsymbol{C}\right) \\ &= \boldsymbol{B} - \left(\boldsymbol{B} - \boldsymbol{C}\right)\left(\boldsymbol{A} + \boldsymbol{B} - \boldsymbol{C} - \boldsymbol{C}^{\dagger}\right)^{-1}\left(\boldsymbol{B} - \boldsymbol{C}^{\dagger}\right). \end{aligned} \tag{1.41}$$

and by effecting the replacements $\boldsymbol{A} \rightarrow \boldsymbol{C}_{rc}$, $\boldsymbol{B} \rightarrow \boldsymbol{C}_{e}$ $\boldsymbol{C} \rightarrow \boldsymbol{C}_{\alpha r}\boldsymbol{S}^{\dagger}$ in the above identity. For completeness, note that Eq. (1.41) can be obtained by starting from the identity

$$\boldsymbol{I} = \left(\boldsymbol{A} - \boldsymbol{C}^{\dagger}\right)\left(\boldsymbol{A} + \boldsymbol{B} - \boldsymbol{C} - \boldsymbol{C}^{\dagger}\right)^{-1} + \left(\boldsymbol{B} - \boldsymbol{C}\right)\left(\boldsymbol{A} + \boldsymbol{B} - \boldsymbol{C} - \boldsymbol{C}^{\dagger}\right)^{-1},$$

and by multiplying it on the right by $\left(\boldsymbol{A} - \boldsymbol{C}\right)$ to obtain

$$\begin{aligned} \boldsymbol{A} - \boldsymbol{C} &= \left(\boldsymbol{A} - \boldsymbol{C}^{\dagger}\right)\left(\boldsymbol{A} + \boldsymbol{B} - \boldsymbol{C} - \boldsymbol{C}^{\dagger}\right)^{-1}\left(\boldsymbol{A} - \boldsymbol{C}\right) \\ &\quad + \left(\boldsymbol{B} - \boldsymbol{C}\right)\left(\boldsymbol{A} + \boldsymbol{B} - \boldsymbol{C} - \boldsymbol{C}^{\dagger}\right)^{-1}\left(\boldsymbol{A} - \boldsymbol{C} + \boldsymbol{B} - \boldsymbol{B} + \boldsymbol{C}^{\dagger} - \boldsymbol{C}^{\dagger}\right) \\ &= \left(\boldsymbol{A} - \boldsymbol{C}^{\dagger}\right)\left(\boldsymbol{A} + \boldsymbol{B} - \boldsymbol{C} - \boldsymbol{C}^{\dagger}\right)^{-1}\left(\boldsymbol{A} - \boldsymbol{C}\right) \\ &\quad + \left(\boldsymbol{B} - \boldsymbol{C}\right)\left(\boldsymbol{A} + \boldsymbol{B} - \boldsymbol{C} - \boldsymbol{C}^{\dagger}\right)^{-1}\left(\boldsymbol{A} + \boldsymbol{B} - \boldsymbol{C} - \boldsymbol{C}^{\dagger}\right) \\ &\quad - \left(\boldsymbol{B} - \boldsymbol{C}\right)\left(\boldsymbol{A} + \boldsymbol{B} - \boldsymbol{C} - \boldsymbol{C}^{\dagger}\right)^{-1}\left(\boldsymbol{B} - \boldsymbol{C}^{\dagger}\right), \end{aligned}$$

a result which, after some minor rearrangements, reduces to Eq. (1.41).

It is important to note that the computation of the best estimate parameter and response values, together with their corresponding best-estimate uncertainties, namely Eqs. (1.23), (1.24), (1.32) requires the inversion of a single matrix, namely the matrix $\boldsymbol{C}_d\left(\boldsymbol{\alpha}^0\right)$ defined in Eq. (1.20). Note also that $\boldsymbol{C}_d\left(\boldsymbol{\alpha}^0\right)$ is matrix of order I , which is computationally advantageous to invert in practice, since the number of measured (or computed responses) is most often considerably smaller that the number of model parameters N .

On the other hand, for the relatively rarely encountered practical instances when $I \gg N$, it is also possible to derive alternative expressions for the best-estimate calibrated parameters and their corresponding best-estimate covariances, by using the linearized model, namely Eq. (1.07) to eliminate at the outset the response (variable) $\boldsymbol{r}$, and carry out the minimization procedure solely for the parameters (variable) $\boldsymbol{\alpha}$, thus performing all derivations in the N-dimensional "parameter space" rather than in the I-dimensional "response space." These derivations are quite tedious to perform, but a considerable shortcut can be achieved by rewriting the matrix $\left[\boldsymbol{C}_d\left(\boldsymbol{\alpha}^0\right)\right]^{-1}$ in an alternative way, by employing the Sherman-Morrison-Woodbury extension, namely:

$$\left(\boldsymbol{A}+\boldsymbol{C}\boldsymbol{B}\boldsymbol{D}^{\dagger}\right)^{-1} = \boldsymbol{A}^{-1} - \boldsymbol{A}^{-1}\boldsymbol{C}\left(\boldsymbol{B}^{-1} + \boldsymbol{D}^{\dagger}\boldsymbol{A}^{-1}\boldsymbol{C}\right)^{-1}\boldsymbol{D}^{\dagger}\boldsymbol{A}^{-1}, \qquad (1.42)$$

with $\boldsymbol{A}$ and $\boldsymbol{B}$ are invertible, and $\boldsymbol{D} = \boldsymbol{C}$. Thus, applying Eq. (1.42) to Eq. (1.21) leads to

$$\begin{aligned} \boldsymbol{C}_d^{-1} &\triangleq \left(\boldsymbol{C}_{rc} - \boldsymbol{C}_{r\alpha}\boldsymbol{S}^{\dagger} - \boldsymbol{S}\boldsymbol{C}_{\alpha r} + \boldsymbol{C}_m\right)^{-1} \\ &= \boldsymbol{A}^{-1} - \boldsymbol{A}^{-1}\boldsymbol{S}\left(\boldsymbol{C}_{\alpha}^{-1} + \boldsymbol{S}^{\dagger}\boldsymbol{A}^{-1}\boldsymbol{S}\right)^{-1}\boldsymbol{S}^{\dagger}\boldsymbol{A}^{-1}, \text{ with} . \\ \boldsymbol{A} &\triangleq \boldsymbol{C}_m - \boldsymbol{C}_{r\alpha}\boldsymbol{S}^{\dagger} - \boldsymbol{S}\boldsymbol{C}_{\alpha r} . \end{aligned} \qquad (1.43)$$

The above expression provides the bridge between the "response-space" and "parameter-space" formulations of the data adjustment procedure. The above expression highlights the fact that the response-space formulation requires a single inversion of an I-dimensional square symmetric matrix, while the "parameter space" formulation require the inversion of three symmetric matrices, two of which are N-dimensional and one is I-dimensional. When the parameters and responses are initially uncorrelated, i.e., if $\boldsymbol{C}_{r\alpha} = \boldsymbol{0}$, then the expressions in parameter space of the best-estimate calibrated (adjusted) quantities can be simplified somewhat by using the following special form of Eq. (1.43):

$$\boldsymbol{B}\boldsymbol{C}^{\dagger}\left(\boldsymbol{A}+\boldsymbol{C}\boldsymbol{B}\boldsymbol{C}^{\dagger}\right)^{-1}=\left(\boldsymbol{B}^{-1}+\boldsymbol{C}^{\dagger}\boldsymbol{A}^{-1}\boldsymbol{C}\right)^{-1}\boldsymbol{C}^{\dagger}\boldsymbol{A}^{-1}, \tag{1.44}$$

in which case Eq. (1.43) can be rewritten in the form

$$\boldsymbol{C}_{\alpha}\boldsymbol{S}^{\dagger}\boldsymbol{C}_{d}^{-1}=\left(\boldsymbol{C}_{\alpha}^{-1}+\boldsymbol{S}^{\dagger}\boldsymbol{C}_{m}^{-1}\boldsymbol{S}\right)^{-1}\boldsymbol{S}^{\dagger}\boldsymbol{C}_{m}^{-1}, \text{ when } \boldsymbol{C}_{r\alpha}=\boldsymbol{0}. \tag{1.45}$$

In the above case, the "parameter-space" expressions for $\boldsymbol{\alpha}^{be}$ and $\boldsymbol{C}_{\alpha}^{be}$ become

$$\boldsymbol{\alpha}^{be}=\boldsymbol{\alpha}^{0}-\left(\boldsymbol{C}_{\alpha}^{-1}+\boldsymbol{S}^{\dagger}\boldsymbol{C}_{m}^{-1}\boldsymbol{S}\right)^{-1}\boldsymbol{S}^{\dagger}\boldsymbol{C}_{m}^{-1}\boldsymbol{d}, \quad \text{when } \boldsymbol{C}_{r\alpha}=\boldsymbol{0}, \tag{1.46}$$

$$\boldsymbol{C}_{\alpha}^{be}=\left(\boldsymbol{C}_{\alpha}^{-1}+\boldsymbol{S}^{\dagger}\boldsymbol{C}_{m}^{-1}\boldsymbol{S}\right)^{-1}, \quad \text{when } \boldsymbol{C}_{r\alpha}=\boldsymbol{0}. \tag{1.47}$$

The computational evaluation of the above expressions still requires the inversion of two N-dimensional one I-dimensional symmetric matrices. From a computational standpoint, therefore, the parameter-space formulations should be avoided whenever possible, using the "response-space" formulations instead.

1.1.1 Data Consistency Indicators

The actual application of the model calibration (adjustment) algorithms, consisting of Eqs. (1.22), (1.23), (1.32), (1.34) and (1.35), to a physical system is straightforward, in principle, although it can become computationally very demanding in terms of data handling and computational speed requirements. It is also important to note that the indiscriminate incorporation of all (seemingly relevant) experimental-response data could produce a set of calibrated (adjusted) parameter values that might differ unreasonably much from the corresponding original nominal values. Worse yet, the indiscriminate use of information might even fail to improve the agreement between the calculated and measured values of some of the very responses by which the library was calibrated (adjusted).

When calibrating (adjusting) a library of model parameters, it is tacitly assumed that the given parameters are basically "correct," except that they are not sufficiently accurate for the objective at hand. The calibration procedure uses additional data (e.g., experimental responses) for improving the parameter values while reducing their uncertainties. Although such additional information induces modifications of the original parameter values, the adjusted parameters are still generally expected to remain consistent with their original nominal values, within the range of their original uncertainties. As just mentioned, however, indiscriminate calibration of model parameters by experimental responses that significantly deviate from their respective computed values would significantly modify the resulting adjusted parameters.

On the other hand, calibrating a parameter library by using measured responses that are very close to their respective computed values would cause minimal parameter modifications and a nearly perfect reproduction of the given responses by the adjusted library (as would be expected). In such a case, the given responses would be considered as being consistent with the parameter library, in contradistinction to adjustment by inconsistent experimental information, in which case the adjustment could fail because of inconsistencies. These considerations clearly underscore the need for using a quantitative indicator to measure the mutual and joint consistency of the information available for model calibration.

The minimum value, $Q_{min} \equiv Q\left(\boldsymbol{z}^{be}\right)$, can be readily computed by replacing $\boldsymbol{z}^{be}$ in the definition of $Q(\boldsymbol{z})$, cf. Eq. (1.04), and carrying out the respective algebra, to obtain

$$Q_{min} \equiv Q\left(\boldsymbol{z}^{be}\right) = \boldsymbol{d}^{\dagger}\left[\boldsymbol{C}_d\left(\boldsymbol{\alpha}^0\right)\right]^{-1}\boldsymbol{d}\,, \;\; \boldsymbol{d} \triangleq \boldsymbol{R}\left(\boldsymbol{\alpha}^0\right) - \boldsymbol{r}_m\,. \tag{1.48}$$

As the above expression indicates, $Q_{min} \equiv Q\left(\boldsymbol{z}^{be}\right)$ represents the square of the length of the vector $\boldsymbol{d}$, measuring (in the corresponding metric) the deviations between the experimental and nominally computed responses. Note that $Q_{min} \equiv Q\left(\boldsymbol{z}^{be}\right)$ can be evaluated directly from the given data (i.e., given parameters and responses, together with their original uncertainties) after having inverted the deviation-vector uncertainty matrix $\boldsymbol{C}_d\left(\boldsymbol{\alpha}^0\right)$. It is also very important to note that $Q_{min} \equiv Q\left(\boldsymbol{z}^{be}\right)$ *depends solely on the original data and can therefore be computed prior to the application of the data assimilation procedure*. As the dimension of $\boldsymbol{d}$ indicates, the number of degrees of freedom characteristic of the calibration under consideration is equal to the number of experimental responses. In the extreme case of absence of experimental responses, no actual calibration takes place since $\boldsymbol{d} = \boldsymbol{R}\left(\boldsymbol{\alpha}^0\right)$, so that the best-estimate parameter values are just the original nominal values, i.e., ; an actual adjustment occurs only when at least one experimental response is included.

Replacing Eq. (1.48) in Eq. (1.04) shows that the bulk of the contribution to the joint posterior probability distribution, which comes from the point , takes on the form of the following multivariate Gaussian distribution:

$$
\begin{aligned}
p\left(\boldsymbol{z}^{be} \mid \boldsymbol{C}\right) &\sim exp\left[-\frac{1}{2}Q\left(\boldsymbol{z}^{be}\right)\right] \\
&= exp\left\{-\frac{1}{2}\left[\boldsymbol{r}_x - \boldsymbol{R}\left(\boldsymbol{\alpha}^0\right)\right]^{\dagger}\left[\boldsymbol{C}_d\left(\boldsymbol{\alpha}^0\right)\right]^{-1}\left[\boldsymbol{r}_x - \boldsymbol{R}\left(\boldsymbol{\alpha}^0\right)\right]\right\}.
\end{aligned}
\tag{1.49}
$$

The above relation indicates that experimental responses can be considered as random variables approximately described by a multivariate Gaussian distribution with means located at the nominal values of the computed responses, and with a covariance matrix $\boldsymbol{C}_d\left(\boldsymbol{\alpha}^0\right)$. In turn, the random variable $Q_{min} \equiv Q\left(\boldsymbol{z}^{be}\right)$ obeys a χ^2-distribution with n degrees of freedom, where n denotes the total number of experimental responses considered in the calibration (adjustment) procedure. Since $Q_{min} \equiv Q\left(\boldsymbol{z}^{be}\right)$ is the "χ^2 of the calibration (adjustment) at hand," it can be used as an indicator of the agreement between the computed and experimental responses, measuring essentially the consistency of the experimental responses with the model parameters. Recall that the χ^2 (chi-square) distribution with n degrees of freedom of the continuous variable x, $0 \le x < \infty$, is defined as

$$\begin{aligned} &P\left(x<\chi^2<x+dx\right) \triangleq k_n(x)\,dx \\ &= \frac{1}{2^{n/2}\Gamma(n/2)} x^{n/2-1} e^{-x/2} dx,\ x>0,\ (n=1,2,\ldots). \end{aligned} \tag{1.50}$$

The χ^2-distribution is a measure of the deviation of a “true distribution” (in this case: the distribution of experimental responses) from the hypothetic one (in this case: a Gaussian). The mean and variance of x are $\langle x\rangle = n$ and $var(x) = 2n$, respectively. Further practically useful asymptotic properties of the χ^2-distribution for $n \to \infty$ are as follows: (i) x is asymptotically normal with mean n and variance $2n$; (ii) x/n is asymptotically normal with mean 1 and variance $2/n$; (iii) $\sqrt{2x}$ is asymptotically normal with mean $\sqrt{2n-1}$ and variance 1. Although the χ^2-distribution is extensively tabulated, the notation is not uniform in the literature for the various derived quantities (in particular, for the corresponding cumulative distribution functions and fractiles). The cumulative distributions, denoted here by $P_n\left(\chi^2\right)$ and $Q_n\left(\chi^2\right)$, are defined as

$$\begin{aligned} &P_n\left(\chi_0^2\right) \triangleq P\left(\chi^2 \le \chi_0^2\right) \triangleq \int_0^{\chi_0^2} k_n(t)\,dt; \\ &Q_n\left(\chi_0^2\right) \triangleq P\left(\chi^2 \ge \chi_0^2\right) \triangleq \int_{\chi_0^2}^{\infty} k_n(t)\,dt = 1 - P_n\left(\chi_0^2\right). \end{aligned} \tag{1.51}$$

In practice, one rejects a hypothesis using the χ^2-distribution when, for a given significance level α and number of degrees of freedom n, the value of $Q_{min} \equiv \chi^2$ exceeds a chosen critical fractile value $\chi_\alpha^2(n)$. Published tables often show $\chi_{1-\alpha}^2(n)$ versus α. When the number of degrees of freedom is large ($n > 30$), a useful asymptotic approximation is $\chi_\alpha^2(n) \approx 1/2\left(\sqrt{2n-1} + z_{2\alpha}\right)^2$, with $z_{2\alpha}$ denoting the corresponding fractile of the standard normal distribution $\Phi_0(z)$, computed by solving the equation $2\Phi_0\left(z_{2\alpha}\right) = 1 - 2\alpha$, using the tabulated tables for $\Phi_0(z)$. For large or small values of α, a more accurate approximation is $\chi_\alpha^2(n) \approx n\left(1 - \frac{2}{9m} + z_{2\alpha}\sqrt{\frac{2}{9m}}\right)^3$. It may be often more convenient to transform χ^2 to the variate $t = \chi^2/n$ (i.e., "χ^2 per degree of freedom"), in which case the transformed distribution, $g_n(t)$, becomes $g_n(t) = nk_n(nt)$, with mean value $\langle t \rangle = 1$ and variance $2/n$.

For model calibration (adjustment), it is important to assess if: (i) the response and data measurements are free of gross errors (blunders such as wrong settings, mistaken readings, etc.); and (ii) the measurements are consistent with the assumptions regarding the respective means, variances, and covariances. For example, if $\chi^2/n \simeq 1$, then the measurements are very likely to be both free of gross errors and consistent with the assumptions. However, if $\chi^2/n \gg 1$ or $\chi^2/n \ll 1$, the measurements (or at least some measurements), the assumptions, or both are suspect. In particular, unusually large values $\chi^2/n \gg 1$ could be obtained when the original variances are underestimated; increasing them beyond their assumed nominal values would cause the adjusted values of χ^2/n and $P_n(\chi^2)$ to decrease accordingly. The reverse argument would apply if the a priori values of χ^2/n and $P_n(\chi^2)$ were unusually small (e.g., $\chi^2/n \ll 1$, $P_n(\chi^2) \sim 10^{-4}$), which could stem from a priori overestimated variances. A practical quantitative criterion for the "acceptance" or "rejection" of experimental results in conjunction with a given "theoretical" model (i.e., in conjunction with the assumptions regarding the variates underlying the model) is to accept the value of χ^2/n whenever $0.15 < P_n(\chi^2) < 0.85$, in analogy to the $"1\sigma"$ range of normal distributions. Note that, when setting an acceptance criterion for χ^2/n of the general form

$$\alpha < P_n(\chi^2) < 1 - \alpha \,, \tag{1.52}$$

the exact value of α is not essential and is subject to personal judgment. This is because the probability $P_n(\chi^2)$ is still sensitive to the value of χ^2/n due to the fact that $\chi^2/n \simeq 1 \pm \sqrt{(2/n)}$ (except for few degrees of freedom, e.g., for $n \le 5$), so the acceptable range of χ^2/n narrows as $1/\sqrt{n}$ (see also the previously noted asymptotic forms for χ^2_α/n). In other words, moderate changes in χ^2/n lead to significant relative changes in $P_n(\chi^2)$. For example, the central 50%-range of $\chi^2/20$ is (0.77, 1.19), and the corresponding 90%-range is

(0.54, 1.57), implying that values of $\chi^2/20$ below $\simeq 0.4$ or above $\simeq 2.0$ would be definitely unacceptable.

In addition to measuring the overall consistency of a given set of parameters and responses, the quantity " χ^2/n " also measures the consistency among the measured responses. Hence, an entire data set (model parameters and/or experimental responses) should not be indiscriminately disqualified because of a "too high" or "too low" value of χ^2/n, since even a single "outlying" response could significantly degrade the set's overall consistency. Note that a simple-minded assessment and ranking of "questionable responses" according to the values of the "individual consistencies" (i.e., the values of χ^2 obtained for each response as if it were the only response available for calibrating the entire set of parameters), would be very likely misleading. This is because the sum of the respective "individual consistencies" [which would numerically be obtained by dividing the squares of the deviations, d_i^2, through the sum of the respective variances of the computed and measured responses $var\left(r_i^{comp}\right)+var\left(r_i^{exp}\right)$], would not be equal to the "joint consistency" (i.e., the joint χ^2) of the entire set of experimental responses. This is because the deviation-vector uncertainty matrix $\boldsymbol{C}_d\left(\boldsymbol{\alpha}^0\right) \triangleq \boldsymbol{C}_{rc}\left(\boldsymbol{\alpha}^0\right) - \boldsymbol{C}_{r\alpha}\left[\boldsymbol{S}\left(\boldsymbol{\alpha}^0\right)\right]^{\dagger} - \left[\boldsymbol{S}\left(\boldsymbol{\alpha}^0\right)\right]\boldsymbol{C}_{\alpha r} + \boldsymbol{C}_m$ is generally non-diagonal, even if both $\boldsymbol{C}_{rc}\left(\boldsymbol{\alpha}^0\right)$ and $\boldsymbol{C}_x$ are diagonal. On the other hand, verifying the consistency of all partial sets of the array of n responses with respect to their consistency with the given library is usually impractical, since the number of partial sets of an array of n responses is $2^n - 1$. Therefore, such a verification would be feasible in practice only when the number of measured responses is very small.

A procedure that has been successfully used to identify successively the responses which are least consistent with a given library of parameters is based on leaving out one response at a time and evaluating $\chi_{n-1}^2(1)$ for the remaining $n-1$ responses. The response left out is subsequently returned to the response set, another response (response "two") is eliminated, and the corresponding $\chi_{n-1}^2(2)$ is evaluated. This procedure is continued until all remaining $\chi_{n-1}^2(i), i = 3,\ldots,n,$ are successively evaluated. The response that yields the lowest χ_{n-1}^2 when eliminated is considered to be “the least consistent;” it is therefore ranked “last” in the consistency sequence and eliminated from further consideration. The evaluation procedure is then repeated for the remaining $n-1$ (“more consistent“) responses, to identify the “second least consistent response,” which is then ranked next-to-last. Subsequently, this procedure is repeatedly applied to the successive, fewer and fewer, partial response sets until establishing the complete consistency sequence. Establishing such a consistency sequence requires only $n(n+1)/2$ computations of χ^2, as compared to $\left(2^n-1\right)$ calculations needed to assign χ^2 values to all possible partial sets of n responses.

The quantity χ^2/n measures the consistency of any set of n experimentally measured responses with a given library of model parameters, in the sense that if χ_1^2 refers to a specific set of n experimental responses and χ_2^2 to another set of n responses, then $\chi_1^2 < \chi_2^2$ means that the first set is more consistent with the library than the second. On the other hand, when varying the number of responses, it is not a priori obvious whether the set yielding a smaller χ^2/n is also necessarily the most consistent with the given parameters. As an example, consider the value $P_n\left(\chi^2\right)=0.85$, which can correspond to both $\chi^2/5=1.623$ and also to $\chi^2/10=1.453$. If, for example, one set of 5 responses would give a computed value $\chi^2/5=1.6$, and second set of 10 responses would give $\chi^2/10=1.5$, the first set would be considered to be the “more consistent set,” for it falls within the “central 70% range,“ whereas the second set does not. In such situations, it is preferable to use the quantity $Q_n\left(\chi^2\right)=1-P_n\left(\chi^2\right)$, as an additional measure of consistency.

Quite generally, therefore, the calibration (adjustment) of a set of model parameters and experimental responses must include the verification of their mutual consistency, which is performed by first generating the consistency sequence, and then determining the probabilities $Q_i\left(\chi^2\right)$, when $i=1,2,\ldots,n$, while generating the sequence. The less consistent responses will show up at the end of the sequence, and the probabilities $Q_i\left(\chi^2\right)$ will generally decrease as i approaches the total number of responses, n. Such an analysis would identify the significantly less-consistent responses, and would also indicate the level of consistency of all response subsets along the consistency sequence.

In parallel, the irregular model parameters, if any, must also be identified. This can be done by computing χ^2 for any response subset, and using $\boldsymbol{\alpha}^{be} = \boldsymbol{\alpha}^0 + \left(\boldsymbol{C}_{\alpha r} - \boldsymbol{C}_{\alpha} \left[\boldsymbol{S}\left(\boldsymbol{\alpha}^0\right) \right]^{\dagger} \right) \left[\boldsymbol{C}_d \left(\boldsymbol{\alpha}^0\right) \right]^{-1} \boldsymbol{d}$ to compute the corresponding values for the best-estimate parameters. This way, the actual individual parameter adjustments induced by the respective response subset are also examined while proceeding step-by-step along the consistency sequence, noting which parameters vary more than others do, and by how much. Usually, the parameter-adjustments induced by the more consistent subsets of responses tend to be marginal. In contradistinction, the less-consistent responses and the questionable parameters would tend to undergo larger adjustments, requiring specific further examinations.

1.2 Time-Dependent Data Assimilation and Model Calibration

Following the work of [Cacuci and Ionescu-Bujor, 2010b], we consider that the time-dependent generic physical system comprises N_α^ν model parameters and N_r^ν distinct responses, respectively, at every time node $\nu = 1,2,\dots,N_t$. Hence, at every time node ν, the (column) vector $\boldsymbol{\alpha}^\nu$ of J_α^ν system parameters, and the (column) vector $\boldsymbol{r}^\nu$ of J_r^ν measured responses can be represented in component form as

$$\boldsymbol{\alpha}^\nu = \left\{\alpha_n^\nu \,|\, n = 1,\dots N_\alpha^\nu\right\}, \quad \boldsymbol{r}^\nu = \left\{r_i^\nu \,|\, i = 1,\dots,N_r^\nu\right\}, \ \nu = 1,\dots,N_t \tag{1.53}$$

At any time node ν, the system parameters are considered to be variates with mean values $\left(\boldsymbol{\alpha}^0\right)^\nu$. Furthermore, the correlations between two parameters α_i^ν and α_j^μ, at two time nodes μ and ν, have the general form

$$c_{\alpha,ij}^{\nu\mu} \equiv \left\langle \left[\alpha_i^\nu - \left(\alpha_i^\nu\right)^0\right]\left[\alpha_j^\mu - \left(\alpha_j^\mu\right)^0\right]\right\rangle \tag{1.54}$$

The above covariances constitute the elements of symmetric covariance matrices of the form

$$\boldsymbol{C}_\alpha^{\mu\nu} \triangleq \left\langle \left(\boldsymbol{\alpha} - \boldsymbol{\alpha}^0\right)^\mu \left[\left(\boldsymbol{\alpha} - \boldsymbol{\alpha}^0\right)^\nu\right]^\dagger \right\rangle = \left(\boldsymbol{C}_\alpha^{\mu\nu}\right)^\dagger = \boldsymbol{C}_\alpha^{\nu\mu} = \left(\boldsymbol{C}_\alpha^{\nu\mu}\right)^\dagger \tag{1.55}$$

Similarly, the measured responses are characterized by mean values $\left(\boldsymbol{r}_m\right)^\nu$ at a time node ν, and by symmetric covariance matrices between two time nodes μ and ν defined as

$$\boldsymbol{C}_m^{\mu\nu} \triangleq \left\langle \left(\boldsymbol{r} - \boldsymbol{r}_m\right)^\mu \left[\left(\boldsymbol{r} - \boldsymbol{r}_m\right)^\nu\right]^\dagger \right\rangle = \left(\boldsymbol{C}_m^{\mu\nu}\right)^\dagger = \boldsymbol{C}_m^{\nu\mu} = \left(\boldsymbol{C}_m^{\nu\mu}\right)^\dagger \tag{1.56}$$

In the most general case, the measured responses may be correlated to the parameters through symmetric response-parameter uncertainty matrices of the form

$$\boldsymbol{C}_{r\alpha}^{\mu\nu} \triangleq \left\langle \left(\boldsymbol{r}-\boldsymbol{r}_m\right)^{\mu}\left[\left(\boldsymbol{\alpha}-\boldsymbol{\alpha}^0\right)^{\nu}\right]^{\dagger}\right\rangle;\ \boldsymbol{C}_{\alpha r}^{\mu\nu} \triangleq \left\langle \left(\boldsymbol{\alpha}-\boldsymbol{\alpha}^0\right)^{\mu}\left[\left(\boldsymbol{r}-\boldsymbol{r}_m\right)^{\nu}\right]^{\dagger}\right\rangle . \tag{1.57}$$

Note that the matrices $\boldsymbol{C}_{r\alpha}^{\mu\nu}$ are not bona-fide variance-covariance matrices, in that they are not necessarily square positive matrices (often, they are rectangular), and the elements on their respective main diagonals (if they happen to be square) are also covariances (or correlations) rather that variances.

At any given time node ν, a response r_i^{ν} can be a function of not only the system parameters at time node ν, but also of the system parameters at all previous time nodes μ, $1 \leq \mu \leq \nu$; this means that $\boldsymbol{r}^{\nu} = \boldsymbol{R}^{\nu}\left(\boldsymbol{p}^{\nu}\right)$, where the vector $\boldsymbol{p}^{\nu} \triangleq \left(\boldsymbol{\alpha}^1,\ldots,\boldsymbol{\alpha}^{\mu},\ldots,\boldsymbol{\alpha}^{\nu}\right)$ has been introduced for notational convenience. In general, the response computed using the model depends nonlinearly and implicitly (in an analytically intractable form) on the model parameters. Furthermore, the uncertainties in parameters and modeling induce uncertainties in the computed responses, and can be computed either by means of statistical methods (for relatively simple models with few parameters) or deterministically, by using the propagation of moments (errors) method, as described by [Cacuci, 2003]. In this method, the computed response is linearized via a functional Taylor-series expansion around the nominal values, $\boldsymbol{p}_0^{\nu} \triangleq \left(\left(\boldsymbol{\alpha}^0\right)^1,\ldots,\left(\boldsymbol{\alpha}^0\right)^{\mu},\ldots,\left(\boldsymbol{\alpha}^0\right)^{\nu}\right)$, of the parameters $\boldsymbol{p}^{\nu}$, as follows:

$$\boldsymbol{r}^{\nu} = \boldsymbol{R}^{\nu}\left(\boldsymbol{p}^{\nu}\right) = \boldsymbol{R}^{\nu}\left(\boldsymbol{p}_0^{\nu}\right) + \sum_{\mu=1}^{\nu} \boldsymbol{S}^{\nu\mu}\left(\boldsymbol{p}_0^{\mu}\right)\left[\boldsymbol{\alpha}^{\mu} - \left(\boldsymbol{\alpha}^0\right)^{\mu}\right] + \ldots,\ \nu = 1,\ldots,N_t, \tag{1.58}$$

where $\boldsymbol{R}^{\nu}\left(\boldsymbol{p}_0^{\nu}\right)$ denotes the vector of computed responses at a time node ν, at the nominal parameter values $\boldsymbol{p}_0^{\nu}$, while $\boldsymbol{S}^{\nu\mu}\left(\boldsymbol{p}_0^{\mu}\right)$, $1 \leq \mu \leq \nu$, represents the $\left(J_r^{\nu} \times J_{\alpha}^{\mu}\right)$-dimensional matrix containing the first Gateaux-derivatives of the computed responses with respect to the parameters, defined as

$$\boldsymbol{S}^{\nu\mu}\left(\boldsymbol{p}_0^{\mu}\right) \triangleq \begin{pmatrix} s_{11}^{\nu\mu} & \cdots & s_{1N}^{\nu\mu} \\ \vdots & s_{in}^{\nu\mu} & \vdots \\ s_{I1}^{\nu\mu} & \cdots & s_{IN}^{\nu\mu} \end{pmatrix} \triangleq \begin{pmatrix} \dfrac{\partial R_1^{\nu}\left(\boldsymbol{p}_0^{\mu}\right)}{\partial \alpha_1^{\mu}} & \cdots & \dfrac{\partial R_1^{\nu}\left(\boldsymbol{p}_0^{\mu}\right)}{\partial \alpha_N^{\mu}} \\ \vdots & \dfrac{\partial R_i^{\nu}}{\partial \alpha_n^{\mu}} & \vdots \\ \dfrac{\partial R_I^{\nu}\left(\boldsymbol{p}_0^{\mu}\right)}{\partial \alpha_1^{\mu}} & \cdots & \dfrac{\partial R_I^{\nu}\left(\boldsymbol{p}_0^{\mu}\right)}{\partial \alpha_N^{\mu}} \end{pmatrix}, \quad 1 \le \mu \le \nu, \tag{1.59}$$

Since the response $\boldsymbol{R}^{\nu}\left(\boldsymbol{p}_0^{\nu}\right)$ at time node ν can depend only on parameters $\left(\boldsymbol{\alpha}^0\right)^{\mu}$ which appear up to the current time node ν, it follows that $\boldsymbol{S}^{\nu\mu} = \boldsymbol{0}$ when $\mu > \nu$, and hence non-zero terms in the expansion shown in (1.58) can only occur in the range $1 \le \mu \le \nu$. It is important to note that discretization parameters are also included among the components of $\boldsymbol{\alpha}$, and the sensitivities of responses to such discretization parameters can be computed as described in [Cacuci ,2003].

By introducing the block matrix

$$\boldsymbol{S} \triangleq \begin{pmatrix} \boldsymbol{S}^{11} & \cdots & \boldsymbol{0} \\ \vdots & \ddots & \vdots \\ \boldsymbol{S}^{N_t 1} & \cdots & \boldsymbol{S}^{N_t N_t} \end{pmatrix}, \tag{1.60}$$

and the (block) column vectors

$$\boldsymbol{\alpha} \triangleq \left(\boldsymbol{\alpha}^{1}, \ldots, \boldsymbol{\alpha}^{\mu}, \ldots, \boldsymbol{\alpha}^{N_t}\right), \tag{1.61}$$

$$\boldsymbol{r} \triangleq \left(\boldsymbol{r}^{1}, \ldots, \boldsymbol{r}^{\mu}, \ldots, \boldsymbol{r}^{N_t}\right), \tag{1.62}$$

$$\boldsymbol{R}\left(\boldsymbol{\alpha}^{0}\right) \triangleq \left(\boldsymbol{R}^{1}, \ldots, \boldsymbol{R}^{\mu}, \ldots, \boldsymbol{R}^{N_t}\right), \tag{1.63}$$

the system shown in (1.58) can be written in the form

$$\boldsymbol{r} = \boldsymbol{R}\left(\boldsymbol{\alpha}^0\right) + \boldsymbol{S}\left(\boldsymbol{\alpha} - \boldsymbol{\alpha}^0\right) + \textit{higher order terms} \tag{1.64}$$

Applying the propagation of errors method to (1.64), which involves the formal integration of the over the unknown joint distributions of the parameters $\boldsymbol{\alpha}$, yields the following expressions for the expectation value, $\langle \boldsymbol{r} \rangle$, of the response $\boldsymbol{r}$, and the corresponding covariance matrix, $\boldsymbol{C}_{rc}\left(\boldsymbol{\alpha}^0\right)$, of the computed responses, i.e.,

$$\langle \boldsymbol{r} \rangle = \boldsymbol{R}\left(\boldsymbol{\alpha}^0\right), \tag{1.65}$$

and

$$\boldsymbol{C}_{rc}\left(\boldsymbol{\alpha}^0\right) \triangleq \left\langle \delta \boldsymbol{r} \delta \boldsymbol{r}^{\dagger} \right\rangle = \left[\boldsymbol{S}\left(\boldsymbol{\alpha}^0\right)\right] \left\langle \delta \boldsymbol{\alpha} \delta \boldsymbol{\alpha}^{\dagger} \right\rangle \left[\boldsymbol{S}\left(\boldsymbol{\alpha}^0\right)\right]^{\dagger} = \left[\boldsymbol{S}\left(\boldsymbol{\alpha}^0\right)\right] \boldsymbol{C}_{\alpha} \left[\boldsymbol{S}\left(\boldsymbol{\alpha}^0\right)\right]^{\dagger}. \tag{1.66}$$

The covariance matrix of the computed responses, $\boldsymbol{C}_{rc}$, has the symmetric structure

$$\boldsymbol{C}_{rc} \triangleq \begin{pmatrix} \boldsymbol{C}_{rc}^{11} & \cdots & \boldsymbol{C}_{rc}^{1N_t} \\ \vdots & \ddots & \vdots \\ \boldsymbol{C}_{rc}^{N_t 1} & \cdots & \boldsymbol{C}_{rc}^{N_t N_t} \end{pmatrix},$$

with components defined as

$$\boldsymbol{C}_{rc}^{\nu\mu} = \sum_{\eta=1}^{\nu} \sum_{\rho=1}^{\mu} \boldsymbol{S}^{\nu\eta} \boldsymbol{C}_{\alpha}^{\eta\rho} \left(\boldsymbol{S}^{\mu\rho}\right)^{\dagger} = \left(\boldsymbol{C}_{rc}^{\mu\nu}\right)^{\dagger}; \quad \nu, \mu = 1, \ldots, N_t. \tag{1.67}$$

As indicated by (1.65), the expectation value of the computed responses for linearized models in which the numerical errors are neglected is given by the value of the response computed at the nominal parameter-values.

According to the maximum entropy algorithm described in [Cacuci and Ionescu-Bujor, 2010b] to the computational and experimental information described in (1.53) through (1.67) indicates that the most objective probability distribution for this information is a multivariate Gaussian of the form

$$p(z\,|\,\boldsymbol{C})\,d(z) = \frac{exp\left[-\frac{1}{2}Q(\boldsymbol{z})\right]}{det(2\pi\boldsymbol{C})^{1/2}}\,d(\boldsymbol{z})\,,\; Q(\boldsymbol{z}) \equiv \boldsymbol{z}^{\dagger}\,\boldsymbol{C}^{-1}\boldsymbol{z}\,, -\infty < z_j < \infty\,, \tag{1.68}$$

where:

$$\boldsymbol{z} \equiv \begin{pmatrix} \boldsymbol{\alpha} - \boldsymbol{\alpha}^0 \\ \boldsymbol{r} - \boldsymbol{r}_m \end{pmatrix}, \boldsymbol{\alpha}^0 \triangleq \left(\left(\boldsymbol{\alpha}^0\right)^1, \ldots, \left(\boldsymbol{\alpha}^0\right)^{\mu}, \ldots, \left(\boldsymbol{\alpha}^0\right)^{N_t} \right), \tag{1.69}$$

$$\boldsymbol{C} \equiv \begin{pmatrix} \boldsymbol{C}_{\alpha} & \boldsymbol{C}_{\alpha r} \\ \boldsymbol{C}_{r\alpha} & \boldsymbol{C}_{m} \end{pmatrix}, \tag{1.70}$$

with

$$\boldsymbol{C}_{\alpha} = \begin{pmatrix} \boldsymbol{C}_{\alpha}^{11} & \boldsymbol{C}_{\alpha}^{12} & \ldots & \ldots \\ \boldsymbol{C}_{\alpha}^{21} & \boldsymbol{C}_{\alpha}^{22} & \ldots & \ldots \\ \ldots & \ldots & \ldots & \ldots \\ \ldots & \ldots & \ldots & \boldsymbol{C}_{\alpha}^{N_tN_t} \end{pmatrix}, \; \boldsymbol{C}_{\alpha r} = \begin{pmatrix} \boldsymbol{C}_{\alpha r}^{11} & \boldsymbol{C}_{\alpha r}^{12} & \ldots & \ldots \\ \boldsymbol{C}_{\alpha r}^{21} & \boldsymbol{C}_{\alpha r}^{22} & \ldots & \ldots \\ \ldots & \ldots & \ldots & \ldots \\ \ldots & \ldots & \ldots & \boldsymbol{C}_{\alpha r}^{N_tN_t} \end{pmatrix}, \; \boldsymbol{C}_{m} = \begin{pmatrix} \boldsymbol{C}_{m}^{11} & \boldsymbol{C}_{m}^{12} & \ldots & \ldots \\ \boldsymbol{C}_{m}^{21} & \boldsymbol{C}_{m}^{22} & \ldots & \ldots \\ \ldots & \ldots & \ldots & \ldots \\ \ldots & \ldots & \ldots & \boldsymbol{C}_{m}^{N_tN_t} \end{pmatrix}.$$

The posterior information, which is contained in (1.68) and (1.64), can now be condensed into a recommended best-estimate value $\left(\boldsymbol{z}^{be}\right)^{\nu}$ at a time node ν for the parameters $\boldsymbol{\alpha}^{\nu}$ and responses $\boldsymbol{r}^{\nu}$, together with corresponding best-estimate recommended uncertainties for these quantities. The procedure for obtaining these best-estimate results is formally similar to that leading to Eq. (1.11)

Subsequent computations are facilitated by recasting (1.64) in the form

$$\boldsymbol{Z}\left(\boldsymbol{\alpha}^0\right)\boldsymbol{z} + \boldsymbol{d} = \boldsymbol{0}\,,\;\; \boldsymbol{d} \triangleq \boldsymbol{R}\left(\boldsymbol{\alpha}^0\right) - \boldsymbol{r}_m\,, \tag{1.71}$$

where $\boldsymbol{r}_m \triangleq \left(\boldsymbol{r}_m^1,\ldots,\boldsymbol{r}_m^\mu,\ldots,\boldsymbol{r}_m^{N_t}\right)$ is the vector comprising all of the experimentally measured responses, $\boldsymbol{d} \triangleq \boldsymbol{R}\left(\boldsymbol{\alpha}^0\right) - \boldsymbol{r}_m$ is a vector of "deviations" reflecting the discrepancies between the nominal computations and the nominally measured responses, while $\boldsymbol{Z}$ denotes the partitioned matrix

$$\boldsymbol{Z} \triangleq \left(\boldsymbol{S} \quad \boldsymbol{U}\right); \quad \boldsymbol{U} \triangleq \begin{pmatrix} -\boldsymbol{I}^{11} & \cdots & \boldsymbol{0} \\ \vdots & \ddots & \vdots \\ \boldsymbol{0} & \cdots & -\boldsymbol{I}^{N_t N_t} \end{pmatrix}, \tag{1.72}$$

where $\boldsymbol{I}^{\nu\nu}, \nu = 1,\ldots,N_t,$ denotes the identity matrix of corresponding dimensions.

Computing the stationary point of $Q(\boldsymbol{z})$ subject to (1.71) poses a constrained minimization problem which can be solved by introducing Lagrange multipliers, $\boldsymbol{\lambda}$, to construct the augmented Lagrangian functional $P(\boldsymbol{z},\boldsymbol{\lambda})$ defined as

$$P(\boldsymbol{z},\boldsymbol{\lambda}) \equiv Q(\boldsymbol{z}) + 2\boldsymbol{\lambda}^\dagger\left[\boldsymbol{Z}\left(\boldsymbol{\alpha}^0\right)\boldsymbol{z} + \boldsymbol{d}\right] = min, \ at \ \boldsymbol{z} = \boldsymbol{z}^{be} \equiv \begin{pmatrix} \boldsymbol{\alpha}^{be} - \boldsymbol{\alpha}^0 \\ \boldsymbol{r}^{be} - \boldsymbol{r}_m \end{pmatrix}. \tag{1.73}$$

where $\boldsymbol{\lambda} = \left(\boldsymbol{\lambda}^1,\ldots,\boldsymbol{\lambda}^\nu,\ldots,\boldsymbol{\lambda}^{N_t}\right)$ denotes the corresponding vector of Lagrange multipliers. In the above expression, the superscript "be" denotes "best-estimated values", and the factor "2" was introduced for convenience in front of $\boldsymbol{\lambda}$ in order to simplify the subsequent algebraic derivations. The point $\boldsymbol{z}^{be}$ where the functional $P(\boldsymbol{z},\boldsymbol{\lambda})$ attains its extremum (minimum) is defined implicitly through the conditions

$$\nabla_z P(\boldsymbol{z},\boldsymbol{\lambda}) = \boldsymbol{0}, \quad \nabla_\lambda P(\boldsymbol{z},\boldsymbol{\lambda}) = \boldsymbol{0}, \quad at \ \boldsymbol{z} = \boldsymbol{z}^{be}. \tag{1.74}$$

The solution to the above constrained minimization problem leads to the following final results for the predictive best-estimate parameters, responses, and their corresponding reduced uncertainties (covariance matrices) are as follows:

1. The best-estimate predicted nominal values for the calibrated (adjusted) parameters:

$$\boldsymbol{\alpha}^{be} = \boldsymbol{\alpha}^0 + \left(\boldsymbol{C}_{\alpha r} - \boldsymbol{C}_{\alpha} \left[\boldsymbol{S}\left(\boldsymbol{\alpha}^0\right) \right]^{\dagger} \right) \left[\boldsymbol{C}_d \left(\boldsymbol{\alpha}^0 \right) \right]^{-1} \boldsymbol{d} \, . \tag{1.75}$$

In component form, the above expression for the calibrated best-estimate parameter values becomes

$$\left(\boldsymbol{\alpha}^{be}\right)^{\nu} = \left(\boldsymbol{\alpha}^0\right)^{\nu} + \sum_{\mu=1}^{N_t} \left\{ \left[\boldsymbol{C}_{\alpha r}^{\nu\mu} - \sum_{\rho=1}^{\mu} \boldsymbol{C}_{\alpha}^{\nu\rho} \left(\boldsymbol{S}^{\dagger}\right)^{\mu\rho} \right] \left[\sum_{\eta=1}^{N_t} \boldsymbol{K}_d^{\mu\eta} \boldsymbol{d}^{\eta} \right] \right\}, \quad \nu = 1,\dots,N_t , \tag{1.76}$$

where $\boldsymbol{K}_d^{\nu\eta}$ denotes the corresponding (ν,η)-element of the block-matrix $\boldsymbol{C}_d^{-1}$, with the block-matrix $\boldsymbol{C}_d\left(\boldsymbol{\alpha}^0\right)$ defined as follows:

$$\begin{aligned} \boldsymbol{C}_d\left(\boldsymbol{\alpha}^0\right) &\triangleq \left\langle \boldsymbol{d}\boldsymbol{d}^{\dagger} \right\rangle = \left\langle \left(\delta\boldsymbol{r} - \boldsymbol{S}\left(\boldsymbol{\alpha}^0\right) \delta\boldsymbol{\alpha} \right) \left(\delta\boldsymbol{r}^{\dagger} - \delta\boldsymbol{\alpha}^{\dagger} \left[\boldsymbol{S}\left(\boldsymbol{\alpha}^0\right) \right]^{\dagger} \right) \right\rangle \\ &= \boldsymbol{C}_{rc}\left(\boldsymbol{\alpha}^0\right) - \boldsymbol{C}_{r\alpha} \left[\boldsymbol{S}\left(\boldsymbol{\alpha}^0\right) \right]^{\dagger} - \left[\boldsymbol{S}\left(\boldsymbol{\alpha}^0\right) \right] \boldsymbol{C}_{\alpha r} + \boldsymbol{C}_m . \end{aligned} \tag{1.77}$$

In component form, the matrix $\boldsymbol{C}_d$ is expressed as

$$\begin{aligned} \boldsymbol{C}_d \triangleq \begin{pmatrix} \boldsymbol{C}_d^{11} & \cdots & \boldsymbol{C}_d^{1N_t} \\ \vdots & \ddots & \vdots \\ \boldsymbol{C}_d^{N_t 1} & \cdots & \boldsymbol{C}_d^{N_t N_t} \end{pmatrix} &= \begin{pmatrix} \boldsymbol{C}_{rc}^{11} + \boldsymbol{C}_m^{11} & \cdots & \boldsymbol{C}_{rc}^{1N_t} + \boldsymbol{C}_m^{1N_t} \\ \vdots & \ddots & \vdots \\ \boldsymbol{C}_{rc}^{N_t 1} + \boldsymbol{C}_m^{N_t 1} & \cdots & \boldsymbol{C}_{rc}^{N_t N_t} + \boldsymbol{C}_m^{N_t N_t} \end{pmatrix} \\ &- \begin{pmatrix} \boldsymbol{C}_{r\alpha}^{11} \left(\boldsymbol{S}^{\dagger}\right)^{11} + \boldsymbol{S}^{11} \boldsymbol{C}_{\alpha r}^{11} & \cdots & \boldsymbol{S}^{11} \boldsymbol{C}_{\alpha r}^{1N_t} + \sum_{\rho=1}^{N_t} \boldsymbol{C}_{r\alpha}^{1\rho} \left(\boldsymbol{S}^{\dagger}\right)^{N_t \rho} \\ \vdots & \ddots & \vdots \\ \boldsymbol{C}_{r\alpha}^{N_t 1} \left(\boldsymbol{S}^{\dagger}\right)^{11} + \sum_{\rho=1}^{N_t} \boldsymbol{S}^{N_t \rho} \boldsymbol{C}_{\alpha r}^{\rho 1} & \cdots & \sum_{\rho=1}^{N_t} \left[\boldsymbol{C}_{r\alpha}^{N_t \rho} \left(\boldsymbol{S}^{\dagger}\right)^{N_t \rho} + \boldsymbol{S}^{N_t \rho} \boldsymbol{C}_{\alpha r}^{\rho N_t} \right] \end{pmatrix} . \end{aligned} \tag{1.78}$$

2. The best-estimate predicted nominal values for the calibrated (adjusted) responses:

$$\boldsymbol{r}\left(\boldsymbol{\alpha}^{be}\right) = \boldsymbol{r}_m + \left(\boldsymbol{C}_m - \boldsymbol{C}_{r\alpha} \left[\boldsymbol{S}\left(\boldsymbol{\alpha}^0\right) \right]^{\dagger} \right) \left[\boldsymbol{C}_d \left(\boldsymbol{\alpha}^0 \right) \right]^{-1} \boldsymbol{d} \, . \tag{1.79}$$

At a specific time node ν, each component $\left(\boldsymbol{r}^{be}\right)^{\nu}$ of $\boldsymbol{r}\left(\boldsymbol{\alpha}^{be}\right)$ has the explicit form

$$\left(\boldsymbol{r}^{be}\right)^{\nu} = \left(\boldsymbol{r}_m\right)^{\nu} + \sum_{\mu=1}^{N_t}\left\{\left[\boldsymbol{C}_m^{\nu\mu} - \sum_{\rho=1}^{\mu}\boldsymbol{C}_{r\alpha}^{\nu\rho}\left(\boldsymbol{S}^{\dagger}\right)^{\mu\rho}\right]\left[\sum_{\eta=1}^{N_t}\boldsymbol{K}_d^{\mu\eta}\boldsymbol{d}^{\eta}\right]\right\}, \quad \nu = 1,\ldots,N_t. \qquad (1.80)$$

3. The expressions for the best-estimate predicted covariances $\boldsymbol{C}_{\alpha}^{be}$ and $\boldsymbol{C}_{r}^{be}$, corresponding to the best-estimate parameters $\boldsymbol{\alpha}^{be}$ and responses $\boldsymbol{r}\left(\boldsymbol{\alpha}^{be}\right)$, together with the predicted best-estimate parameter-response covariance matrix $\boldsymbol{C}_{\alpha r}^{be}$:

$$\begin{aligned}\boldsymbol{C}_{\alpha}^{be} &\triangleq \left\langle\left(\boldsymbol{\alpha}-\boldsymbol{\alpha}^{be}\right)\left(\boldsymbol{\alpha}-\boldsymbol{\alpha}^{be}\right)^{\dagger}\right\rangle \\ &= \boldsymbol{C}_{\alpha} - \left[\boldsymbol{C}_{\alpha d}\left(\boldsymbol{\alpha}^{0}\right)\right]\left[\boldsymbol{C}_{d}\left(\boldsymbol{\alpha}^{0}\right)\right]^{-1}\left[\boldsymbol{C}_{\alpha d}\left(\boldsymbol{\alpha}^{0}\right)\right]^{\dagger},\end{aligned} \qquad (1.81)$$

$$\begin{aligned}\boldsymbol{C}_{r}^{be} &\triangleq \left\langle\left(\boldsymbol{r}-\boldsymbol{r}\left(\boldsymbol{\alpha}^{be}\right)\right)\left(\boldsymbol{r}-\boldsymbol{r}\left(\boldsymbol{\alpha}^{be}\right)\right)^{\dagger}\right\rangle \\ &= \boldsymbol{C}_{m} - \left[\boldsymbol{C}_{rd}\left(\boldsymbol{\alpha}^{0}\right)\right]\left[\boldsymbol{C}_{d}\left(\boldsymbol{\alpha}^{0}\right)\right]^{-1}\left[\boldsymbol{C}_{rd}\left(\boldsymbol{\alpha}^{0}\right)\right]^{\dagger},\end{aligned} \qquad (1.82)$$

$$\begin{aligned}\boldsymbol{C}_{r\alpha}^{be} = \boldsymbol{C}_{\alpha r}^{be} &\triangleq \left\langle\left(\boldsymbol{\alpha}-\boldsymbol{\alpha}^{be}\right)\left(\boldsymbol{r}-\boldsymbol{r}\left(\boldsymbol{\alpha}^{be}\right)\right)^{\dagger}\right\rangle \\ &= \boldsymbol{C}_{r\alpha} - \left[\boldsymbol{C}_{rd}\left(\boldsymbol{\alpha}^{0}\right)\right]\left[\boldsymbol{C}_{d}\left(\boldsymbol{\alpha}^{0}\right)\right]^{-1}\left[\boldsymbol{C}_{\alpha d}\left(\boldsymbol{\alpha}^{0}\right)\right]^{\dagger},\end{aligned} \qquad (1.83)$$

where

$$\boldsymbol{C}_{rd}\left(\boldsymbol{\alpha}^{0}\right) \triangleq \left\langle\left(\boldsymbol{r}-\boldsymbol{r}_m\right)\boldsymbol{d}^{\dagger}\right\rangle = \left(\boldsymbol{C}_{m} - \boldsymbol{C}_{r\alpha}\left[\boldsymbol{S}\left(\boldsymbol{\alpha}^{0}\right)\right]^{\dagger}\right), \qquad (1.84)$$

and

$$\boldsymbol{C}_{\alpha d}\left(\boldsymbol{\alpha}^{0}\right) \triangleq \left\langle\left(\boldsymbol{\alpha}-\boldsymbol{\alpha}^{0}\right)\boldsymbol{d}^{\dagger}\right\rangle = \left(\boldsymbol{C}_{\alpha r} - \boldsymbol{C}_{\alpha}\left[\boldsymbol{S}\left(\boldsymbol{\alpha}^{0}\right)\right]^{\dagger}\right). \qquad (1.85)$$

For completeness, the block-matrix components, which correlate two (distinct or not) time-nodes, of the above calibrated best-estimate covariance matrices are given below:

$$\left(\boldsymbol{C}_{\alpha}^{be}\right)^{\nu\mu} = \boldsymbol{C}_{\alpha}^{\nu\mu} - \sum_{\eta=1}^{N_t}\sum_{\rho=1}^{N_t}\left[\boldsymbol{C}_{\alpha r}^{\nu\rho} - \sum_{\pi=1}^{\rho}\boldsymbol{C}_{\alpha}^{\nu\pi}\left(\boldsymbol{S}^{\dagger}\right)^{\rho\pi}\right]\boldsymbol{K}_{d}^{\rho\eta}\left[\boldsymbol{C}_{r\alpha}^{\eta\mu} - \sum_{\pi=1}^{\eta}\boldsymbol{S}^{\eta\pi}\boldsymbol{C}_{\alpha}^{\pi\mu}\right], \tag{1.86}$$

$$\left(\boldsymbol{C}_{r}^{be}\right)^{\nu\mu} = \boldsymbol{C}_{m}^{\nu\mu} - \sum_{\eta=1}^{N_t}\sum_{\rho=1}^{N_t}\left[\boldsymbol{C}_{m}^{\nu\rho} - \sum_{\pi=1}^{\rho}\boldsymbol{C}_{r\alpha}^{\nu\pi}\left(\boldsymbol{S}^{\dagger}\right)^{\rho\pi}\right]\boldsymbol{K}_{d}^{\rho\eta}\left[\boldsymbol{C}_{m}^{\eta\mu} - \sum_{\pi=1}^{\eta}\boldsymbol{S}^{\eta\pi}\boldsymbol{C}_{\alpha r}^{\pi\mu}\right], \tag{1.87}$$

$$\left(\boldsymbol{C}_{r\alpha}^{be}\right)^{\nu\mu} = \boldsymbol{C}_{r\alpha}^{\nu\mu} - \sum_{\eta=1}^{N_t}\sum_{\rho=1}^{N_t}\left[\boldsymbol{C}_{m}^{\nu\rho} - \sum_{\pi=1}^{\rho}\boldsymbol{C}_{r\alpha}^{\nu\pi}\left(\boldsymbol{S}^{\dagger}\right)^{\rho\pi}\right]\boldsymbol{K}_{d}^{\rho\eta}\left[\boldsymbol{C}_{\alpha r}^{\eta\mu} - \sum_{\pi=1}^{\eta}\boldsymbol{S}^{\eta\pi}\boldsymbol{C}_{\alpha}^{\pi\mu}\right]. \tag{1.88}$$

Note in Eq. (1.81) that a symmetric positive matrix is subtracted from the initial parameter covariance matrix $\boldsymbol{C}_{\alpha}$; hence, in this sense, the best-estimate predicted parameter uncertainty matrix $\boldsymbol{C}_{\alpha}^{be}$ has been reduced by the calibration (adjustment) procedure, through the introduction of new information from experiments. Similarly, a symmetric positive matrix is subtracted in (1.82) from the initial covariance matrix $\boldsymbol{C}_{m}$ of the experimental-responses; hence, the best-estimate predicted response covariance matrix $\boldsymbol{C}_{r}^{be}$ has been improved (reduced) through the introduction of new experimental information. Furthermore, (1.83) indicates that the calibration (adjustment) procedure will introduce correlations between the calibrated (adjusted) parameters and responses even if the parameters and response were initially uncorrelated, since $\boldsymbol{C}_{r\alpha}^{be} \neq 0$ even if $\boldsymbol{C}_{r\alpha} = 0$, i.e.,

$$\boldsymbol{C}_{r\alpha}^{be} = \boldsymbol{C}_{m}\left[\boldsymbol{C}_{rc}\left(\boldsymbol{\alpha}^{0}\right) + \boldsymbol{C}_{m}\right]^{-1}\left[\boldsymbol{S}\left(\boldsymbol{\alpha}^{0}\right)\right]\boldsymbol{C}_{\alpha}, \text{ when } \boldsymbol{C}_{r\alpha} = 0\,. \tag{1.89}$$

As the above expression indicates, the adjustment (calibration) modifies the correlations among the parameters through couplings introduced by the sensitivities of the participating responses. In the calibration procedure, the sensitivities play the role of weighting functions for propagating the initial parameter-covariances and experimental-response covariances to the adjusted best-estimate predicted quantities. Thus, as indicated by Eqs. (1.81) through (1.83), the incorporation of additional (experimental) information in the adjustment (calibration) process reduces the variances of the adjusted parameters and responses while also modifying their correlations. Furthermore, all of the considerations following Eq. (1.34) are also valid for the time-dependent formalism, since all of the corresponding expressions are formally identical. In particular, $\boldsymbol{C}_{rc}^{be} \neq \boldsymbol{C}_{r}^{be}$ since $\boldsymbol{S}\left(\boldsymbol{\alpha}^{be}\right) \neq \boldsymbol{S}\left(\boldsymbol{\alpha}^{0}\right)$, in general, except when the model is linear and "perfect" (i.e., free of errors).

In view of Eq. (1.78), it is essential to note that the inverse matrix, $\boldsymbol{C}_{d}^{-1}$, incorporates simultaneously all of the available information about the system parameters and responses, at all time nodes [i.e., $\nu = 1,2,...,N_t$]. Specifically, at any time node ν, $\boldsymbol{C}_{d}^{-1}$ incorporates information not only from time nodes prior in time to ν (i.e., information regarding the "past" and "present" states of the system) but also from time nodes posterior in time to ν (i.e., information about the "future" states of the system). Through the matrix $\boldsymbol{C}_{d}^{-1}$, at any specified time node ν, the calibrated best-estimates parameters $\left(\boldsymbol{\alpha}^{be}\right)^{\nu}$ and responses $\boldsymbol{r}\left(\boldsymbol{\alpha}^{be}\right) \triangleq \boldsymbol{r}^{be}$, together with the corresponding calibrated best-estimate covariance matrices $\left(\boldsymbol{C}_{\alpha}^{be}\right)^{\nu\mu}$, $\left(\boldsymbol{C}_{r}^{be}\right)^{\nu\mu}$, and $\left(\boldsymbol{C}_{\alpha r}^{be}\right)^{\nu\mu}$ will also incorporate automatically all of the available information about the system parameters and responses at all time nodes [i.e., $\nu = 1,2,...,N_t$].

In this respect, the methodology presented in this section is conceptually related to the "foresight" aspects encountered in decision analysis. It is also important to note that, in practice, the application of the methodology developed in this section involves two distinct computational stages. A complete sensitivity data base (i.e., sensitivities $s_{ni}^{\nu\mu}$ at all times nodes $\nu,\mu = 1,\ldots,N_t$) needs to be generated "off-line" prior to performing the "data assimilation" and "model calibration" (or data adjustment) stages. All sensitivities are subsequently combined with appropriate covariance matrices to compute calibrated best-estimate responses, parameters, and best-estimate covariance matrices.

Because of the "foresight" and "off-line" characteristics, the methodology presented in this Section can be called the "off-line with foresight" data assimilation and adjustment (model calibration) methodology, underscoring that all sensitivities are generated separately, prior to performing the uncertainty analysis, and that foresight characteristics are included in the calibration procedure. Since the incorporation of foresight effects involves the inversion of the matrix $\boldsymbol{C}_d$, this methodology is best suited for problems involving relatively few time nodes. For large-scale highly nonlinear problems involving many time nodes, the matrix $\boldsymbol{C}_d$ becomes very large, requiring large amounts of computer storage; the inversion of $\boldsymbol{C}_d$ may become prohibitively expensive in such cases. These difficulties can be reduced at the expense of using less than the complete information available at any specific time node. For example, even in time-dependent problems in which the entire time history is known (e.g., transient behavior of reactor systems), one may nevertheless choose to use only information up to the current time index, and disregard the information about "future" system states.

On the other hand, in dynamical problems such as climate or weather prediction, in which the time variable advances continuously and states beyond the current time are not known, information about future states cannot be reliably accounted for anyway. Thus, the most common way of reducing the dimensionality of the data assimilation and model calibration problem is to disregard information about future states and limit the amount of information assimilated about "past states". Data assimilation and model calibration procedure using such a limited amount of information can be performed either off-line or on-line, assimilating the new data as the time index advances.

The simplest case of dynamic data assimilation and model calibration is when these operations are performed by using information on-line from only two successive time-steps. In this particular case, the expressions given by Eqs. (1.76), (1.80), (1.86), (1.87) and (1.88) for the best-estimate predicted calibrated quantities reduce to the following explicit formulas:

(i) The components $\left(\boldsymbol{\alpha}^{be}\right)^k$, representing the calibrated best-estimates for the system parameters at time node k, can be written in a particular form of Eq. (1.76), as follows:

$$\left(\boldsymbol{\alpha}^{be}\right)^k = \left(\boldsymbol{\alpha}^{0}\right)^k + \sum_{\mu=k-1}^{k} \left\{ \left[\boldsymbol{C}_{\alpha r}^{k\mu} - \sum_{\rho=k-1}^{\mu} \boldsymbol{C}_{\alpha}^{k\rho} \left(\boldsymbol{S}^{\dagger}\right)^{\mu\rho} \right] \left[\sum_{\eta=k-1}^{k} \boldsymbol{K}_{d}^{\mu\eta} \boldsymbol{d}^{\eta} \right] \right\}, \quad k = 1,2,...,N_t. \qquad (1.90)$$

(ii) The vector $\left(\boldsymbol{r}^{be}\right)^{k}$, representing the best-estimates predicted values for the system responses at a time node k, take on the following particular form of Eq. (1.80):

$$\left(\boldsymbol{r}^{be}\right)^{k}=\left(\boldsymbol{r}_{m}\right)^{k}+\sum_{\mu=k-1}^{k}\left\{\left[\boldsymbol{C}_{m}^{k\mu}-\sum_{\rho=k-1}^{\mu}\boldsymbol{C}_{r\alpha}^{k\rho}\left(\boldsymbol{S}^{\dagger}\right)^{\mu\rho}\right]\left[\sum_{\eta=k-1}^{k}\boldsymbol{K}_{d}^{\mu\eta}\boldsymbol{d}^{\eta}\right]\right\},\quad k=1,2,...,N_{t}. \tag{1.91}$$

(iii) The components $\left(\boldsymbol{C}_{\alpha}^{be}\right)^{\nu\mu}$, $\left(\nu,\mu=k-1,k\right)$, of the calibrated best-estimate covariance matrix, $\boldsymbol{C}_{\alpha}^{be}$, for the calibrated best-estimates system parameters is obtained by particularizing Eq. (1.86) to two consecutive time nodes $\left(k-1,k\right)$, $k=1,2,...,N_{t}$, leading to

$$\begin{gathered}\left(\boldsymbol{C}_{\alpha}^{be}\right)^{\nu\mu}=\boldsymbol{C}_{\alpha}^{\nu\mu}-\sum_{\eta=k-1}^{k}\sum_{\rho=k-1}^{k}\left[\boldsymbol{C}_{\alpha r}^{\nu\rho}-\sum_{\pi=k-1}^{\rho}\boldsymbol{C}_{\alpha}^{\nu\pi}\left(\boldsymbol{S}^{\dagger}\right)^{\rho\pi}\right]\boldsymbol{K}_{d}^{\rho\eta}\left[\boldsymbol{C}_{r\alpha}^{\eta\mu}-\sum_{\pi=k-1}^{\eta}\boldsymbol{S}^{\eta\pi}\boldsymbol{C}_{\alpha}^{\pi\mu}\right], \\ for\quad \nu=k-1,k;\quad and\quad \mu=k-1,k;\quad k=1,2,...,N_{t}.\end{gathered} \tag{1.92}$$

(iv). The components $\left(\boldsymbol{C}_{r}^{be}\right)^{\nu\mu}$, $\left(\nu,\mu=k-1,k\right)$, of the calibrated best-estimate covariance matrix $\boldsymbol{C}_{r}^{be}$, for the best-estimate responses takes on the following particular form of Eq. (1.87):

$$\begin{gathered}\left(\boldsymbol{C}_{r}^{be}\right)^{\nu\mu}=\boldsymbol{C}_{m}^{\nu\mu}-\sum_{\eta=k-1}^{k}\sum_{\rho=k-1}^{k}\left[\boldsymbol{C}_{m}^{\nu\rho}-\sum_{\pi=k-1}^{\rho}\boldsymbol{C}_{r\alpha}^{\nu\pi}\left(\boldsymbol{S}^{\dagger}\right)^{\rho\pi}\right]\boldsymbol{K}_{d}^{\rho\eta}\left[\boldsymbol{C}_{m}^{\eta\mu}-\sum_{\pi=k-1}^{\eta}\boldsymbol{S}^{\eta\pi}\boldsymbol{C}_{\alpha r}^{\pi\mu}\right], \\ for\quad \nu=k-1,k;\quad and\quad \mu=k-1,k;\quad k=1,2,...,N_{t}.\end{gathered} \tag{1.93}$$

(v). The components $\left(\boldsymbol{C}_{r\alpha}^{be}\right)^{\nu\mu}$, $\left(\nu,\mu=k-1,k\right)$, of the best-estimate response-parameter covariance matrix $\boldsymbol{C}_{\alpha r}^{be}$ take on the following particular form of Eq. (1.88):

$$\begin{gathered}\left(\boldsymbol{C}_{r\alpha}^{be}\right)^{\nu\mu}=\boldsymbol{C}_{r\alpha}^{\nu\mu}-\sum_{\eta=k-1}^{k}\sum_{\rho=k-1}^{k}\left[\boldsymbol{C}_{m}^{\nu\rho}-\sum_{\pi=k-1}^{\rho}\boldsymbol{C}_{r\alpha}^{\nu\pi}\left(\boldsymbol{S}^{\dagger}\right)^{\rho\pi}\right]\boldsymbol{K}_{d}^{\rho\eta}\left[\boldsymbol{C}_{r\alpha}^{\eta\mu}-\sum_{\pi=k-1}^{\eta}\boldsymbol{S}^{\eta\pi}\boldsymbol{C}_{\alpha}^{\pi\mu}\right] \\ for\quad \nu=k-1,k;\quad and\quad \mu=k-1,k;\quad k=1,2,...,N_{t}.\end{gathered} \tag{1.94}$$

For each time node, $k = 1,2,...,N_t$, the quantities $\boldsymbol{K}_d^{\nu\eta}$ which appear in Eq. (1.90) through (1.94) have the following expressions:

$$\begin{aligned}\boldsymbol{K}_d^{k-1,k-1} &= \left[\boldsymbol{C}_d^{k-1,k-1} - \boldsymbol{C}_d^{k-1,k}\left(\boldsymbol{C}_d^{k,k}\right)^{-1}\boldsymbol{C}_d^{k,k-1}\right]^{-1} \\ &= \left(\boldsymbol{C}_d^{k-1,k-1}\right)^{-1} + \left(\boldsymbol{C}_d^{k-1,k-1}\right)^{-1}\boldsymbol{C}_d^{k-1,k}\boldsymbol{K}_d^{k,k}\boldsymbol{C}_d^{k,k-1}\left(\boldsymbol{C}_d^{k-1,k-1}\right)^{-1}\end{aligned} \tag{1.95}$$

$$\begin{aligned}\boldsymbol{K}_d^{k-1,k} &= -\left(\boldsymbol{C}_d^{k-1,k-1}\right)^{-1}\boldsymbol{C}_d^{k-1,k}\left[\boldsymbol{C}_d^{k,k} - \boldsymbol{C}_d^{k,k-1}\left(\boldsymbol{C}_d^{k-1,k-1}\right)^{-1}\boldsymbol{C}_d^{k-1,k}\right]^{-1} \\ &= -\left(\boldsymbol{C}_d^{k-1,k-1}\right)^{-1}\boldsymbol{C}_d^{k-1,k}\boldsymbol{K}_d^{k,k}\end{aligned} \tag{1.96}$$

$$\begin{aligned}\boldsymbol{K}_d^{k,k} &= \left[\boldsymbol{C}_d^{k,k} - \boldsymbol{C}_d^{k,k-1}\left(\boldsymbol{C}_d^{k-1,k-1}\right)^{-1}\boldsymbol{C}_d^{k-1,k}\right]^{-1} \\ &= \left(\boldsymbol{C}_d^{k,k}\right)^{-1} + \left(\boldsymbol{C}_d^{k,k}\right)^{-1}\boldsymbol{C}_d^{k,k-1}\boldsymbol{K}_d^{k-1,k-1}\boldsymbol{C}_d^{k-1,k}\left(\boldsymbol{C}_d^{k,k}\right)^{-1}\end{aligned} \tag{1.97}$$

$$\begin{aligned}\boldsymbol{K}_d^{k,k-1} &= -\left(\boldsymbol{C}_d^{k,k}\right)^{-1}\boldsymbol{C}_d^{k,k-1}\left[\boldsymbol{C}_d^{k-1,k-1} - \boldsymbol{C}_d^{k-1,k}\left(\boldsymbol{C}_d^{k,k}\right)^{-1}\boldsymbol{C}_d^{k,k-1}\right]^{-1} \\ &= -\left(\boldsymbol{C}_d^{k,k}\right)^{-1}\boldsymbol{C}_d^{k,k-1}\boldsymbol{K}_d^{k-1,k-1}\end{aligned} \tag{1.98}$$

For time-independent problems, the (time-dependent) results derived in Eqs. (1.90) through (1.94) reduce to expressions that are formally identical to Eqs. (1.75), (1.79), (1.81), (1.82) and (1.83). Hence, the later expressions can be used directly to obtain the best-estimate predicted values for parameters, responses, and their respective covariances. Recall that modeling errors can be treated in a manner similar to parameter uncertainties, by including the discretization intervals among the components of the vector $\boldsymbol{\alpha}$ of model parameters, as detailed in [Cacuci , 2003].

Finally, it is important to emphasize that the explicit formulas presented in this Section are based on the linearized relationship between responses and parameters that customarily underlies the "propagation of moments" method, i.e., Eq. (1.64), without considering nonlinearities explicitly. Nevertheless, this limitation is not as severe as it may appear at first glance, since nonlinear relations between computed responses and model parameters can be treated by considering Eq. (1.64) iteratively, starting with the known nominal values of the quantities involved. The first iteration (in such an iterative procedure) would yield all of the major explicit results derived in Eqs. (1.75), (1.79), (1.81), (1.82) and (1.83) .The subsequent iteration would the results of Eqs (1.75), (1.79), (1.81), (1.82) and (1.83) as the "prior information" in a second application of these formulas, and compute the new ("second-iteration") best-estimate quantities by using once again these formulas. This iterative procedure would be continued until the best-estimated values would converge within a small, user-specified, convergence criterion. The actual application of the model calibration (adjustment) algorithms –see Eqs. (1.75), (1.79), (1.81), (1.82) and (1.83), to a physical system is straightforward, in principle, although it can become computationally very demanding in terms of data handling and computational speed requirements.

Just as for the time-independent case discussed in Section 1.1.1, the expression $Q\left(\boldsymbol{z}^{be}\right)=\boldsymbol{d}^{\dagger}\left[\boldsymbol{C}_d\left(\boldsymbol{\alpha}^0\right)\right]^{-1}\boldsymbol{d}$ measures (in the corresponding metric) the deviations between the experimental and nominally computed responses, and can be evaluated directly from the given data (i.e., given parameters and responses, together with their original uncertainties) after having inverted the deviation-vector uncertainty matrix $\boldsymbol{C}_d\left(\boldsymbol{\alpha}^0\right)$. This quantity obeys a χ^2 -distribution with n degrees of freedom, where n denotes the total number of experimental responses considered in the calibration (adjustment) procedure, and indicates the degree of agreement between the computed and experimental responses, measuring essentially the consistency of the experimental responses with the model parameters. For model calibration (adjustment), it is important to assess if: (i) the response and data measurements are free of gross errors (blunders such as wrong settings, mistaken readings, etc), and (ii) the measurements are consistent with the assumptions regarding the respective means, variances, and covariances. As has been noted by [Cacuci and Ionescu-Bujor, 2010a], when the distance between any two nominal response values, $\left|R_i^0-R_j^0\right|$, is smaller or at least not much larger than the sum of the corresponding uncertainties, say $\sigma_i+\sigma_j$, the data is considered to be consistent or to agree "within error bars". However, if the distances $\left|R_i^0-R_j^0\right|$ are larger than $\left(\sigma_j+\sigma_k\right)$, the data are considered to be inconsistent or discrepant. Inconsistencies can be caused by unrecognized or ill-corrected experimental effects (e.g., background, dead time of the counting electronics, instrumental resolution, sample impurities, calibration errors, etc,). Note that the probability that two equally precise measurements yield a separation greater than $\sigma_i + \sigma_j = 2\sigma$ is very small, namely $erfc(1) \simeq 0.157$ for Gaussian sampling distributions with standard deviation σ. Thus, although there is a nonzero probability that genuinely discrepant data do occur, it is much more likely that apparently discrepant experiments actually indicate the presence of unrecognized errors, an issue addressed in the recent work of [Cacuci and Ionescu-Bujor, 2010a].

The *consistency indicator expression* $Q(\boldsymbol{z}^{be}) = \boldsymbol{d}^{\dagger}\left[\boldsymbol{C}_d(\boldsymbol{\alpha}^0)\right]^{-1}\boldsymbol{d}$ *together with Eqs. (1.75), (1.79), (1.81), (1.82) and (1.83) have been programmed into a computational software module called **BEST-EST***, based on the conceptual framework of [ROOT CERN]. This computational software module will be used for the time-dependent applications to be presented in Section III of this work.

2 Time Independent Data Assimilation and Model Calibration: Paradigm Examples

2.1 Neutron Diffusion in One Dimensional Geometry

In this Section, the main features methodology presented in Section 1.1 will be illustrated using a paradigm application to a *steady-state* neutron diffusion problem.

2.1.1 Mathematical Formulation

Consider the diffusion of monoenergetic neutrons due to distributed sources of strength S $\text{neutrons}/\text{cm}^3 \cdot \text{s}$ within a slab of material of extrapolated thickness $2a$. The linear neutron diffusion equation that models mathematically this problem is

$$D\frac{d^2\varphi}{dx^2} - \Sigma_a\varphi + S = 0\,, \quad x \in (-a,a)\,, \tag{2.1}$$

where $\varphi(x)$ is the neutron flux, D is the diffusion coefficient, Σ_a is the macroscopic absorption cross section, and S is the distributed source term. Note that, in view of the problem's symmetry, the origin $x = 0$ has been conveniently chosen at the middle (center) of the slab. The boundary conditions for Eq. (2.1) are that the neutron flux must vanish at the extrapolated distance, i.e.,

$$\varphi(\pm a) = 0\,. \tag{2.2}$$

A typical response R for the neutron diffusion problem modeled by Eqs. (2.1) and (2.2) would be the reading of a detector placed within the slab, for example, at a distance b from the slab's midline at $x = 0$. Such a response is given by the reaction rate

$$R(\boldsymbol{e}) \equiv \Sigma_d\varphi(b)\,, \tag{2.3}$$

where Σ_d represents the detector's equivalent reaction cross section. The system parameters for this problem are thus the positive constants Σ_a, D, S, and Σ_d, which will be considered to be the components of the vector $\boldsymbol{\alpha}$ of system parameters, defined as

$$\boldsymbol{\alpha} \equiv \left(\Sigma_a, D, S, \Sigma_d\right). \tag{2.4}$$

Consider that the components of $\boldsymbol{\alpha} \equiv \left(\Sigma_a, D, S, \Sigma_d\right)$ are imprecisely (e.g., experimentally) determined quantities, with mean nominal values $\boldsymbol{\alpha}^0 = \left(\Sigma_a^0, D^0, S^0, \Sigma_d^0\right)$ and standard deviations $\boldsymbol{h}_\alpha \triangleq \left(\delta\Sigma_a, \delta D, \delta S, \delta\Sigma_d\right)$, respectively. The vector $\boldsymbol{e}(x)$ appearing in the functional dependence of R in Eq. (2.3) denotes the concatenation of $\varphi(x)$ with $\boldsymbol{\alpha}$, defined as

$$\boldsymbol{e} \equiv \left(\varphi, \boldsymbol{\alpha}\right). \tag{2.5}$$

The nominal value $\varphi^0(x)$ of the flux is determined by solving Eqs. (2.1) and (2.2) for the nominal parameter values $\boldsymbol{\alpha}^0 = \left(\Sigma_a^0, D^0, S^0, \Sigma_d^0\right)$, to obtain

$$\varphi^0(x) = \frac{S^0}{\Sigma_a^0}\left(1 - \frac{\cosh xk}{\cosh ak}\right), \quad k \equiv \sqrt{\Sigma_a^0 / D^0}, \tag{2.6}$$

where $k \equiv \sqrt{\Sigma_a^0 / D^0}$ is the nominal value of the reciprocal diffusion length for our illustrative example. Inserting Eq. (2.6) together with the nominal value Σ_d^0 into Eq. (2.3) gives the nominal response

$$R\left(\boldsymbol{e}^0\right) = \frac{S^0 \Sigma_d^0}{\Sigma_a^0}\left(1 - \frac{\cosh bk}{\cosh ak}\right), \quad \boldsymbol{e}^0 \equiv \left(\varphi^0, \boldsymbol{\alpha}^0\right). \tag{2.7}$$

Note that even though Eq. (2.1) is linear in φ, the solution $\varphi(x)$ depends nonlinearly on $\boldsymbol{\alpha}$, as evidenced by Eq. (2.6). The same is true of the response $R(\boldsymbol{e})$. Even though $R(\boldsymbol{e})$ is linear separately in φ and in $\boldsymbol{\alpha}$, as shown in Eq. (2.3), R is not simultaneously linear in φ and $\boldsymbol{\alpha}$, which leads to a nonlinear dependence of $R(\boldsymbol{e})$ on $\boldsymbol{\alpha}$. This fact is confirmed by the explicit expression of $R(\boldsymbol{e})$ given in Eq. (2.7).

Recalling next that

$$\boldsymbol{h}_\alpha \equiv \left(\delta\Sigma_a, \delta D, \delta S, \delta\Sigma_d\right), \tag{2.8}$$

we can compute the sensitivities of the response $R(\boldsymbol{e})$ to the variations $\boldsymbol{h}_\alpha$, which are given by the G-differential $\delta R\left(\boldsymbol{e}^0;\boldsymbol{h}\right)$ of $R(\boldsymbol{e})$ at $\boldsymbol{e}^0$ to variations

$$\boldsymbol{h} \triangleq \left(h_\varphi, \boldsymbol{h}_\alpha\right). \tag{2.9}$$

By definition, the G-differential $\delta R\left(\boldsymbol{e}^0;\boldsymbol{h}\right)$ of $R(\boldsymbol{e})$ at $\boldsymbol{e}^0$ is

$$\delta R\left(\boldsymbol{e}^0;\boldsymbol{h}\right) \equiv \frac{d}{d\varepsilon}\left\{R\left(\boldsymbol{e}^0+\varepsilon\boldsymbol{h}\right)\right\}_{\varepsilon=0}. \tag{2.10}$$

Hence, the explicit form of the G-differential of $R(\boldsymbol{e})$ defined in Eq. (2.3) becomes

$$\begin{aligned}\delta R\left(\boldsymbol{e}^0;\boldsymbol{h}\right) &\equiv \frac{d}{d\varepsilon}\left\{\left(\Sigma_d^0+\varepsilon\delta\Sigma_d\right)\left[\varphi^0(b)+\varepsilon h_\varphi(b)\right]\right\}_{\varepsilon=0} \\ &= R'_\alpha\left(\boldsymbol{e}^0\right)\boldsymbol{h}_\alpha + R'_\varphi\left(\boldsymbol{e}^0\right)h_\varphi ,\end{aligned} \tag{2.11}$$

where the “direct-effect” term $R'_\alpha \boldsymbol{h}_\alpha$ is defined as

$$R'_\alpha\left(\boldsymbol{e}^0\right)\boldsymbol{h}_\alpha \triangleq \delta\Sigma_d\varphi^0(b), \tag{2.12}$$

while the “indirect-effect” term $R'_\varphi h_\varphi$ is defined as

$$R'_\varphi\left(\boldsymbol{e}^0\right)h_\varphi \equiv \Sigma_d^0\, h_\varphi\left(b\right). \tag{2.13}$$

As indicated by Eq. (2.11), the operator $\delta R\left(\boldsymbol{e}^0;\boldsymbol{h}\right)$ is linear in $\boldsymbol{h}$; in particular, $R'_\varphi h_\varphi$ is a linear operator on h_φ. This linear dependence of $\delta R\left(\boldsymbol{e}^0;\boldsymbol{h}\right)$ on $\boldsymbol{h}$ is underscored by writing henceforth $DR\left(\boldsymbol{e}^0;\boldsymbol{h}\right)$ to denote the sensitivity of $R\left(\boldsymbol{e}\right)$ at $\boldsymbol{e}^0$ to variations $\boldsymbol{h}$. The “direct-effect” term $R'_\alpha\,\boldsymbol{h}_\alpha$ can be evaluated at this stage by replacing Eq. (2.6) into Eq. (2.12), to obtain

$$R'_\alpha\left(\boldsymbol{e}^0\right)\boldsymbol{h}_\alpha = \delta\Sigma_d\,\frac{S^0}{\Sigma_a^0}\left(1-\frac{\cosh bk}{\cosh ak}\right). \tag{2.14}$$

The “indirect-effect” term $R'_\varphi h_\varphi$, though, cannot be evaluated at this stage, since $h_\varphi\left(x\right)$ is not yet available. The first-order in $\left\|\boldsymbol{h}_\alpha\right\|$, the expression of $h_\varphi\left(x\right)$ is obtained by calculating the G-differentials of Eqs. (2.12) and (2.13), and then solving the resulting equations. The G-differentials of Eqs. (2.12) and (2.13) yield the “forward sensitivity equations” (or “tangent linear model”)

$$L\left(\boldsymbol{\alpha}^0\right)h_\varphi + \left[L'_\alpha\left(\boldsymbol{\alpha}^0\right)\varphi^0\right]\boldsymbol{h}_\alpha = O\left(\left\|\boldsymbol{h}_\alpha\right\|^2\right), \tag{2.15}$$

together with the boundary conditions

$$h_\varphi\left(\pm a\right)=0\,. \tag{2.16}$$

In Eq. (2.15), the operator $L\left(\boldsymbol{\alpha}^0\right)$ is defined as

$$L\left(\boldsymbol{\alpha}^0\right) \equiv D^0\frac{d^2}{dx^2}-\Sigma_a^0\,, \tag{2.17}$$

while the quantity

$$\left[L'_{\alpha}\left(\boldsymbol{\alpha}^{0}\right)\varphi^{0}\right]\boldsymbol{h}_{\alpha}\equiv\delta D\frac{d^{2}\varphi^{0}}{dx^{2}}-\delta\Sigma_{a}\varphi^{0}+\delta S\ , \tag{2.18}$$

which is the partial G-differential of $L\varphi$ at $\boldsymbol{\alpha}^0$ with respect to $\boldsymbol{\alpha}$, contains all of the first-order parameter variations $\boldsymbol{h}_{\alpha}$. Solving Eq. (2.15) yields the solution

$$\begin{aligned}h_{\varphi}\left(x\right)&=C_{1}\left(cosh\,xk-cosh\,ak\right)\\&+C_{2}\left(x\,sinh\,xk\,cosh\,ak-a\,sinh\,ak\,cosh\,xk\right),\end{aligned} \tag{2.19}$$

where the constants C_1 and C_2 are defined as

$$C_{1}\equiv\frac{\left(\delta\Sigma_{a}S^{0}/\Sigma_{a}^{0}-\delta S\right)}{\Sigma_{a}^{0}\left(cosh\,ak\right)}\ , \tag{2.20}$$

and, respectively,

$$C_{2}\equiv\frac{\left(\delta D/D^{0}-\delta\Sigma_{a}/\Sigma_{a}^{0}\right)S^{0}}{2\sqrt{D^{0}\Sigma_{a}^{0}}\left(cosh\,ak\right)^{2}}\ . \tag{2.21}$$

Evaluating Eq. (2.19) at $x=b$ and replacing the resulting expression in Eq. (2.13) gives the “indirect-effect” term as

$$\begin{aligned}R'_{\varphi}\left(\boldsymbol{e}^{0}\right)h_{\varphi}&=\Sigma_{d}^{0}C_{1}\left(cosh\,bk-cosh\,ak\right)\\&+\Sigma_{d}^{0}C_{2}\left(b\,sinh\,bk\,cosh\,ak-a\,sinh\,ak\,cosh\,bk\right).\end{aligned} \tag{2.22}$$

As generally shown by Cacuci (2003), the need to solve repeatedly the forward sensitivity equations for each component of $\boldsymbol{h}_{\alpha}$ can be circumvented by using the Adjoint Sensitivity Analysis Procedure (ASAP). The first prerequisite for applying the ASAP is that the "indirect-effect" term $R'_\varphi\left(\boldsymbol{e}^0\right)h_\varphi$ be expressible as a linear functional of h_φ. An examination of Eq. (2.13) readily reveals that $R'_\varphi\left(\boldsymbol{e}^0\right)h_\varphi$ is indeed a linear functional of h_φ. Therefore, $R'_\varphi\left(\boldsymbol{e}^0\right)h_\varphi$ can be represented as an inner product in an appropriately defined Hilbert space H_u. For this example, the appropriate space is the real Hilbert space $\mathsf{H}_u \equiv \mathsf{L}_2\left(\Omega\right)$, with $\Omega \equiv \left(-a,a\right)$, equipped with the inner product

$$\left\langle f\left(x\right), g\left(x\right)\right\rangle \equiv \int_{-a}^{a} f\left(x\right)g\left(x\right)dx\,, \qquad for\ f,g \in \mathsf{H}_u \equiv \mathsf{L}_2\left(\Omega\right),\quad \Omega \equiv \left(-a,a\right). \tag{2.23}$$

In $\mathsf{H}_u \equiv \mathsf{L}_2\left(\Omega\right)$, the linear functional $R'_\varphi\left(\boldsymbol{e}^0\right)h_\varphi$ defined in Eq. (2.13) can be represented as the inner product

$$\begin{aligned} R'_\varphi\left(\boldsymbol{e}^0\right)h_\varphi &\equiv \Sigma_d^0\, h_\varphi\left(b\right) = \int_{-a}^{a} \Sigma_d^0\, h_\varphi\left(x\right)\,\delta\left(x-b\right)dx \\ &= \left\langle \Sigma_d^0 \delta\left(x-b\right), h_\varphi\right\rangle . \end{aligned} \tag{2.24}$$

The next step underlying the ASAP is the construction of the operator $L^+\left(\boldsymbol{\alpha}^0\right)$ that is formally adjoint to $L\left(\boldsymbol{\alpha}^0\right)$. In view of Eq. (2.17), the formal adjoint of $L\left(\boldsymbol{\alpha}^0\right)$ is the operator

$$L^+\left(\boldsymbol{\alpha}^0\right) \equiv D^0 \frac{d^2}{dx^2} - \Sigma_a^0\,. \tag{2.25}$$

Note that $L^+\left(\boldsymbol{\alpha}^0\right)$ and $L\left(\boldsymbol{\alpha}^0\right)$ are formally self-adjoint. The qualifier "formally" must still be kept at this stage, since the boundary conditions for $L^+\left(\boldsymbol{\alpha}^0\right)$ have not been determined yet. The boundary conditions for $L^+\left(\boldsymbol{\alpha}^0\right)$ are obtained as

$$\int_{-a}^{a} \psi(x)\left[D^0 \frac{d^2 h_\varphi}{dx^2} - \Sigma_a^0 h_\varphi(x)\right] dx = \int_{-a}^{a} \left[D^0 \frac{d^2 \psi(x)}{dx^2} - \Sigma_a^0 \psi(x)\right] h_\varphi(x)\, dx \\ + \left\{ P\left[h_\varphi, \psi\right] \right\}_{x=-a}^{x=a} . \tag{2.26}$$

Note that the function $\psi(x)$ is still arbitrary at this stage, except for the requirement that $\psi \in \mathsf{H}_Q = \mathsf{L}_2(\Omega)$; note also that the Hilbert spaces H_u and H_Q have now both become the same space, i.e., $\mathsf{H}_u = \mathsf{H}_Q = \mathsf{L}_2(\Omega)$.

Integrating the left-side of Eq. (2.26) by parts twice and canceling terms yields the following expression for the bilinear boundary form:

$$\left\{ P\left[h_\varphi, \psi\right] \right\}_{-a}^{a} = D^0 \left[\psi \frac{dh_\varphi}{dx} - h_\varphi \frac{d\psi}{dx} \right]_{-a}^{a} . \tag{2.27}$$

Since h_φ is known at $x = \pm a$ from Eq. (2.16) the boundary conditions for $L^+(\boldsymbol{\alpha}^0)$ can now be selected as

$$\psi(\pm a) = 0 , \tag{2.28}$$

which ensures that unknown values of h_φ, such as the derivatives $\left\{ dh_\varphi / dx \right\}_{-a}^{a}$, would be eliminated from the bilinear form $\left\{ P\left[h_\varphi, \psi\right] \right\}_{-a}^{a}$ in Eq. (2.27). Note that the implementation of both Eqs. (2.28) and (2.16) into Eq. (2.27) actually causes $\left\{ P\left[h_\varphi, \psi\right] \right\}_{-a}^{a}$ to vanish.

Since the boundary conditions selected in Eq. (2.28) for the adjoint function $\psi(x)$ are the same as the boundary conditions for $h_\varphi(x)$ in Eq. (2.16), and since the operators $L^+(\boldsymbol{\alpha}^0)$ and $L(\boldsymbol{\alpha}^0)$ are formally self-adjoint, we can at this stage drop the qualifier “formally,” and can now conclude that the operators $L^+(\boldsymbol{\alpha}^0)$ and $L(\boldsymbol{\alpha}^0)$ are indeed self-adjoint.

The last step in the construction of the adjoint system is the identification of the source term, which shows that

$$\nabla_{\varphi} R\left(\boldsymbol{e}^0\right) = \Sigma_d^0 \delta\left(x-b\right), \tag{2.39}$$

so that the complete adjoint system becomes

$$L^{+}\left(\boldsymbol{\alpha}^0\right)\psi \equiv D^0 \frac{d^2\psi}{dx^2} - \Sigma_a^0 \psi\left(x\right) = \Sigma_d^0 \delta\left(x-b\right), \tag{2.30}$$

where the adjoint function $\psi\left(x\right)$ is subject to the boundary conditions $\psi\left(\pm a\right)=0$, as shown in Eq. (2.16). Recalling that $\delta Q = 0$ and $\hat{P}=0$ for our example, and using Eq. (2.18) gives the following expression for the "indirect-effect" term $R'_{\varphi}\left(\boldsymbol{e}^0\right)h_{\varphi}$:

$$R'_{\varphi}\left(\boldsymbol{e}^0\right)h_{\varphi} = -\int_{-a}^{a} \psi\left(x\right)\left[\delta D \frac{d^2\varphi^0}{dx^2} - \delta\Sigma_a \varphi^0\left(x\right) + \delta S\right] dx\,, \tag{2.31}$$

where $\psi\left(x\right)$ is the solution of the adjoint sensitivity system defined by Eqs. (2.30) and (2.28).

As expected, the adjoint sensitivity system is independent of parameter variations $\boldsymbol{h}_{\alpha}$, so it needs to be solved only once to obtain the adjoint function $\psi\left(x\right)$. Very important, too, is the fact (characteristic of linear systems) that the adjoint system is independent of the original solution $\varphi^0\left(x\right)$, and can therefore be solved directly, without any knowledge of the neutron flux $\varphi\left(x\right)$. Of course, the adjoint system depends on the response, which provides the source term. Solving the adjoint system for our illustrative example yields the following expression for the adjoint function $\psi\left(x\right)$:

$$\psi\left(x\right) = \frac{\Sigma_d^0}{\sqrt{\Sigma_a^0 D^0}}\left[\frac{\sinh\left(b-a\right)k}{\sinh 2ak}\sinh\left(x+a\right)k + H\left(x-b\right)\sinh\left(x-b\right)k\right], \tag{2.32}$$

where $H\left(x-b\right)$ is the Heaviside-step functional defined as

$$H\left(x\right)=\begin{cases}0\,, & for\; x<0\\ 1\,, & for\; x\geq 0\end{cases}. \tag{2.33}$$

Using Eq. (2.32) in Eq. (2.31) and carrying out the respective integrations over x yields, as expected, the same expression for the "indirect-effect" term $R'_{\varphi}\left(\boldsymbol{e}^{0}\right)h_{\varphi}$ as obtained in Eq. (2.22). Finally, the local sensitivity $DR\left(\boldsymbol{e}^{0};\boldsymbol{h}\right)$ of $R\left(\boldsymbol{e}\right)$ at $\boldsymbol{e}^{0}$ to variations $\boldsymbol{h}_{\alpha}$ in the system parameters is obtained from Eqs. (2.11), (2.14), and either Eq. (2.22) provided by the FSAP or, alternatively, using the adjoint function in Eq. (2.31), as provided by the ASAP; either way, the final expression of the sensitivity $DR\left(\boldsymbol{e}^{0};\boldsymbol{h}\right)$ is

$$\begin{aligned}DR\left(\boldsymbol{e}^{0};\boldsymbol{h}\right)=\delta\Sigma_{d}\frac{S^{0}}{\Sigma_{a}^{0}}&\left(1-\frac{cosh\,bk}{cosh\,ak}\right)\\ &+\Sigma_{d}^{0}\Big[C_{1}\left(cosh\,bk-cosh\,ak\right)\\ &+C_{2}\left(b\,sinh\,bk\,cosh\,ak-a\,sinh\,ak\,cosh\,bk\right)\Big].\end{aligned} \tag{2.34}$$

It is instructive to compare the expression of the local sensitivity $DR\left(\boldsymbol{e}^{0};\boldsymbol{h}\right)$ with the expression of the exact variation

$$\left(\Delta R\right)_{exact}\equiv R\left(\boldsymbol{e}^{0}+\boldsymbol{h}\right)-R\left(\boldsymbol{e}^{0}\right), \tag{2.35}$$

which would be induced in the response $R\left(\boldsymbol{e}\right)$ by parameter variations $\boldsymbol{h}_{\alpha}$. The exact variation $\left(\Delta R\right)_{exact}$ is readily obtained from Eq. (2.07) as

$$\left(\Delta R\right)_{exact}=\frac{S^{0}+\delta S}{\Sigma_{a}^{0}+\delta\Sigma_{a}}\left(\Sigma_{d}^{0}+\delta\Sigma_{d}\right)\left(1-\frac{cosh\,bk_{p}}{cosh\,ak_{p}}\right)-R\left(\boldsymbol{e}^{0}\right), \tag{2.36}$$

where

$$k_p \equiv \sqrt{\left(\Sigma_a^0 + \delta\Sigma_a\right)/\left(D^0 + \delta D\right)}. \tag{2.37}$$

On the other hand, we can solve exactly the perturbed equation

$$L\left(\boldsymbol{\alpha}^0 + \boldsymbol{h}_\alpha\right)\left[\varphi^0 + h_\varphi^{exact}\left(x\right)\right] + \left(S^0 + \delta S\right) = 0\,, \tag{2.38}$$

subject to the boundary conditions given by Eq. (2.16), to obtain

$$\begin{aligned} h_\varphi^{exact}\left(x\right) = & \frac{S^0\,\delta\Sigma_a/\Sigma_a^0 - \delta S}{\left(\Sigma_a^0 + \delta\Sigma_a\right)\,\cosh ak_p}\left(\cosh xk_p - \cosh ak_p\right) \\ & + S^0\,\frac{\cosh\left(ak_p\right)\cosh\left(xk\right) - \cosh\left(ak\right)\cosh\left(xk_p\right)}{\Sigma_a^0 \cosh ak_p \cosh ak}. \end{aligned} \tag{2.39}$$

Comparing Eq. (2.39) to Eq. (2.19) readily confirms that the solution $h_\varphi\left(x\right)$ of the forward sensitivity equations is the first-order, in $\left\|\boldsymbol{h}_\alpha\right\|$, approximation of $h_\varphi^{exact}\left(x\right)$, i.e.,

$$h_\varphi^{exact}\left(x\right) = h_\varphi\left(x\right) + O\left(\left\|\boldsymbol{h}_\alpha\right\|^2\right). \tag{2.40}$$

Similarly, comparing Eq. (2.36) to Eq. (2.34) confirms, as expected, that the local sensitivity $DR\left(\boldsymbol{e}^0;\boldsymbol{h}\right)$ is the first-order, in $\left\|\boldsymbol{h}_\alpha\right\|$, approximation of the exact response variation, namely:

$$R\left(\boldsymbol{e}^0 + \boldsymbol{h}\right) = R\left(\boldsymbol{e}^0\right) + DR\left(\boldsymbol{e}^0;\boldsymbol{h}\right) + O\left(\left\|\boldsymbol{h}_\alpha\right\|^2\right). \tag{2.41}$$

Actually, it can be shown that the functional Taylor-series of $R\left(\boldsymbol{e}^0 + \boldsymbol{h}\right)$ contains three terms only, namely

$$R\left(\boldsymbol{e}^0+\boldsymbol{h}\right)=R\left(\boldsymbol{e}^0\right)+DR\left(\boldsymbol{e}^0;\boldsymbol{h}\right)+\frac{1}{2}D^2R\left(\boldsymbol{e}^0;\boldsymbol{h}\right), \tag{2.42}$$

where $D^2R\left(\boldsymbol{e}^0;\boldsymbol{h}\right)=2\left(\delta\Sigma_d\right)h_\varphi\left(b\right)$. In view of Eq. (2.34), the expressions of the partial sensitivities of $R\left(\boldsymbol{e}\right)$ to the various parameters are:

$$\frac{\partial R}{\partial S}=\frac{\Sigma_d^0}{\Sigma_a^0}\left(1-\frac{\cosh bk}{\cosh ak}\right), \tag{2.43}$$

$$\frac{\partial R}{\partial \Sigma_d}=\frac{S^0}{\Sigma_a^0}\left(1-\frac{\cosh bk}{\cosh ak}\right), \tag{2.44}$$

$$\frac{\partial R}{\partial \Sigma_a}=-\frac{S^0\Sigma_d^0}{\left(\Sigma_a^0\right)^2}\left(1-\frac{\cosh bk}{\cosh ak}\right)+\frac{1}{2\sqrt{D^0\Sigma_a^0}}\frac{S^0\Sigma_d^0}{\Sigma_a^0}\frac{a\sinh ak\cosh bk-b\sinh bk\cosh ak}{\left(\cosh ak\right)^2}, \tag{2.45}$$

$$\frac{\partial R}{\partial D}=-\frac{1}{2}\sqrt{\frac{\Sigma_a^0}{D^0}}\frac{S^0\Sigma_d^0}{D^0\Sigma_a^0}\frac{a\sinh ak\cosh bk-b\sinh bk\cosh ak}{\left(\cosh ak\right)^2}. \tag{2.46}$$

Note that the relative sensitivities of R to Σ_d and S are unity, i.e., $\left(\partial R/\partial\Sigma_d\right)\left(\Sigma_d^0/R\right)=1$ and $\left(\partial R/\partial S\right)\left(S^0/R\right)=1$. The expressions in Eqs. (2.43) through (2.46) will be used in conjunction with Eqs. (1.66), (1.75), (1.77), (1.79), (1.81), (1.82), and (1.83) to assimilate experimental information, perform data adjustment (model calibration), and compute the best estimate values for parameter, responses, and their associated uncertainties.

To illustrate with numerical values the application of these formulas, consider that the slab of extrapolated thickness a consists of water with material properties having the following nominal values: $\Sigma_a^0=0.0197\,cm^{-1}$, $D^0=0{,}16\,cm$, containing distributed neutron sources emitting nominally $S^0=10^7\,neutrons\cdot cm^{-3}\cdot s^{-1}$. For the sake of argument, consider that all of these parameters are uncorrelated and the following relative standard deviations: $\Delta\Sigma_a^0/\Sigma_a^0=5\%$, $\Delta D^0/D^0=5\%$, $\Delta S^0/S^0=15\%$.

Furthermore, consider that measurements are performed with an infinitely thin detector immersed at different locations, $x = b$, in the water slab, having an indium-like nominal detector cross section $\Sigma_d^0 = 7.438\,cm^{-1}$, uncorrelated to the other parameters, with a standard deviation $\Delta\Sigma_d^0 / \Sigma_d^0 = 10\%$. Collecting this information (and omitting, for simplicity, the respective units), it follows that the covariance matrix for the model parameters is

$$\boldsymbol{C}_\alpha = \begin{pmatrix} \left(9.85\times10^{-5}\right)^2 & 0 & 0 & 0 \\ 0 & \left(8.0\times10^{-3}\right)^2 & 0 & 0 \\ 0 & 0 & \left(1.5\times10^{6}\right)^2 & 0 \\ 0 & 0 & 0 & \left(7.44\times10^{-1}\right)^2 \end{pmatrix}. \tag{2.47}$$

2.1.2 An Imprecise but Consistent Measurement

Consider now that a measurement is performed at $b = 10\,cm$ in the positive direction (i.e., to the right of the origin $x = 0$), yielding $r_m = 3.40\times10^9\,neutrons\cdot cm^{-3}\cdot s^{-1}$, with a relative standard deviation of 25%, i.e., $\Delta r_m / r_m = 8.50\times10^8\,neutrons\cdot cm^{-3}\cdot s^{-1}$, which corresponds to a variance $C_m = 7.22\times10^{17}\left(neutrons\cdot cm^{-3}\cdot s^{-1}\right)^2$. On the other hand, using Eq. (2.07), the nominal value of the computed response at $b = 10\,cm$ is obtained as $R(10\,cm) = 3.77\times10^9\,neutrons\cdot cm^{-3}\cdot s^{-1}$. The absolute sensitivities of the response to are: $\partial R(10\,cm)/\partial\Sigma_a = -1.92\times10^{11}$, $\partial R(10\,cm)/\partial D = -1.33\times10^{5}$, $\partial R(10\,cm)/\partial S = 3.77\times10^{2}$, $\partial R(10\,cm)/\partial\Sigma_d = 5.08\times10^{8}$.

The relative sensitivities of $R(10\,cm)$ to Σ_a and D are:

$$\left[\partial R(10\,cm)/\partial\Sigma_a\right]\left[\Sigma_a^0/R(10\,cm)\right] = -.99999,$$

$$\left[\partial R(10\,cm)/\partial D\right]\left[D^0/R(10\,cm)\right] = -5.64\times10^{-6}.$$

Using the above sensitivities in Eq. (1.66) together with the covariance matrix shown in Eq. (1.99) yields the following value for the computed variance of $R(10cm)$:

$$C_{rc}(10cm) = \left[\boldsymbol{S}(10cm)\right]\boldsymbol{C}_{\alpha}\left[\boldsymbol{S}(10cm)\right]^{\dagger} = 4.98\times10^{17}\left(n\cdot cm^{-3}\cdot s^{-1}\right)^{2}, \qquad (2.48)$$

which corresponds to a computed relative standard deviation $\Delta C_{rc}/R(10cm) = 18.72\%$, due to parameter sensitivities and uncertainties. Note that this standard deviation is smaller than would be naively expected from the popular recipe of "taking the square root of the sum of the squared errors", which would in this case amount to 19.37%. The smaller actual computed standard deviation is due to the fact that the sensitivity of $R(10cm)$ to D is vanishingly small, so that the error in D does not contribute to the computed error in $R(10cm)$.

Applying now Eqs. (1.75), (1.79), (1.81), (1.82), and (1.83) to the above information leads to the following best estimate values and covariances:

$$\Sigma_a^{be} = 0.0197\,cm^{-1},\ D^{be} = 0{,}16\ cm,\ S^{be} = 9.7372\times10^{6}\,neutrons\cdot cm^{-3}\cdot s^{-1},\ \Sigma_d^{be} = 7.351\,cm^{-1} \qquad (2.49)$$

$$C_{\alpha}^{be} = \begin{pmatrix} 9.71\times10^{-4} & 0 & 0 & 0 \\ 0 & 0.80\times10^{-2} & 0 & 0 \\ 0 & 0 & 1.28\times10^{6} & 0 \\ 0 & 0 & 0 & 6.99\times10^{-1} \end{pmatrix}$$
$$\times\begin{pmatrix} 1.0 & -1.67\times10^{-7} & 1.03\times10^{-1} & 0.63\times10^{-1} \\ -1.67\times10^{-7} & 1.0 & 5.75\times10^{-7} & 3.50\times10^{-7} \\ 1.03\times10^{-1} & 5.75\times10^{-7} & 1.0 & -2.17\times10^{-1} \\ 0.63\times10^{-1} & 3.50\times10^{-7} & -2.17\times10^{-1} & 1.0 \end{pmatrix} \qquad (2.50)$$
$$\times\begin{pmatrix} 9.71\times10^{-4} & 0 & 0 & 0 \\ 0 & 0.80\times10^{-2} & 0 & 0 \\ 0 & 0 & 1.28\times10^{6} & 0 \\ 0 & 0 & 0 & 6.99\times10^{-1} \end{pmatrix},$$

$$r^{be} = 3.62 \times 10^{9} n \cdot cm^{-3} \cdot s^{-1},\; C_r^{be} = 2.95 \times 10^{17} \left(n \cdot cm^{-3} \cdot s^{-1}\right)^2, \tag{2.51}$$

$$\Delta C_r^{be} = 5.43 \times 10^{8} neutrons \cdot cm^{-3} \cdot s^{-1},\; \Delta C_r^{be} / r^{be} = 14.99\%, \tag{2.52}$$

$$\begin{aligned} C_{\alpha R}^{be} = {} & \left(5.43 \times 10^{8}\right) \times \left(\text{-}2.08 \times 10^{\text{-}1} \quad \text{-}1.15 \times 10^{\text{-}6} \quad 7.18 \times 10^{\text{-}1} \quad 4.37 \times 10^{\text{-}1}\right) \\ & \times \begin{pmatrix} 9.71 \times 10^{\text{-}4} & 0 & 0 & 0 \\ 0 & 0.80 \times 10^{\text{-}2} & 0 & 0 \\ 0 & 0 & 1.28 \times 10^{6} & 0 \\ 0 & 0 & 0 & 6.99 \times 10^{\text{-}1} \end{pmatrix}. \end{aligned} \tag{2.53}$$

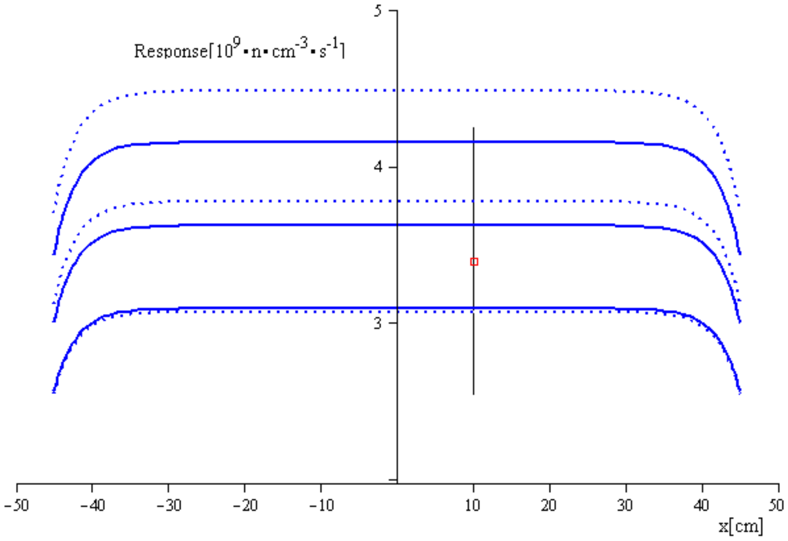

Figure 2.01: An imprecise (relative standard deviation = 25%) but consistent measurement ($\chi^2 = 0.1168$)

Figure 2.01 shows the spatial variation of the original nominal computed values and standard deviations (depicted using broken lines) together with the best estimate values and corresponding standard deviations (depicted using solid lines). The value of the consistency indicator is $\chi^2 = 0.12$, which is reasonable for a single measurement. Altogether, the above information leads to the following conclusions:

(i) As would be expected intuitively, the best-estimate response value, r^{be}, is predicted by the data assimilation and model calibration formalism to fall between the experimentally measured and the originally computed values, somewhat closer to the computed values, because the relative standard deviation of the computed response, $\Delta C_{rc} / R(10\,cm) = 18.72\%$, is smaller than the relative standard deviation of the measured response (25%), i.e.,

$$r_m\left(=3.40\right) < r^{be}\left(=3.62\right) < R\left(10\,cm\right)\left(=3.77\right)\left[\times 10^9\, n \cdot cm^{-3} \cdot s^{-1}\right] \tag{2.54}$$

(ii) Again as expected, the assimilation of a consistent experiment reduces the best-estimate variance, C_r^{be}, of r^{be} to a value that is smaller than the variances of both the computed and measured responses, i.e.,

$$C_r^{be}\left(=2.95\times 10^{17}\right) < C_{rc}\left(=4.99\times 10^{17}\right) < C_m\left(=7.22\times 10^{17}\right) \tag{2.55}$$

(iii). In the case under consideration, the absolute values of the relative sensitivities to S, Σ_d and Σ_a were all equal to unity. In such a case, the adjustment procedure usually affects most the parameters with the largest standard deviation, while those with the smallest original standard deviation are adjusted the least. The above results underscore this general trend, in that the best estimate value of the source S (characterized by the largest original uncertainty) was adjusted the most, followed by the best-estimate value for Σ_d (the second largest original uncertainty), and Σ_a (which had the smallest original uncertainty). Since the relative sensitivity to D was vanishingly small, this parameter was not adjusted following the assimilation of the experiment.

(iv) Comparing the matrices in Eqs. (2.47) and (2.50) indicates that the best-estimate standard deviations for the parameters are also reduced by comparison to their original values. Due to the same reasons as discussed above (i.e., equal absolute values for the relative sensitivities of S, Σ_d, and Σ_a), and the values of the respective original standard deviations, the best-estimate standard deviations for S and Σ_d are the most reduced, the standard deviation for Σ_a is reduced the least, while that for D is not reduced.

(v) Although the parameters were originally considered as uncorrelated, cf. Eq. (2.47), the assimilation of the experimental response induces correlations among the best-estimate parameters, as indicated by the correlation matrix in Eq. (2.50), as follows:

(a) Σ_a^{be} becomes positively correlated with both S^{be} and Σ_d^{be};

(b) S^{be} and Σ_d^{be} become anti-correlated; and

(c) D^{be} remains uncorrelated to the other best-estimate parameters, due to its vanishingly small relative sensitivity.

(vi) As indicated by the correlation matrix $C_{\alpha R}^{be}$ in Eq. (2.53), the best-estimate response becomes anti-correlated to Σ_a^{be}, remains uncorrelated to D^{be}, and becomes positively correlated to both S^{be} and Σ_d^{be}, even though originally the response was considered to have been uncorrelated to any of the original model parameters.

(vi) Due to its vanishingly small relative sensitivity, the diffusion parameter is the sole quantity that has remained essentially unaffected by the assimilation of the experiment and subsequent calibration procedure, i.e., $D^0 = D^{be}$ and $\Delta D^0 / D^0 = \Delta D^{be} / D^{be} = 5\%$.

2.1.3 A Precise and Consistent Measurement

Consider now that the measurement described in the previous section, i.e., $r_m = 3.40 \times 10^9 neutrons \cdot cm^{-3} \cdot s^{-1}$, is performed more precisely, with a relative standard deviation $\Delta r_m / r_m = 5\%$ (rather than 25%), with a corresponding variance $C_m = 2.89 \times 10^{16} \left(neutrons \cdot cm^{-3} \cdot s^{-1} \right)^2$ .In this case, therefore, the experimental variance is considerably smaller than the computed response variance $C_{rc}\left(\boldsymbol{\alpha}^0 \right) = 4.98 \times 10^{17} \left(neutrons \cdot cm^{-3} \cdot s^{-1} \right)^2$.

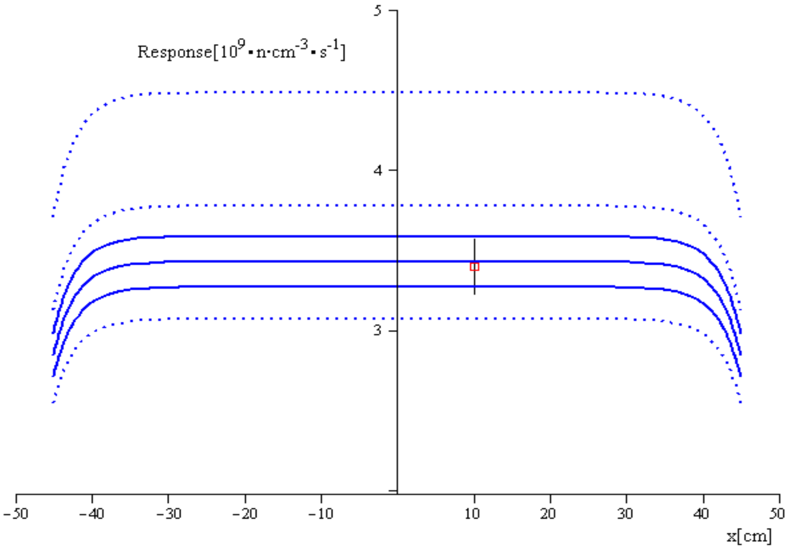

Figure 2.02: A precise (relative standard deviation = 5%) and consistent measurement ($\chi^2 = 0.27$)

Figure 2.02 shows the spatial variation of the original nominal computed values and standard deviations (depicted using broken lines) together with the best estimate response values and corresponding standard deviations (depicted using solid lines). The value of the consistency indicator is $\chi^2 = 0.27$, which is considerably better than for the imprecise measurement considered in the previous section. After assimilating the experiment, the best-estimate values produced by the calibration procedure are:

$$\Sigma_a^{be} = 0.0198\, cm^{-1},\ D^{be} = 0{,}16\ cm,\ S^{be} = 9.393 \times 10^6 neutrons \cdot cm^{-3} \cdot s^{-1}, \Sigma_d^{be} = 7.2371\ cm^{-1}, \tag{2.56}$$

$$C_{\alpha}^{be} = \begin{pmatrix} 9.51\times 10^{-4} & 0 & 0 & 0 \\ 0 & 0.80\times 10^{-2} & 0 & 0 \\ 0 & 0 & 9.39\times 10^{5} & 0 \\ 0 & 0 & 0 & 6.35\times 10^{-1} \end{pmatrix}$$

$$\times \begin{pmatrix} 1.0 & -3.94\times 10^{-7} & 3.34\times 10^{-1} & 1.63\times 10^{-1} \\ -3.94\times 10^{-7} & 1.0 & 1.82\times 10^{-6} & 8.91\times 10^{-7} \\ 3.34\times 10^{-1} & 1.82\times 10^{-6} & 1.0 & -7.57\times 10^{-1} \\ 1.63\times 10^{-1} & 8.91\times 10^{-7} & -7.57\times 10^{-1} & 1.0 \end{pmatrix} \tag{2.57}$$

$$\times \begin{pmatrix} 9.51\times 10^{-4} & 0 & 0 & 0 \\ 0 & 0.80\times 10^{-2} & 0 & 0 \\ 0 & 0 & 9.39\times 10^{5} & 0 \\ 0 & 0 & 0 & 6.35\times 10^{-1} \end{pmatrix},$$

The adjusted best-estimate response value, the corresponding best-estimate response variance, and the best-estimate response-parameter correlation matrix are obtained, respectively, as

$$r^{be} = 3.42\times 10^{9} n\cdot cm^{-3}\cdot s^{-1},\ C_{r}^{be} = 2.73\times 10^{16}\left(n\cdot cm^{-3}\cdot s^{-1}\right)^{2} \tag{2.58}$$

$$C_{\alpha R}^{be} = \left(1.65\times 10^{8}\right)$$

$$\times\left(-6.47\times 10^{-2}\quad -3.52\times 10^{-7}\quad 2.99\times 10^{-1}\quad 1.46\times 10^{-1}\right) \tag{2.59}$$

$$\times \begin{pmatrix} 9.51\times 10^{-4} & 0 & 0 & 0 \\ 0 & 0.80\times 10^{-2} & 0 & 0 \\ 0 & 0 & 9.39\times 10^{5} & 0 \\ 0 & 0 & 0 & 6.35\times 10^{-1} \end{pmatrix}.$$

The following conclusions can be drawn from the above information:

(i) The more precise measurement considered in this section has a considerably stronger influence on the best-estimate adjusted values than the less precise one considered in the previous section, pulling the adjusted values strongly towards the experimentally measured value, as depicted in Figure 2.02. Thus, the best-estimate response value $r^{be} = 3.42\times 10^{9} neutrons\cdot cm^{-3}\cdot s^{-1}$ is much closer to the experimentally measured value than to the originally computed value.

$$r_m\left(=3.40\right) < r^{be}\left(=3.42\right) < R\left(\boldsymbol{\alpha}^0\right)\left(=3.77\right)\left[\times 10^9\, n \cdot cm^{-3} \cdot s^{-1}\right] \tag{2.60}$$

(ii) The best-estimate response variance C_r^{be} is also reduced more significantly in this case than in the case of the less precise measurement considered in the previous section; the best-estimate relative standard deviation is 4.83%. As before, the adjusted best-estimate response variance is smaller than both the measured and the computed response variances, namely.

$$C_r^{be}\left(=2.73\times 10^{16}\right) < C_m\left(=2.89\times 10^{16}\right) < C_{rc}\left(=4.98\times 10^{17}\right) \tag{2.61}$$

(iii) Since the sensitivities have remained unchanged, the largest adjustments occurred for the source S (characterized by the largest original uncertainty), followed by Σ_d (the second largest original uncertainty); Σ_a underwent a minute adjustment, while D was not adjusted (just as in the previous section). However, since the experimental response variance is much smaller than in the previous section, the corresponding parameter-adjustments are also larger than in the previous section.

(iv) Comparing the best-estimate parameter covariance matrix C_α^{be} in Eq. (2.57) with the original parameter covariance matrix in Eq. (2.47) shows that the best-estimate standard deviations for the parameters are reduced more by the more precise experiment considered in this case (by comparison to the uncertainty reductions effected in the previous section). The largest reductions of the standard deviations occurred, in order, for S (best-estimate relative standard deviation reduced to 10%), Σ_d (best-estimate relative standard deviation reduced to 8.78%), and Σ_a (best-estimate relative standard deviation reduced to 4.79%), while that for D was hardly reduced (4.99%).

(v) Just as in the previous section, the originally uncorrelated parameters became correlated after calibration, as indicated by the correlation matrix C_α^{be} in Eq. (2.57). The nature of the induced correlations has retained the same character as in the previous section (i.e., Σ_a^{be} has become positively correlated with both S^{be} and Σ_d^{be}; S^{be} and Σ_d^{be} have become anti-correlated; and D^{be} remained uncorrelated to the other best-estimate parameters), but the induced best-estimate correlations have become stronger (i.e., larger in absolute values) than in the previous case, by a factor of about three.

(vi) Just as in the previous section, the best-estimate response has become anti-correlated to Σ_a^{be}, remained uncorrelated to D^{be}, and became positively correlated to both S^{be} and Σ_d^{be}. However, as indicated by the correlation matrix $C_{\alpha R}^{be}$ in Eq. (2.59), these correlations have become weaker (i.e., have become larger in absolute values), also by a factor of about three, by comparison to the previous case.

(vi) As before, because of its vanishingly small relative sensitivity, the diffusion parameter has remained essentially unaffected by the assimilation of the experiment and subsequent calibration procedure.

2.1.4 Four Precise and Consistent Measurements

To illustrate the effects of several consistent measurements, and also to test that symmetric measurements (with respect to the vertical plane through the origin) do preserve the solution's symmetry, we consider four consistent ($\chi^2 = 1.21$) measurements, taken at the symmetric locations $-10\,cm, -40\,cm,\ 10\,cm, 40\,cm$, and having the following values and relative standard deviations (abbreviated as "rsd"):

$$r_1^m \triangleq r\left(meas.at\ \ 10\,cm\right) = 3.40\times10^9 n\cdot cm^{-3}\cdot sec^{-1};\ rsd\left(r_1^m\right) = 5\%; \tag{2.62}$$

$$r_2^m \triangleq r\left(meas.at\ \ -10\,cm\right) = 3.59\times10^9 n\cdot cm^{-3}\cdot sec^{-1};\ rsd\left(r_2^m\right) = 6\%; \tag{2.63}$$

$$r_3^m \triangleq r\left(meas.at\ \ -40\,cm\right) = 3.77\times10^9 n\cdot cm^{-3}\cdot sec^{-1};\ rsd\left(r_3^m\right) = 5\%; \tag{2.64}$$

$$r_4^m \triangleq r\left(meas.at\ \ 40\,cm\right) = 3.74\times10^9 n\cdot cm^{-3}\cdot sec^{-1};\ rsd\left(r_4^m\right) = 5\%; \tag{2.65}$$

Thus, the covariance matrix of the measured responses is

$$\boldsymbol{C}_m = \begin{pmatrix} \left(1.7\times10^8\right)^2 & 0 & 0 & 0 \\ 0 & \left(2.15\times10^8\right)^2 & 0 & 0 \\ 0 & 0 & \left(1.89\times10^8\right)^2 & 0 \\ 0 & 0 & 0 & \left(1.87\times10^8\right)^2 \end{pmatrix} \tag{2.66}$$

The nominal values of the computed responses at the above locations are as follows:

$$R_1\left(comp.\ at\ \ 10\,cm\right) = 3.77\times10^9 n\cdot cm^{-3}\cdot sec^{-1}; \tag{2.67}$$

$$R_2\left(comp.\ at\ -10\,cm\right) = 3.77\times10^9 n\cdot cm^{-3}\cdot sec^{-1}; \tag{2.68}$$

$$R_3\left(comp.\ at\ -40\,cm\right) = 3.66\times10^9 n\cdot cm^{-3}\cdot sec^{-1}; \tag{2.69}$$

$$R_4\left(comp.\ at\ \ 40\,cm\right) = 3.66\times10^9 n\cdot cm^{-3}\cdot sec^{-1}; \tag{2.70}$$

As expected, the above computed responses confirm the problem's symmetry. The matrices S and S_{rel}, with $\Delta\alpha_j \triangleq std.\,dev.\left(\alpha_j\right)$, containing the nominal values of the absolute and relative sensitivities, respectively, are:

$$\boldsymbol{S} \triangleq \left(\frac{\partial R_i}{\partial \alpha_j}\right) = \begin{pmatrix} -1.92\times10^{11} & -1.33\times10^{5} & 3.78\times10^{2} & 5.08\times10^{8} \\ -1.92\times10^{11} & -1.33\times10^{5} & 3.78\times10^{2} & 5.08\times10^{8} \\ -1.76\times10^{11} & -1.24\times10^{9} & 3.66\times10^{2} & 4.92\times10^{8} \\ -1.76\times10^{11} & -1.24\times10^{9} & 3.66\times10^{2} & 4.92\times10^{8} \end{pmatrix}, \tag{2.71}$$

$$\boldsymbol{S}_{rel} \triangleq \left(\frac{\partial R_i}{\partial \alpha_j}\frac{\Delta\alpha_j}{R_i}\right) = \begin{pmatrix} -0.99999 & -5.64\times10^{-6} & 1.00 & 1.00 \\ -0.99999 & -5.64\times10^{-6} & 1.00 & 1.00 \\ -9.46\times10^{-1} & -5.41\times10^{-2} & 1.00 & 1.00 \\ -9.46\times10^{-1} & -5.41\times10^{-2} & 1.00 & 1.00 \end{pmatrix}. \tag{2.72}$$

As already noted, the relative sensitivities of each of the four responses are unity for S and Σ_d. Furthermore, the relative sensitivities of R_2 and R_2 to Σ_a are practically unity (in the region where the response is essentially constant in space), while those of R_3 and R_4 to Σ_a are just about 5% smaller, in the regions closer to the slab's boundary. Finally, the relative sensitivities of R_2 and R_2 to D are practically nil (in the region where the response is essentially constant in space), while those of R_3 and R_4 to D considerably larger, but still very small (ca. 5%) by comparison to the other relative sensitivities. Using the above sensitivities in Eq. (1.66) together with the covariance matrix shown in Eq. (2.58) yields the following value for the covariance matrix of the computed responses:

$$\begin{aligned} \boldsymbol{C}_{rc} &= \boldsymbol{S}\boldsymbol{C}_{\alpha}\boldsymbol{S}^{\dagger} \\ &= \begin{pmatrix} 7.06\times10^{8} & 0 & 0 & 0 \\ 0 & 7.06\times10^{8} & 0 & 0 \\ 0 & 0 & 6.83\times10^{8} & 0 \\ 0 & 0 & 0 & 6.83\times10^{8} \end{pmatrix} \\ &\times \begin{pmatrix} 1.0 & 0.9999 & 0.9998 & 0.9998 \\ 0.9999 & 1.0 & 0.9998 & 0.9998 \\ 0.9998 & 0.9998 & 1.0 & 1.00 \\ 0.9998 & 0.9998 & 1.00 & 1.0 \end{pmatrix} \\ &\times \begin{pmatrix} 7.06\times10^{8} & 0 & 0 & 0 \\ 0 & 7.06\times10^{8} & 0 & 0 \\ 0 & 0 & 6.83\times10^{8} & 0 \\ 0 & 0 & 0 & 6.83\times10^{8} \end{pmatrix}. \end{aligned} \tag{2.73}$$

From the above covariance matrix and from Eqs. (2.67) through (2.70), the relative standard deviations of the four computed responses are $rsd(R_3) = rsd(R_4) = 18.64\%$ and , respectively. Note that the particular values (essentially either unity or zero) of the components of the sensitivity matrix lead to a fully correlated covariance matrix for the four computed responses.

Applying the data assimilation and adjustment procedure, cf. Eqs. (1.75), (1.79), (1.81), (1.82), and (1.83), to the above information leads to the following best estimate parameter values, relative standard deviations (abbreviated as "rsd"), and covariances:

$$\Sigma_a^{be} = 0.0198\,cm^{-1},\ rsd\left(\Sigma_a^{be}\right) = 4.79\%; \tag{2.74}$$

$$D^{be} = 0{,}1591\ cm,\ rsd\left(D^{be}\right) = 5.00\%; \tag{2.75}$$

$$S^{be} = 9.85\times10^{6}\,n\cdot cm^{-3}\cdot s^{-1},\ rsd\left(S^{be}\right) = 9.21\%; \tag{2.76}$$

$$\Sigma_d^{be} = 7.388\,cm^{-1},\ \ rsd\left(\Sigma_d^{be}\right) = 8.53\%; \tag{2.77}$$

$$\begin{aligned}\boldsymbol{C}_{\alpha}^{be} = &\begin{pmatrix} 9.50\times10^{-4} & 0 & 0 & 0 \\ 0 & 7.99\times10^{-3} & 0 & 0 \\ 0 & 0 & 9.08\times10^{5} & 0 \\ 0 & 0 & 0 & 6.30\times10^{-1} \end{pmatrix} \\ \times &\begin{pmatrix} 1.0 & -8.89\times10^{-4} & 3.51\times10^{-1} & 1.67\times10^{-1} \\ -8.89\times10^{-4} & 1.0 & 1.02\times10^{-2} & 4.84\times10^{-3} \\ 3.51\times10^{-1} & 1.02\times10^{-2} & 1.0 & -8.24\times10^{-1} \\ 1.67\times10^{-1} & 4.84\times10^{-3} & -8.24\times10^{-1} & 1.0 \end{pmatrix} \\ \times &\begin{pmatrix} 9.50\times10^{-4} & 0 & 0 & 0 \\ 0 & 7.99\times10^{-3} & 0 & 0 \\ 0 & 0 & 9.08\times10^{5} & 0 \\ 0 & 0 & 0 & 6.30\times10^{-1} \end{pmatrix},\end{aligned} \tag{2.78}$$

$$at\ \left(10\,cm\right):\ r_1^{be} = 3.66\times10^{9}\,n\cdot cm^{-3}\cdot sec^{-1};\ rsd\left(r_1^{be}\right) = 2.58\%; \tag{2.79}$$

$$at\ \left(-10\,cm\right):\ r_2^{be} = 3.66\times10^{9}\,n\cdot cm^{-3}\cdot sec^{-1};\ rsd\left(r_2^{be}\right) = 2.59\%; \tag{2.80}$$

$$at\ \left(-40\,cm\right):\ r_3^{be} = 3.56\times10^{9}\,n\cdot cm^{-3}\cdot sec^{-1};\ rsd\left(r_3^{be}\right) = 2.59\%; \tag{2.81}$$

$$at\ \left(40\,cm\right):\ r_4^{be} = 3.56\times10^{9}\,n\cdot cm^{-3}\cdot sec^{-1};\ rsd\left(r_4^{be}\right) = 2.58\%; \tag{2.82}$$

$$\boldsymbol{C}_{r}^{be}=\begin{pmatrix} 9.51\times10^{7} & 0 & 0 & 0\\ 0 & 9.51\times10^{7} & 0 & 0\\ 0 & 0 & 9.19\times10^{7} & 0\\ 0 & 0 & 0 & 9.19\times10^{7}\end{pmatrix}\times\begin{pmatrix} 1.00 & 1.00 & 0.988 & 0.988\\ 1.00 & 1.00 & 0.988 & 0.988\\ 0.988 & 0.988 & 1.00 & 0.999\\ 0.988 & 0.988 & 0.999 & 1.00\end{pmatrix}\times\begin{pmatrix} 9.51\times10^{7} & 0 & 0 & 0\\ 0 & 9.51\times10^{7} & 0 & 0\\ 0 & 0 & 9.19\times10^{7} & 0\\ 0 & 0 & 0 & 9.19\times10^{7}\end{pmatrix}, \tag{2.83}$$

$$\boldsymbol{C}_{\alpha r}^{be}=\begin{pmatrix} 9.51\times10^{7} & 0 & 0 & 0\\ 0 & 9.51\times10^{7} & 0 & 0\\ 0 & 0 & 9.19\times10^{7} & 0\\ 0 & 0 & 0 & 9.19\times10^{7}\end{pmatrix}\times\begin{pmatrix} -8.65\times10^{-2} & 5.12\times10^{-2} & 1.60\times10^{-1} & 7.62\times10^{-2}\\ -8.65\times10^{-2} & 5.12\times10^{-2} & 1.60\times10^{-1} & 7.62\times10^{-2}\\ 1.72\times10^{-2} & -5.62\times10^{-2} & 1.96\times10^{-1} & 9.34\times10^{-2}\\ 1.72\times10^{-2} & -5.62\times10^{-2} & 1.96\times10^{-1} & 9.34\times10^{-2}\end{pmatrix}\times\begin{pmatrix} 9.50\times10^{-4} & 0 & 0 & 0\\ 0 & 7.99\times10^{-3} & 0 & 0\\ 0 & 0 & 9.08\times10^{5} & 0\\ 0 & 0 & 0 & 6.30\times10^{-1}\end{pmatrix}. \tag{2.84}$$

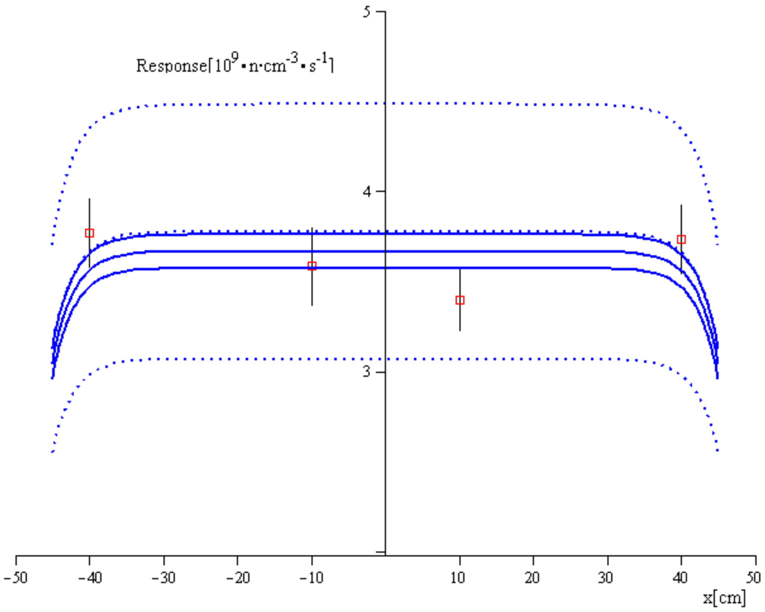

Figure 2.03 Four precise consistent precise measurements ($\chi^2 = 1.21$)

Figure 2.03 shows the spatial variation of the original nominal computed values and standard deviations (depicted using broken lines) together with the best estimate response values and corresponding standard deviations (depicted using solid lines). The value of $\chi^2 = 1.21$ indicates a very good consistency among the four measurements. Altogether, the above information leads to the following conclusions:

(i) The adjustment procedure preserves the problem’s symmetry, as reflected in all of the values in Eqs.(2.73) through (2.84). In order to preserve this symmetry, the adjustment procedure forces the best-estimate response values $r_2^{be} = r_3^{be}$ to fall below both the experimentally measured and the originally computed values. However, the values of $r_2^{be} = r_3^{be}$ remain nevertheless consistent with the other best-estimate response values, since they remain within their “one-standard deviation” respective ranges.

(ii) As expected, the assimilation of a consistent experiment reduces the best-estimate variances values that are smaller than the variances of both the computed and measured responses, i.e.,

$$rsd\left(r_i^{be}\right) < rsd\left(r_i^{m}\right) < rsd\left(R_i\right); \; i = 1,\ldots,4; \qquad (2.85)$$

(iii). As in the previous sections, the absolute values of the relative sensitivities to S and Σ_d were unity, while that of Σ_a remained nearly equal to unity, and that of D continued to remain vanishingly small. Hence, also as in previous sections the best estimate value of the source S (characterized by the largest original uncertainty) was adjusted the most, followed by the best-estimate value for Σ_d (the second largest original uncertainty), and Σ_a (which had the smallest original uncertainty). In contrast to the case of a single experiment, though , the diffusion coefficient D was adjusted (slightly) following the assimilation of four experiments, due to the fact that the relative sensitivities to D of the responses near the slab's boundaries were small but non-zero.

(iv) As in previous sections, the best-estimate standard deviations for the parameters are also reduced by comparison to their original values. Due to the same reasons as discussed in the previous sections, the best-estimate standard deviations for S and Σ_d are the most reduced, the standard deviation for Σ_a is reduced the least, and that for D is not been reduced.

(v) As in the previous sections, the assimilation of experimental data causes the originally uncorrelated parameters and responses to become correlated, as indicated by the matrices $\boldsymbol{C}_{\alpha}^{be}$, $\boldsymbol{C}_{r}^{be}$ and $\boldsymbol{C}_{\alpha r}^{be}$.

Parameter estimation is an important part of the creation of a complex numerical model. Therefore, the values of the various model parameters must be calibrated (adjusted) to the correct values. Until the recent introduction of adjoint methods in this field, parameters have been estimated by using a large number of trial-and-error direct perturbation sensitivity experiments. For problems involving a large number of unknown parameters, the identifiability problem becomes even more difficult because of correlation between parameters. Hence, models must consider not only optimal parameter values (which adjoint computations now readily generate), but a range of parameter values within the joint distribution of parameter uncertainties, since this joint distribution determines the uncertainties in responses for a given scenario. For these reasons, the problem of parameter estimation has recently attracted a great deal of attention; intense efforts and research resources are devoted to this problem.

Data adjustment (model calibration) for large-scale models will certainly pose significant computational challenges which may require adopting reasonable compromises, such as reduced-order modeling, to avoid difficulties arising from increased dimensionality. Methods of large-scale constrained minimization for the solution of optimal parameter estimation for range-bounded parameters may need to employ sequential quadratic programming and projected gradient minimization methods.

3 Time-Dependent Data Assimilation and Model Calibration

3.1 Paradigm Example: A Radioactive Decay Chain

Consider the time-dependent decay of a radioactive substance, $N_1(t)$, from an initial quantity $N_1(0) = N_{10}$ at time $t = 0$, which decay with a decay constant λ_1 into a daughter substance, $N_2(t)$. The daughter substance is itself radioactive and decays, in turn, with a decay constant λ_2 into a grand-daughter substance, $N_3(t)$, which is also radioactive, and decays, in turn, with a decay constant λ_3. This three-member radioactive decay chain can be written in matrix form as:

$$\begin{pmatrix} \frac{d}{dt}+\lambda_1 & 0 & 0 \\ -\lambda_1 & \frac{d}{dt}+\lambda_2 & 0 \\ 0 & -\lambda_2 & \frac{d}{dt}+\lambda_3 \end{pmatrix} \begin{pmatrix} N_1(t) \\ N_2(t) \\ N_3(t) \end{pmatrix} = \begin{pmatrix} 0 \\ 0 \\ 0 \end{pmatrix} \tag{3.01}$$

subject to the initial conditions:

$$N_1(0) = N_{10},\ N_2(0) = 0,\ N_3(0) = 0, \text{ at } t = 0. \tag{3.02}$$

The decay constants $\lambda_i, i = 1,2,3$ and the initial quantity N_{10} are considered to have been obtained experimentally and are therefore affected by uncertainties. The information usually available in practice are nominal (mean) values and standard deviations. In this particular case, therefore, the nominal values, denoted as N_{10}^0 and $\lambda_i^0, i = 1,2,3$, are considered to be known along with the respective standard deviation, denoted here as δN_{10} and $\delta\lambda_i, i = 1,2,3$.

For the purposes of model calibration (data adjustment), consider that various experimentally measured values of the so-called *activities* $A_i(t) \equiv \lambda_i N_i(t),\, i = 1,2,3,$ at various instances in time, are also available. Especially for small numbers, they are intrinsically statistical quantities which may or may not be correlated. The paradigm problem considered in this section is to apply the time-dependent methodology presented in Section 1.2, using the "experimentally measured" activities, to obtain best-estimate mean values and reduced uncertainties for the decay constants $\lambda_i,\, i = 1,2,3$ and the initial quantity N_{10}.

The *activities* $A_i(t) \equiv \lambda_i N_i(t),\, i = 1,2,3,$ can be computed after solving Eqs. (3.01) and (3.02) for any (known) nominal values of the model parameters N_{10} and $\lambda_i,\, i = 1,2,3$, to obtain

$$N_1(t) = N_{10} e^{-\lambda_1 t}, \tag{3.03}$$

$$N_2(t) = \frac{N_{10}\lambda_1}{\lambda_2 - \lambda_1}\left(e^{-\lambda_1 t} - e^{-\lambda_2 t}\right), \tag{3.04}$$

$$\begin{aligned} N_3(t) = {} & \frac{\lambda_1 \lambda_2 N_{10} e^{-\lambda_1 t}}{(\lambda_2 - \lambda_1)(\lambda_3 - \lambda_1)} + \frac{\lambda_1 \lambda_2 N_{10} e^{-\lambda_2 t}}{(\lambda_1 - \lambda_2)(\lambda_3 - \lambda_2)} \\ & + \frac{\lambda_1 \lambda_2 N_{10} e^{-\lambda_3 t}}{(\lambda_3 - \lambda_1)(\lambda_3 - \lambda_2)}. \end{aligned} \tag{3.05}$$

The above solutions indicate that the radioactivity of the parent substance, $N_1(t)$, decays ultimately to zero from its initial value $N_1(0) = N_{10}$ at time $t = 0$. The daughter substance, $N_2(t)$, builds up to a maximum value $N_2(t_{2m}) = N_{10} e^{-\lambda_2 t_{2m}}$, which is reached at time $t_{2m} \equiv (\lambda_2 - \lambda_1)^{-1} ln(\lambda_2 / \lambda_1)$, after which it will ultimately decay to zero, too. The grand-daughter substance, $N_3(t)$, also builds up to a maximum value after which it also ultimately decays to zero.

A measured activity at any time instant instances t_i is evidently a "number". From a computational point of view, such a "number" can be represented mathematically as a functional of the state variables $\boldsymbol{u} \equiv \left[N_1(t),\, N_2(t),\, N_3(t) \right]$ and model parameters $\boldsymbol{\alpha} \equiv \left[N_{10},\, \lambda_1,\, \lambda_2,\, \lambda_3 \right]$ of the general form

$$R(\boldsymbol{u},\boldsymbol{\alpha}) \equiv \int_0^{t_f} F(\boldsymbol{u},\boldsymbol{\alpha})\, \delta(t - t_i)\, dt, \tag{3.06}$$

where $F(\boldsymbol{u},\boldsymbol{\alpha})$ is a function of the indicated arguments and $\delta(t - t_i)$ is the customary Dirac delta functional. The sensitivity of the response $R(\boldsymbol{u},\boldsymbol{\alpha})$ defined in Eq. (3.06) to variations $\boldsymbol{h}_\alpha \equiv \left[\delta N_{10},\, \delta\lambda_1,\, \delta\lambda_2,\, \delta\lambda_3 \right]$ in the model parameters and variations $\boldsymbol{h}_u \equiv \left[\delta N_1(t),\, \delta N_2(t),\, \delta N_3(t) \right] \equiv \left[h_1(t),\, h_2(t),\, h_3(t) \right]$ in the state functions is given by the Gateaux-differential $DR(\boldsymbol{u},\boldsymbol{\alpha};\boldsymbol{h}_u,\boldsymbol{h}_\alpha)$ of $R(\boldsymbol{u},\boldsymbol{\alpha})$ at the nominal parameter values $\boldsymbol{\alpha}^0 \equiv \left[N_{10}^0,\, \lambda_1^0,\, \lambda_2^0,\, \lambda_3^0 \right]$ and the corresponding the nominal values of the state variables as $\boldsymbol{u}^0 \equiv \left[N_1^0(t),\, N_2^0(t),\, N_3^0(t) \right]$, and is defined as

$$DR(\boldsymbol{u},\boldsymbol{\alpha};\boldsymbol{h}_u,\boldsymbol{h}_\alpha) \equiv \left\{ \frac{d}{d\varepsilon} R\left[\boldsymbol{u}^0 + \varepsilon \boldsymbol{h}_u,\, \boldsymbol{\alpha}^0 + \varepsilon\, \boldsymbol{h}_\alpha \right] \right\}_{\varepsilon = 0} . \tag{3.07}$$

Applying the above definition to Eq. (3.06) gives

$$DR(\boldsymbol{u},\boldsymbol{\alpha};\boldsymbol{h}_u,\boldsymbol{h}_\alpha) = (DR)_{dir} + (DR)_{in}, \tag{3.08}$$

where the direct effect term $(DR)_{dir}$ is defined as

$$(DR)_{dir} \equiv \int_0^{t_f} F'_\alpha(\boldsymbol{u}^0,\boldsymbol{\alpha}^0)\, \boldsymbol{h}_\alpha\, \delta(t - t_i)\, dt, \tag{3.09}$$

while the indirect effect term $(DR)_{in}$ is defined as

$$(DR)_{in} \equiv \int_0^{t_f} F'_u(\boldsymbol{u}^0,\boldsymbol{\alpha}^0)\, \boldsymbol{h}_u\, \delta(t - t_i)\, dt. \tag{3.10}$$

The forward sensitivity system (variational tangent model) [Cacuci, 2003] of the radioactive chain model is needed in order to determine the variational vector $\boldsymbol{h}_u$. This system is obtained by taking the Gateaux-derivative of Eqs. (3.01) and (3.02), to obtain

$$\boldsymbol{Lh} \equiv \begin{pmatrix} \frac{d}{dt}+\lambda_1 & 0 & 0 \\ -\lambda_1 & \frac{d}{dt}+\lambda_2 & 0 \\ 0 & -\lambda_2 & \frac{d}{dt}+\lambda_3 \end{pmatrix} \begin{pmatrix} h_1(t) \\ h_2(t) \\ h_3(t) \end{pmatrix} = \begin{pmatrix} -\delta\lambda_1 N_1^0(t) \\ -\delta\lambda_2 N_2^0(t)+\delta\lambda_1 N_1^0(t) \\ -\delta\lambda_3 N_3^0(t)+\delta\lambda_2 N_2^0(t) \end{pmatrix} \tag{3.11}$$

subject to the initial conditions

$$h_1(0)=\delta N_{10},\ h_2(0)=0,\ h_3(0)=0, \text{ at } t=0. \tag{3.12}$$

3.1.1 Deterministic Computation of Sensitivities Using the Adjoint Model

The adjoint sensitivity system corresponding to the above forward sensitivity model is obtained by applying the general theory outlined in [Cacuci, 2003]. Fundamentally, the adjoint system is introduced via an appropriately defined inner product. For the present problem, in which the state variables are three-component vectors of the form $\boldsymbol{h}_u \equiv \left[h_1(t), h_2(t), h_3(t)\right]$, the inner product is defined as

$$\langle h_u, \psi \rangle \equiv \int_0^{t_f} \left[\sum_{i=1}^{3} h_i(t)\psi_i(t) \right] dt. \tag{3.13}$$

where $\boldsymbol{\psi} \equiv \left[\psi_1(t), \psi_2(t), \psi_3(t)\right]$. Applying the general theory outlined in [Cacuci, 2003] leads to the following final-value time problem for the vector of adjoint functions $\boldsymbol{\psi} \equiv \left[\psi_1(t), \psi_2(t), \psi_3(t)\right]$:

$$\boldsymbol{L}^{*}\boldsymbol{\psi} \equiv \begin{pmatrix} -\frac{d}{dt}+\lambda_1 & -\lambda_1 & 0 \\ 0 & -\frac{d}{dt}+\lambda_2 & -\lambda_2 \\ 0 & 0 & -\frac{d}{dt}+\lambda_3 \end{pmatrix} \begin{pmatrix} \psi_1(t) \\ \psi_2(t) \\ \psi_3(t) \end{pmatrix} = \begin{pmatrix} \frac{\partial F}{\partial N_1}\delta(t-t_i) \\ \frac{\partial F}{\partial N_2}\delta(t-t_i) \\ \frac{\partial F}{\partial N_3}\delta(t-t_i) \end{pmatrix}, \tag{3.14}$$

subject to the final-time conditions

$$\psi_1(t_f)=0,\ \psi_2(t_f)=0,\ \psi_3(t_f)=0,\ \text{at } t=t_f. \tag{3.15}$$

The indirect effect term can be expressed alternately in terms of adjoint functions as follows:

$$\begin{aligned}(DR)_{in} &\equiv \int_0^{t_f} F_u'(u^0,\alpha^0)h_u\,dt = \langle h_u, L^{*}\psi\rangle = \langle \psi, Lh_u\rangle - \hat{P}(h,\psi;u^0,\alpha^0) \\ &= (\delta N_{10})\psi_1(0) + (\delta\lambda_1)\int_0^{t_f} N_1^0(t)\left[\psi_2(t)-\psi_1(t)\right]dt \\ &\quad +(\delta\lambda_2)\int_0^{t_f} N_2^0(t)\left[\psi_3(t)-\psi_2(t)\right]dt - (\delta\lambda_3)\int_0^{t_f} N_3^0(t)\psi_3(t)\,dt,\end{aligned} \tag{3.16}$$

Note the important fact, generally valid for time-evolution systems, that the sensitivity of the response to the system's initial conditions are related directly to the values of the adjoint functions at the initial-time. Actually, for the particular radioactive decay chain example considered in this section, the sensitivity of the particular responses selected above actually *coincides* with the value of the adjoint function at the initial time $t=0$. This property provides a very valuable tool to verify the accuracy of solving the adjoint sensitivity system backwards in time, from the final-time value to the initial one, to compute the respective adjoint functions.

3.1.1.1 Measurements of $A_1(t) \equiv \lambda_1 N_1(t_i),\, i = 1,\ldots,n_1$.

To begin with, consider that values $A_1(t) \equiv \lambda_1 N_1(t_i),\, i = 1,\ldots,n_1,$ of the time-dependent activity of the radioactive substance $N_1(t)$, are measured at n_1 instances $t_i,\, i = 1,\ldots,n_1$, in time. These *measured responses* may or may not be correlated. From a computational standpoint, the nominal values of these responses can be readily computed at each time point $t_i,\, i = 1,\ldots,n_1$ by using Eq. (3.03) to obtain

$$R_1\left(\boldsymbol{u}^0,\boldsymbol{\alpha}^0\right) = \lambda_1^0 N_1^0(t_i) = \lambda_1^0 N_{10}^0 e^{-\lambda_1 t_i},\; i = 1,\ldots,n_1. \tag{3.17}$$

The above response can be represented mathematically as a functional of the form given in Eq. (3.06), namely

$$R_1(\boldsymbol{u},\boldsymbol{\alpha}) \equiv \int_0^{t_f} \lambda_1 N_1(t)\,\delta(t - t_i)\,dt, \tag{3.18}$$

where t_f denotes the (finite or infinite) final-time value to be considered for this problem.

The sensitivities of the above response to variations $\boldsymbol{h}_u$ and $\boldsymbol{h}_\alpha$ are given by the Gateaux-differential, $DR_1\left(\boldsymbol{u}^0,\boldsymbol{\alpha}^0;\boldsymbol{h}_u,\boldsymbol{h}_\alpha\right)$, of $R_1(\boldsymbol{u},\boldsymbol{\alpha})$, which is obtained as a particular case of Eqs. (3.09) and (3.10), giving the expressions

$$\begin{gathered} DR_1\left(\boldsymbol{u}^0,\boldsymbol{\alpha}^0;\boldsymbol{h}_u,\boldsymbol{h}_\alpha\right) = \left(DR_1\right)_{dir} + \left(DR_1\right)_{in},\ \text{where} \\ \left(DR_1\right)_{dir} \equiv \left(\delta\lambda_1\right) N_1^0(t_i),\;\; \left(DR_1\right)_{in} \equiv \int_0^{t_f} \lambda_1^0 h_1(t)\,\delta(t - t_i)\,dt. \end{gathered} \tag{3.19}$$

The direct effect term, $\left(DR_1\right)_{dir}$, can be evaluated immediately, but the indirect effect term $\left(DR_1\right)_{in}$ needs to be evaluated either by the forward (*FSAP*) or the adjoint (*ASAP*) sensitivity analysis procedure. Even though the number of model parameters (4) is modest in this paradigm problem, the *ASAP* is still more efficient to use than the *FSAP*. For the particular form of $\left(DR_1\right)_{in}$ defined in Eq. (3.19), the adjoint sensitivity system shown in Eq. (3.14) takes on the following particular form:

$$\begin{pmatrix} -\frac{d}{dt}+\lambda_1^0 & -\lambda_1^0 & 0 \\ 0 & -\frac{d}{dt}+\lambda_2^0 & -\lambda_2^0 \\ 0 & 0 & -\frac{d}{dt}+\lambda_3^0 \end{pmatrix} \begin{pmatrix} \psi_1(t) \\ \psi_2(t) \\ \psi_3(t) \end{pmatrix} = \begin{pmatrix} \lambda_1^0 \delta(t-t_i) \\ 0 \\ 0 \end{pmatrix}, \tag{3.20}$$

subject to the same final-time conditions as shown in Eq. (3.15). The solution to the above final-time problem is readily obtained in the form

$$\psi_3(t) \equiv 0,\ \psi_2(t) \equiv 0,\ \psi_1(t) = \lambda_1^0 e^{-\lambda_1^0 (t_i - t)} H(t_i - t), \tag{3.21}$$

where $H(t-t_i)$ denotes the customary Heaviside functional defined as

$$H(t_i - t) \equiv \begin{cases} 0, \text{ if } t_i < t, \\ 1, \text{ if } t_i \geq t. \end{cases} \tag{3.22}$$

Taking into account the expression of the direct effect term from Eq. (3.19), inserting the expressions obtained in Eq. (3.21) into the general form given in Eq. (3.16), and performing the respective integration yields the following expressions for the non-zero sensitivities of $R_2(\boldsymbol{u},\boldsymbol{\alpha})$:

$$\frac{\partial R_1}{\partial N_{10}} = \psi_1(0) = \lambda_1^0 e^{-\lambda_1^0 t_i},\ \frac{\partial R_1}{\partial \lambda_1} = N_{10}^0 \left(1 - \lambda_1^0 t_i\right) e^{-\lambda_1^0 t_i}. \tag{3.23}$$

3.1.1.2 Measurements of $A_2(t) \equiv \lambda_2 N_2(t_j),\ j = 1,\ldots,n_2.$

Consider next that values $A_2(t) \equiv \lambda_2 N_2(t_j),\ j = 1,\ldots,n_2,$ of the time-dependent activity of the radioactive substance $N_2(t)$, are measured at n_2 instances $t_j,\ j = 1,\ldots,n_2$, in time. These *measured responses* may or may not be correlated. The computed nominal values of these responses can be readily computed from Eq. (3.04) to obtain

$$R_2\left(\boldsymbol{u}^0,\boldsymbol{\alpha}^0\right) = \lambda_2^0 N_2^0\left(t_j\right) = \frac{N_{10}^0 \lambda_1^0}{\lambda_2^0 - \lambda_1^0}\left(e^{-\lambda_1^0 t_j} - e^{-\lambda_2^0 t_j}\right),\ j = 1,\ldots,n_2. \tag{3.24}$$

As before, the response $R_2(\boldsymbol{u},\boldsymbol{\alpha})$ can be represented mathematically as a functional of the form

$$R_2(\boldsymbol{u},\boldsymbol{\alpha}) \equiv \int_0^{t_f} \lambda_2 N_2(t)\delta\left(t - t_j\right)dt, \tag{3.25}$$

where t_f denotes the (finite or infinite) final-time value to be considered for this problem.

The sensitivities of the above response to variations $\boldsymbol{h}_u$ and $\boldsymbol{h}_\alpha$ are given by the Gateaux-differential, $DR_2\left(\boldsymbol{u}^0,\boldsymbol{\alpha}^0;\boldsymbol{h}_u,\boldsymbol{h}_\alpha\right)$, of $R_2(\boldsymbol{u},\boldsymbol{\alpha})$, which is obtained as

$$\begin{gathered} DR_2\left(\boldsymbol{u}^0,\boldsymbol{\alpha}^0;\boldsymbol{h}_u,\boldsymbol{h}_\alpha\right) = \left(DR_2\right)_{dir} + \left(DR_2\right)_{in},\ \text{where} \\ \left(DR_2\right)_{dir} \equiv \left(\delta\lambda_2\right) N_2^0\left(t_j\right),\ \ \left(DR_2\right)_{in} \equiv \int_0^{t_f} \lambda_2^0 h_2(t)\delta\left(t - t_j\right)dt. \end{gathered} \tag{3.26}$$

The direct effect term, $\left(DR_2\right)_{dir}$, can be evaluated immediately, but the indirect effect term $\left(DR_2\right)_{in}$ needs to be evaluated either by the forward (*FSAP*) or the adjoint (*ASAP*) sensitivity analysis procedure. For the particular form of $\left(DR_2\right)_{in}$ defined in Eq. (3.26), the adjoint sensitivity system shown in Eq. (3.14) takes on the following particular form:

$$\begin{pmatrix} -\frac{d}{dt}+\lambda_1^0 & -\lambda_1^0 & 0 \\ 0 & -\frac{d}{dt}+\lambda_2^0 & -\lambda_2^0 \\ 0 & 0 & -\frac{d}{dt}+\lambda_3^0 \end{pmatrix} \begin{pmatrix} \psi_1(t) \\ \psi_2(t) \\ \psi_3(t) \end{pmatrix} = \begin{pmatrix} 0 \\ \lambda_2^0 \delta\left(t-t_j\right) \\ 0 \end{pmatrix}, \tag{3.27}$$

subject to the same final-time conditions as shown in Eq. (3.15). The solution to the above final-time problem is readily obtained in the form

$$\begin{gathered} \psi_3(t) \equiv 0,\ \psi_2(t) = \lambda_2^0 e^{-\lambda_2^0\left(t_j-t\right)} H\left(t_j-t\right), \\ \psi_1(t) = \frac{\lambda_1^0 \lambda_2^0}{\lambda_2^0-\lambda_1^0}\left(e^{-\lambda_2^0\left(t_j-t\right)} - e^{-\lambda_1^0\left(t_j-t\right)}\right) H\left(t_j-t\right). \end{gathered} \tag{3.28}$$

Taking into account the expression of the direct effect term from Eq. (3.26), inserting the expressions obtained in Eq. (3.28) into the general form given in Eq. (3.16), and performing the respective integration yields the following expressions for the non-zero sensitivities of $R_1(\boldsymbol{u},\boldsymbol{\alpha})$:

$$\begin{aligned} &\frac{\partial R_2}{\partial \lambda_3} \equiv 0,\quad \frac{\partial R_2}{\partial N_{10}} = \psi_1(0) = \frac{\lambda_1^0 \lambda_2^0}{\lambda_2^0-\lambda_1^0}\left(e^{-\lambda_1^0 t_j} - e^{-\lambda_2^0 t_j}\right), \\ &\frac{\partial R_2}{\partial \lambda_1} = N_{10}^0 \frac{\lambda_1^0 \lambda_2^0 t_j}{\lambda_1^0-\lambda_2^0} e^{-\lambda_1^0 t_j} + N_{10}^0 \left(\frac{\lambda_2^0}{\lambda_2^0-\lambda_1^0}\right)^2 e^{-\lambda_1^0 t_j} - N_{10}^0 \left(\frac{\lambda_2^0}{\lambda_2^0-\lambda_1^0}\right)^2 e^{-\lambda_2^0 t_j} \\ &\frac{\partial R_2}{\partial \lambda_2} = N_2^0\left(t_j\right) - \frac{\lambda_1^0 \lambda_2^0 N_{10}^0}{\lambda_2^0-\lambda_1^0}\left(\frac{e^{-\lambda_1^0 t_j} - e^{-\lambda_2^0 t_j}}{\lambda_2^0-\lambda_1^0} - t_j e^{-\lambda_2^0 t_j}\right). \end{aligned} \tag{3.29}$$

3.1.1.3 Measurements of $A_3(t) \equiv \lambda_3 N_3\left(t_k\right),\ k = 1,\ldots,n_3.$

Consider now that values $A_3(t) \equiv \lambda_3 N_3\left(t_k\right),\ k = 1,\ldots,n_3,$ of the time-dependent activity of the radioactive substance $N_3(t)$, are measured at n_3 instances $t_k,\ k = 1,\ldots,n_3$, in time. These *measured responses* may or may not be correlated. As before, the response $R_3\left(\boldsymbol{u},\boldsymbol{\alpha}\right)$ can be represented mathematically as a functional of the form

$$R_3\left(\boldsymbol{u},\boldsymbol{\alpha}\right) \equiv \int_0^{t_f} \lambda_3 N_3\left(t\right)\delta\left(t-t_k\right)dt, \tag{3.30}$$

where t_f denotes the (finite or infinite) final-time value to be considered for this problem. The sensitivities of the above response to variations $\boldsymbol{h}_u$ and $\boldsymbol{h}_\alpha$ given by the Gateaux-differential, $DR_3\left(\boldsymbol{u}^0,\boldsymbol{\alpha}^0;\boldsymbol{h}_u,\boldsymbol{h}_\alpha\right)$, of $R_3\left(\boldsymbol{u},\boldsymbol{\alpha}\right)$, which is obtained as

$$\begin{gathered} DR_3\left(\boldsymbol{u}^0,\boldsymbol{\alpha}^0;\boldsymbol{h}_u,\boldsymbol{h}_\alpha\right) = \left(DR_3\right)_{dir} + \left(DR_3\right)_{in}, \text{ where} \\ \left(DR_3\right)_{dir} \equiv \left(\delta\lambda_3\right)N_3^0\left(t_k\right), \; \left(DR_3\right)_{in} \equiv \int_0^{t_f} \lambda_3^0 h_3\left(t\right)\delta\left(t-t_k\right)dt. \end{gathered} \tag{3.31}$$

The direct effect term, $\left(DR_3\right)_{dir}$, can be evaluated immediately, while the indirect effect term $\left(DR_3\right)_{in}$ will be evaluated using the adjoint (*ASAP*) sensitivity analysis procedure. For the particular form of $\left(DR_3\right)_{in}$ defined in Eq. (3.31), the adjoint sensitivity system shown in Eq. (3.14) takes on the following particular form:

$$\begin{pmatrix} -\frac{d}{dt}+\lambda_1^0 & -\lambda_1^0 & 0 \\ 0 & -\frac{d}{dt}+\lambda_2^0 & -\lambda_2^0 \\ 0 & 0 & -\frac{d}{dt}+\lambda_3^0 \end{pmatrix} \begin{pmatrix} \psi_1\left(t\right) \\ \psi_2\left(t\right) \\ \psi_3\left(t\right) \end{pmatrix} = \begin{pmatrix} 0 \\ 0 \\ \lambda_3^0\delta\left(t-t_k\right) \end{pmatrix}, \tag{3.32}$$

subject to the same final-time conditions given in Eq. (3.15). Solving the above final-time problem gives

$$
\begin{aligned}
&\psi_3(t) = \lambda_3^0 e^{-\lambda_3^0(t_k - t)} H(t_k - t), \\
&\psi_2(t) = \frac{\lambda_3^0 \lambda_2^0}{\lambda_3^0 - \lambda_2^0}\left(e^{-\lambda_3^0(t_k - t)} - e^{-\lambda_2^0(t_k - t)}\right) H(t_k - t), \\
&\psi_1(t) = \lambda_3^0 \lambda_2^0 \lambda_1^0 H(t_k - t) \times \\
&\quad \times \left[\frac{e^{-\lambda_1^0(t_k - t)}}{(\lambda_2^0 - \lambda_1^0)(\lambda_3^0 - \lambda_1^0)} + \frac{e^{-\lambda_2^0(t_k - t)}}{(\lambda_1^0 - \lambda_2^0)(\lambda_3^0 - \lambda_2^0)} + \frac{e^{-\lambda_3^0(t_k - t)}}{(\lambda_3^0 - \lambda_1^0)(\lambda_3^0 - \lambda_2^0)}\right].
\end{aligned}
\tag{3.33}
$$

Taking into account the expression of the direct effect term from Eq. (3.31), inserting the expressions from the adjoint functions from Eq. (3.22) into the general form given in Eq. (3.16), and performing the respective integration yields the following expressions for the non-zero sensitivities of $R_3(\boldsymbol{u},\boldsymbol{\alpha})$:

$$
\begin{aligned}
&\frac{\partial R_3}{\partial N_{10}} = \psi_1(0) = \lambda_3^0 \lambda_2^0 \lambda_1^0 \times \\
&\quad \times \left[\frac{e^{-\lambda_1^0 t_k}}{(\lambda_2^0 - \lambda_1^0)(\lambda_3^0 - \lambda_1^0)} + \frac{e^{-\lambda_2^0 t_k}}{(\lambda_1^0 - \lambda_2^0)(\lambda_3^0 - \lambda_2^0)} + \frac{e^{-\lambda_3^0 t_k}}{(\lambda_1^0 - \lambda_3^0)(\lambda_2^0 - \lambda_3^0)}\right]; \\
&\frac{\partial R_3}{\partial \lambda_1} = \frac{(\lambda_2^0)^2 \lambda_3^0}{(\lambda_1^0 - \lambda_2^0)^2 (\lambda_3^0 - \lambda_2^0)} N_{10}^0 \left(e^{-\lambda_1^0 t_k} - e^{-\lambda_2^0 t_k}\right) + \frac{\lambda_2^0 (\lambda_3^0)^2}{(\lambda_1^0 - \lambda_3^0)^2 (\lambda_2^0 - \lambda_3^0)} N_{10}^0 \left(e^{-\lambda_1^0 t_k} - e^{-\lambda_3^0 t_k}\right) \\
&\quad - \frac{\lambda_1^0 \lambda_2^0 \lambda_3^0}{(\lambda_2^0 - \lambda_1^0)^2 (\lambda_3^0 - \lambda_1^0)} N_{10}^0 t_k e^{-\lambda_1^0 t_k}; \\
&\frac{\partial R_3}{\partial \lambda_2} = \frac{\lambda_3^0}{\lambda_2^0} N_3^0(t_k) + N_{10}^0 \lambda_1^0 \lambda_2^0 \lambda_3^0 \left[-\frac{e^{-\lambda_1^0 t_k}}{(\lambda_2^0 - \lambda_1^0)^2 (\lambda_3^0 - \lambda_1^0)} - \frac{t_k e^{-\lambda_2^0 t_k}}{(\lambda_1^0 - \lambda_2^0)(\lambda_3^0 - \lambda_2^0)}\right. \\
&\quad \left. + \frac{e^{-\lambda_2^0 t_k}}{(\lambda_1^0 - \lambda_2^0)^2 (\lambda_3^0 - \lambda_2^0)} + \frac{e^{-\lambda_2^0 t_k}}{(\lambda_1^0 - \lambda_2^0)(\lambda_3^0 - \lambda_2^0)^2} - \frac{e^{-\lambda_3^0 t_k}}{(\lambda_1^0 - \lambda_3^0)(\lambda_2^0 - \lambda_3^0)^2}\right]; \\
&\frac{\partial R_3}{\partial \lambda_3} = N_3^0(t_k) + N_{10}^0 \lambda_1^0 \lambda_2^0 \lambda_3^0 \left[-\frac{e^{-\lambda_1^0 t_k}}{(\lambda_2^0 - \lambda_1^0)(\lambda_3^0 - \lambda_1^0)^2} - \frac{e^{-\lambda_2^0 t_k}}{(\lambda_1^0 - \lambda_2^0)(\lambda_3^0 - \lambda_2^0)^2}\right. \\
&\quad \left. - \frac{t_k e^{-\lambda_3^0 t_k}}{(\lambda_1^0 - \lambda_3^0)(\lambda_2^0 - \lambda_3^0)} + \frac{e^{-\lambda_3^0 t_k}}{(\lambda_2^0 - \lambda_1^0)(\lambda_3^0 - \lambda_1^0)^2} + \frac{e^{-\lambda_3^0 t_k}}{(\lambda_1^0 - \lambda_2^0)(\lambda_3^0 - \lambda_2^0)^2}\right].
\end{aligned}
\tag{3.34}
$$

3.1.2 Best-Estimate Predictions after Data Assimilation and Model Calibration

As a specific example of a radioactive decay chain involving three nuclides, consider the decay of iodine into cesium:

$$\begin{array}{ccccc} {}^{135}_{53}I & \xrightarrow[T_{1/2}=6.7h]{\beta^-} & {}^{135}_{54}Xe & \xrightarrow[T_{1/2}=9.2h]{\beta^-} & {}^{135}_{55}Cs \quad (\text{almost stable}) \\ (N_1) & & (N_2) & & (N_3) \end{array} \tag{3.35}$$

where the radioactive constants $\lambda_1, \lambda_2, \lambda_3$ have the following nominal values:

$$\begin{aligned} \lambda_1^0 &= 0.10345\ \mathrm{h}^{-1} & (T_{1/2} &= 6.7\ \text{hours}) \\ \lambda_2^0 &= 0.07534\ \mathrm{h}^{-1} & (T_{1/2} &= 9.2\ \text{hours}) \\ \lambda_3^0 &= 2.6660 \cdot 10^{-5}\ \mathrm{y}^{-1} & (T_{1/2} &= 2.6 \cdot 10^4\ \text{years}) \end{aligned} \tag{3.36}$$

For an initial quantity of iodine $N_1(0) = N_{10}^0 = 10\,mol$, the time-dependent behaviour of the solutions of Eqs. (3.03) through (3.05) are depicted in Figure 3.01.

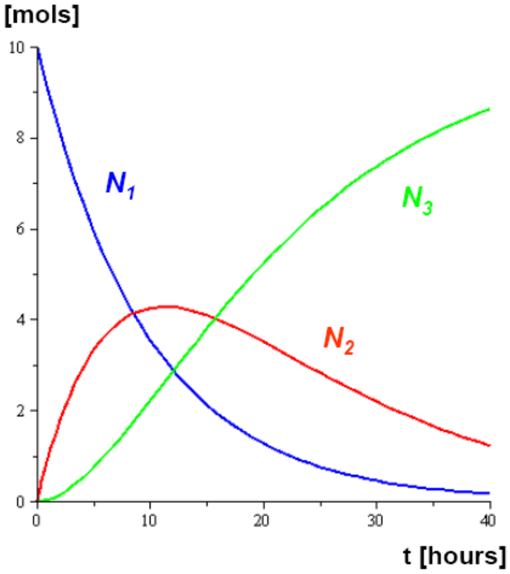

Figure 3.01: Time-variation of the nuclides following the decay chain defined in (3.35).

Consider next that the radionuclides' activities are measured during the first 40 hours of the transient radioactive decay process. These activities are therefore the "measured responses". The corresponding computed responses (activities) are readily obtained by multiplying the respective number densities (see Figure 3.01, above) with the corresponding decay constants, and their behavior in the time interval 0-40 hours is displayed in Figure 3.02. It turns out that the activity of the third isotope (Cs) is negligible (6 orders of magnitude smaller) compared with those of the Iodine and Xenon and will therefore not be considered for data assimilation and model calibration. In the following, the activity of the Iodine nuclei will be denoted by the "response" $R_1 = \lambda_1 N_1$ and the activity of the Xenon nuclei will be denoted by the "response" $R_2 = \lambda_2 N_2$.

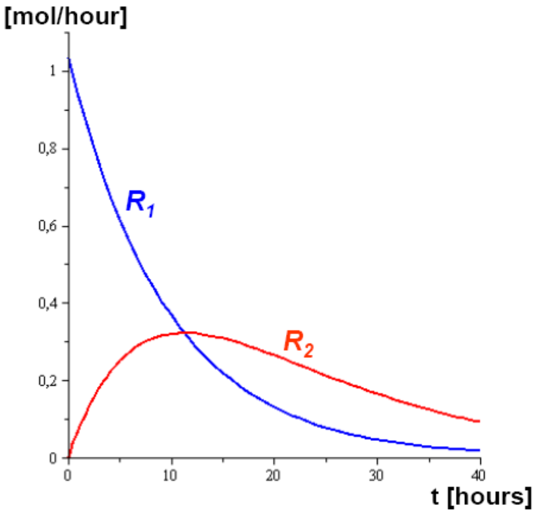

Figure 3.02: Time-dependent activities of Iodine (R_1) and Xenon (R_2).

The uncertainty, and therefore adjustable, to be considered for the data assimilation and calibration procedure are the decay constants λ_1, λ_2 and the initial quantity of Iodine isotope (N_{10}). Figure 3.03 shows the relative sensitivities of the two responses [see Eq. (3.29)] to the three system parameters. The activity of Iodine (R_1) is not sensitive to λ_2.

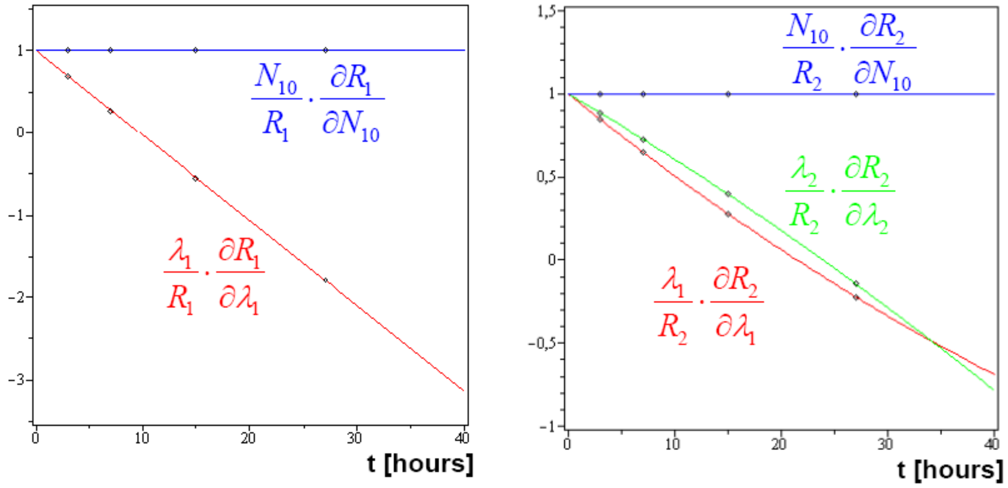

Figure 3.03: Relative sensitivities of the activities R_1 (left) and R_2 (right) to the parameters N_{10}, λ_1 and, respectively, N_{10}, λ_1, λ_2.

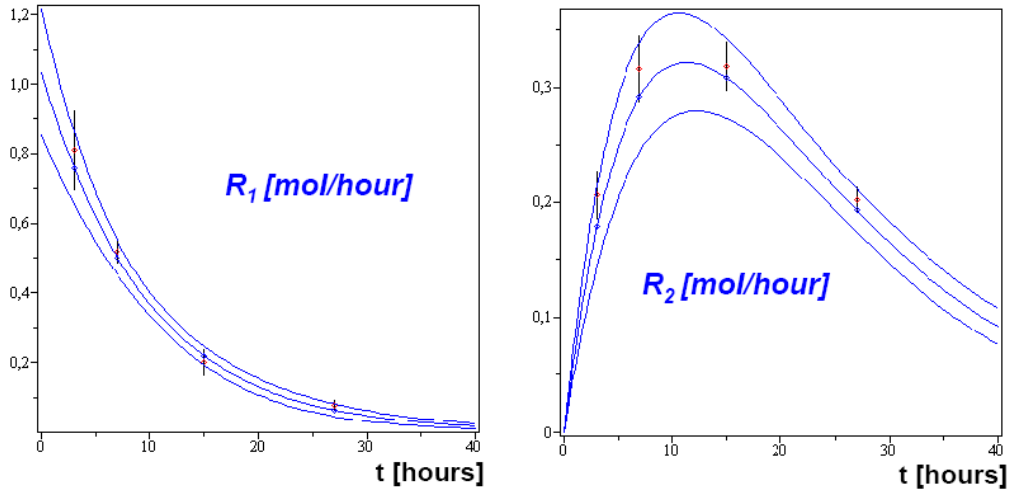

Figure 3.04: Nominal values of computed responses and their corresponding error bands (standard deviations) derived from error propagation. Red dots denote consistent "measured" responses (for R_1 and R_2) at four time nodes: 3, 7, 15 and 27 hours, with corresponding standard deviations.

In Figure 3.04, the nominal values of the computed responses are depicted by the middle lines. On each side of the computed nominal values, are the lines depicted the computed standard deviations that arise from the propagation of the following relative standard deviations of the system parameters:

$$\sigma_{rel}\left(N_{10}\right)=9\%,\quad \sigma_{rel}\left(\lambda_1\right)=15\%,\quad \sigma_{rel}\left(\lambda_2\right)=13\% \tag{3.37}$$

Four consistent "experimental" measurements, depicted as red-dots in Figure 3.04, are considered to be available at 3, 7, 15, and 27 hours, respectively. The consistency indicator for these measurements is $\chi^2 = 2.463/8$ indicating that the experimental and computational information to be considered posed for data assimilation is consistent. Using the BEST-EST software module for assimilating and calibrating both responses and parameters simultaneously, the resulting best-estimate relative standard deviations of the system parameters are:

$$\sigma_{rel}\left(N_{10}\right) = 3.09\%, \quad \sigma_{rel}\left(\lambda_1\right) = 6.93\%, \quad \sigma_{rel}\left(\lambda_2\right) = 8.14\% . \tag{3.38}$$

As expected for a consistent data assimilation and model calibration procedure, the errors in the considered parameters have been clearly reduced, as indicated by comparing the best-estimate results in (3.38) with the initial ones in (3.37). The relative standard deviation for λ_2 is not so strongly reduced because only R_2 is sensitive to λ_2.

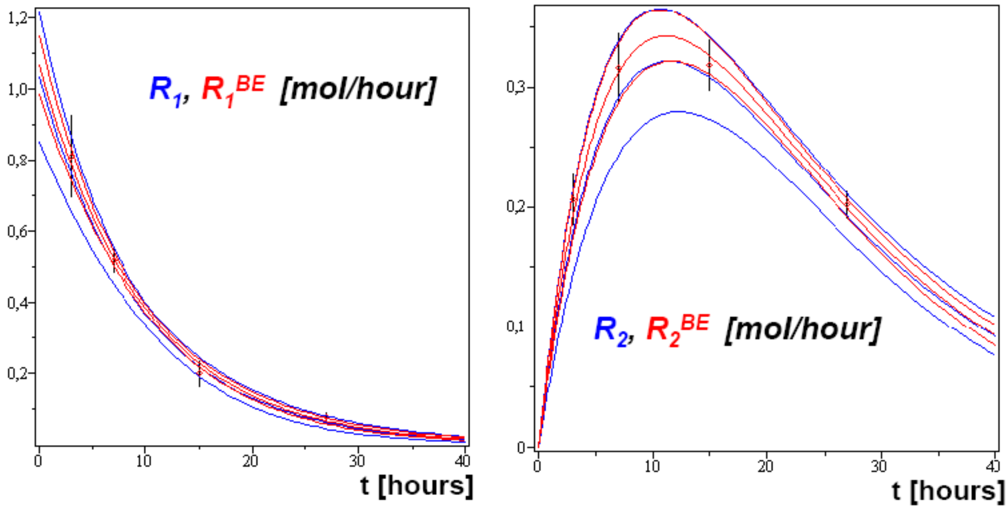

Figure 3.05: Initial (R_i, in blue) and adjusted (R_i^{BE}, in red) responses (central lines) with corresponding standard deviations (side lines). The eight "experimental" points used for the data adjustment (four for each response) and their standard deviations are also displayed.

After data assimilation, the new values of the best-estimate responses, depicted in red in Figure 3.05, fall in between the computed and measured values, and their uncertainities have been reduced by about 50%. These results clearly demonstrate the value of combining consistent measurements and computations for reducing uncertainties in predicted best-estimate quantities.

3.2 Large-Scale Application: Data Assimilation and Model Calibration of the FLICA4 3D Thermal-Hydraulics Code using the NUPEC BFBT Experiments

This Chapter demonstrates an application of the time-dependent best-estimate data assimilation and model calibration methodology presented in Section 1.2 and programmed in the software module BES-EST to a large-scale three-dimensional reactor thermal-hydraulics experimental facility simulated using the code system FLICA4 developed at CEA/France. The experimental information used for calibrating FLICA4-parameters stems from the international OECD/NRC BWR Full Size Fine-Mesh Bundle Tests (BFBT) benchmarks, which were designed by the Nuclear Power Engineering Corporation (NUPEC) of Japan for enabling systematic validation of simulation tools using full-scale experimental data. The following specific BFBT experiments will be used in this work for calibrating parameters and boundary conditions for FLICA4: (i) one-dimensional pressure drops; (ii) axial void fraction distributions; and (iii) three-dimensional transverse void fraction distributions. The resulting uncertainties for the best-estimate parameters and distributions of pressure drops and void fractions will be shown to be smaller than the a priori experimental and computed uncertainties, thus demonstrating the successful calibration of a large-scale reactor core thermal-hydraulics code using the BFBT benchmark-grade experiments.

Section 3.2.1 describes the experimental set-up of the BFBT benchmarks. The Nuclear Power Engineering Corporation (NUPEC) of Japan designed these experiments for enabling a systematic validation of numerical simulation models using full-scale experimental data. The BFBT benchmarks are particularly well suited for quantifying uncertainties in predictions of detailed distributions of sub-channel void fraction and critical powers. Section 3.2.1.1 presents the description of the BFBT experimental loop facility and test section, while Section 3.2.1.2 highlights the methods for measuring pressures drops, as well as static and transient void fraction distributions. Section 3.2.1.3 presents the geometrical description and material properties of the BWR fuel assembly mock-up used in the respective BFBT measurements.

Section 3.2.2 comprises four subsections, which present the procedure and best-estimate results following the calibration of model parameters in FLICA4, in conjunction with the assimilation of experimental data from the NUPEC BFBT experiments [Neykov et al., 2006]. To begin with, Section 3.2.2.1 presents the high fidelity FLICA4 simulations that have been performed for the following benchmark measurements: (i) pressure drops stemming from steady one-dimensional FLICA4-simulations; (ii) axial void fractions distributions stemming from transient one-dimensional FLICA4-simulations; and (iii) transversal void fraction distributions stemming from steady three-dimensional FLICA4-simulations, at sub-channel level with cross-flow.

3.2.1 Description of the BFBT experiments

From 1987 to 1995, the Nuclear Power Engineering Corporation of Japan (NUPEC) performed measurements [Inoue et al., 1995] of void fraction distribution in full-size mock-up fuel bundles for both boiling water reactors (BWRs) and pressurized water reactors (PWRs). The void fraction distributions were visualized using computer tomography (CT) technology under actual plant conditions for mesh sizes smaller than a sub-channel. In addition to measuring void fraction distributions, NUPEC also performed steady state and transient measurement of critical power in equivalent full-size mock-ups. The NUPEC measurements are internationally considered to be highly reliable because of the high reliability of the experimental facility, including control of the system pressure, inlet sub-cooling, and rod surface temperature. Thus, these measurements provide internationally a comprehensive database for the development of consistent mechanistic models for predicting void fraction distributions and boiling transition in sub-channels.

Gaining accurate knowledge about boiling transition and void fraction distribution is essential for the quantification of nuclear reactor safety margins. However, the theoretical principles underlying the numerical modeling of sub-channel void distribution are incompletely known, and the correlations replacing first-principles are not generally applicable to the wide range of geometrical arrangements and operating conditions found in operating LWRs of various types. The international OECD/NRC BWR Full-Size Fine-Mesh Bundle Tests (BFBT) benchmarks [Neykov et al., 2006] were established based on the NUPEC database to motivate research on insufficiently known two-phase flow regimes by facilitating a systematic comparison of full-scale experimental data to predictions of numerical simulation models. These benchmarks are particularly well suited for quantifying uncertainties in the prediction of detailed distributions of sub-channel void fractions and critical powers.

The design and data acquisition systems of NUPEC's facility enable both macroscopic and microscopic measurements. In this context, measurement of sub-channel void fractions are considered as macroscopic data, while the digitized computer graphic images are considered as microscopic data. Thus, the BFBT measurements of void fraction distributions and critical powers in a multi-rod assembly under typical reactor power and fluid conditions enable comparisons with predictions of computational models and encourage the development of new theoretical models focusing more on microscopic processes.

3.2.1.1 Experimental Loop Facility and Test Section

By using an electrically heated rod assembly that simulates a full scale BWR fuel assembly, NUPEC's BWR Full-size Fine-mesh Bundle Test (BFBT) facility is able to simulate the high-pressure and high temperature fluid conditions characteristic of operating BWRs.

3.2.1.1.1 Experimental Loop Facility

Figure 3.06 shows the diagram of the BFBT experimental loop facility. The facility enables steady-state simulations that span the full range of BWR operating conditions, as well as time-dependent simulations of complex BWR operational transients. The limiting operating conditions for the facility are as follows: pressure up to 10.3 MPa, temperature up to 315 °C, power up to 12 MW, and flow rate up to 75 t/h.

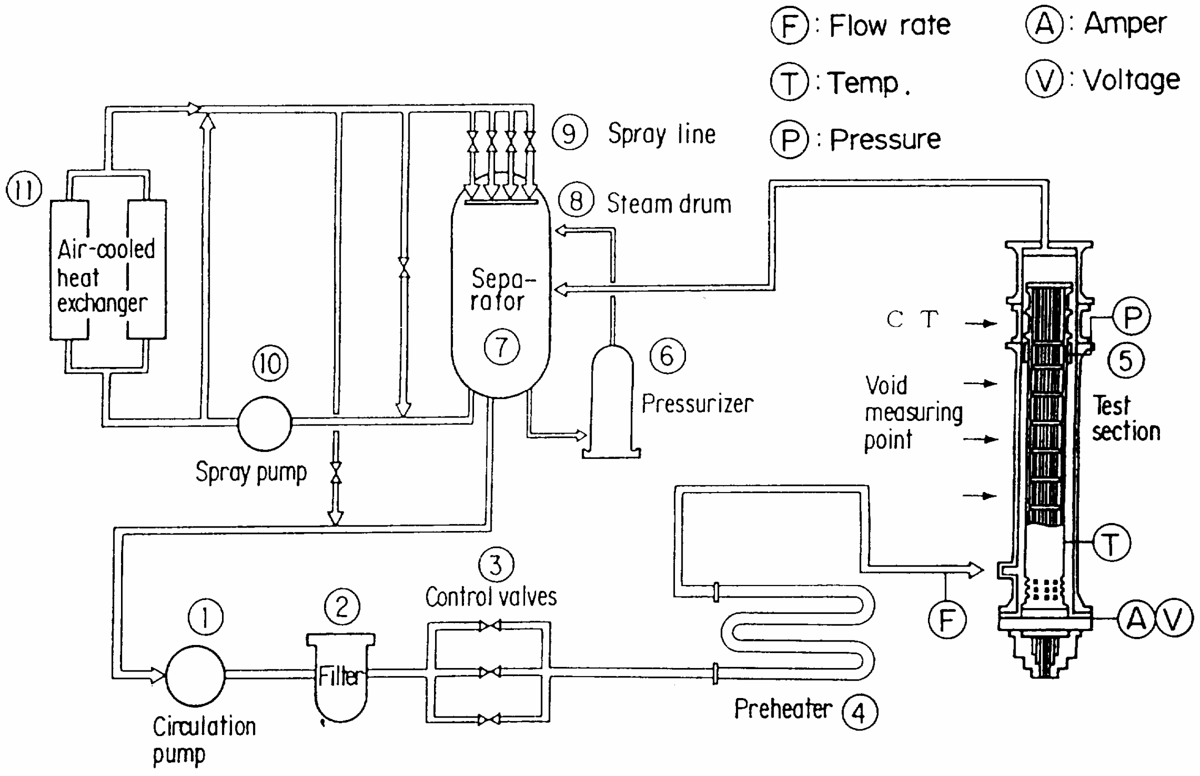

Figure 3.06: Facility for NUPEC Rod Bundle Test Series

The main structural components are made of stainless steel (SUS304). De-mineralized water is used as a cooling fluid. As depicted in Figure 3.06, water is circulated by the circulation pump (1); the three valves (3) of different sizes control the coolant flow rate. A direct-heating tubular pre-heater (4) controls the inlet fluid temperature for the test section (5). Sub-cooled coolant flows upward into the test bundle (5), in which it is heated to become a two-phase mixture. The steam is separated from the steam-water mixture in the separator (7) and is condensed using a spray of sub-cooled water in the steam drum (8). The condensed water is then returned to the circulation pump (1). The spray lines (9), which have four different-sized valves, control the system pressure in both steady and transient state. The pressurizer (6) controls the system pressure when the power in the test section is low. After the water is cooled with two air-cooled heat exchangers (11), the spray pump (10) forces a spray into the steam-drum. The operation range of the test loop depicted in Figure 3.06 covers the full range of BWR steady-state operating conditions.

3.2.1.1.2 Test Section

Figure 3.07 depicts the test section, which comprises a pressure vessel, a simulated flow channel, and electrodes, and a full-scale BWR mock-up fuel assembly installed within the vessel. Although two types of BWR bundles (a current 8x8 type and a high burn-up 8x8 type) were simulated in the BFBT experiments, this work considers only the experiments involving the “high burn-up” 8×8 mock-up; its characteristic dimensions are listed in Table 3.01. Each rod in the test assembly is heated electrically to simulate the actual operating conditions for a reactor fuel rod. The cladding, insulator, and heater are made of inconel, boron nitride, and nichrome, respectively.

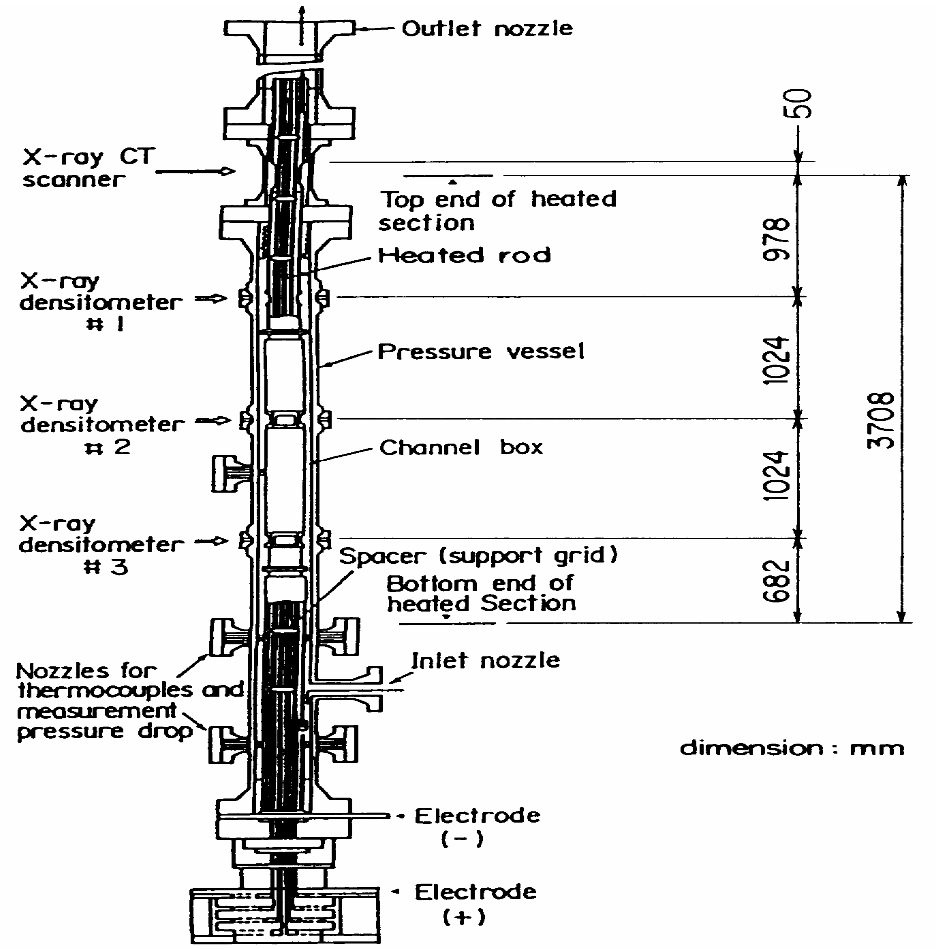

Figure 3.07: Cross Sectional View of Test Section

Items	High burnup 8×8
Number of fuel rods Outer diameter (mm) Heated length (m) Number of water rod Outer diameter of water rod (mm) Rod pitch (mm) Width of channel box Number of spacer Spacer type	60 12.3 3.7 1 34.0 16.2 132.5 7 Ferrule

Table 3.01: Characteristics of BWR Test Bundles

3.2.1.2 Measurement Methods

This section highlights the measurement methods for the static and transient void fraction distributions (Sec.3.2.1.2.1), and for the pressures drop measurements (Sec.3.2.1.2.2).

3.2.1.2.1 Void Fraction Distribution (Static and Transient)

The X-ray computerized tomography (CT) scanner and the X-ray densitometer were used as shown in Figure 3.08 (a) for measuring void fraction distributions. Fine-mesh void distributions were measured under steady-state conditions using the X-ray CT scanner at a point 50 mm above the heated length. Figure 3.08 (b) shows the void fraction measuring section. The pressure vessel is made of titanium, while the channel wall and the cladding of the heater rods at this location are made of beryllium in order to minimize X-ray attenuation in the structure. The X-ray CT measurement system comprises an X-ray tube and 512 detectors at locations shown in Figure 3 (c), attaining a spatial resolution of 0.3 mm × 0.3 mm.

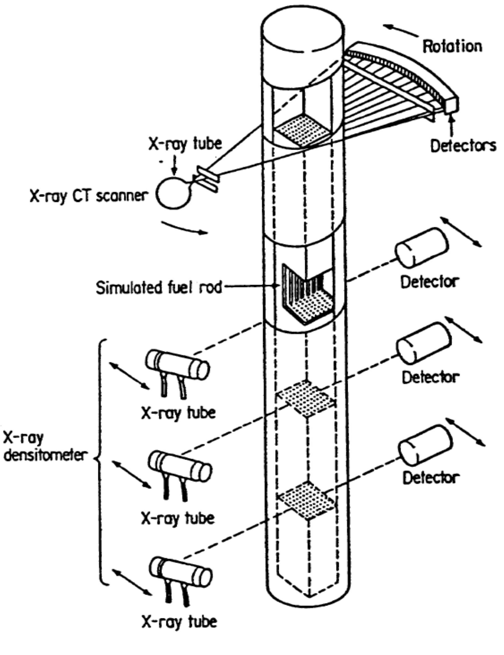

(a) Measuring structure

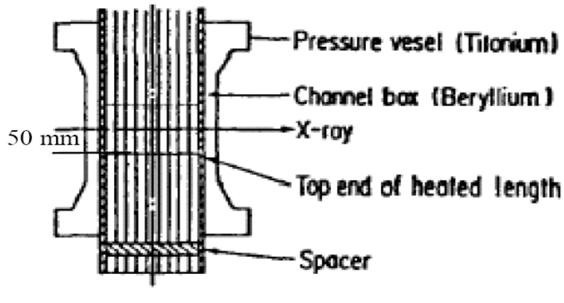

(b) Scanning section

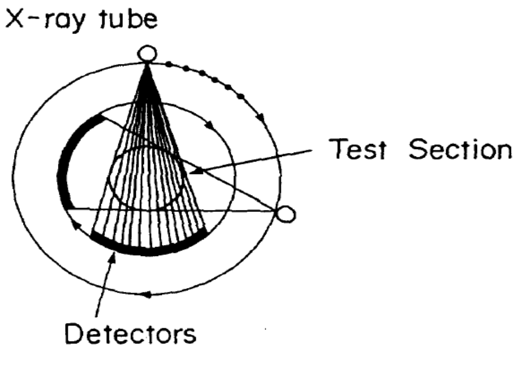

(c) Scanning method

Figure 3.08: Void fraction measurement system

The cross-sectional average transient void fraction distributions were measured by the X-ray densitometer at 3 elevations (at elevations 682, 1706, 2730 mm, from bottom to top, in Figure 3.07. To enable these measurements, the channel sections at these elevations were made of beryllium, and the heater rods were clad with beryllium having the same diameter as the Inconel portion of the heater rod.

Scan method	360^o rotation with pulse X-rays
Type of X-ray beam	Fan-shaped X-ray beam of 34^o radiation angle
Voltage of X-ray tube	Max. 120 kV
Current	Max 400mA
Scanning time	15s
Scanning region	D=300 mm
Dimensions of reconstruction element	0.3mm X 0.3mm

Table 3.02: Specification of X-ray CT Scanner

Table 3.02 shows the basic specifications of the X-ray CT scanner. As a fan-shaped X-ray beam scans an object, the object attenuates the beam; the detectors measure the attenuated beam and record the X-ray intensity data. These records are called "projection data"; complete 360^o projection data were thus obtained. The distribution of the linear attenuation coefficient is obtained by reconstructing the projection data. The reconstruction technique is called a "filter back projection", and has been widely used in the field of nuclear medicine. All void fraction signals from the detectors are calibrated using a signal from a reference detector to improve the signal-to-noise ratio.

The steady state measurements were performed using thermal-hydraulic conditions that would envelope the steady-state parameters characterizing the actual operation of a BWR in terms of the bundle's geometrical configuration, power shape and two-phase flow. The range of test conditions included pressures ranging from 1 MPa to 8.6 MPa, flow rates ranging from 284 kg/m2/s to 1988 kg/m2/s, and exit qualities ranging from 1 to 25%. The X-ray CT scanner and the X-ray densitometer measurements systems were used in the experiments. In particular, the X-ray densitometer was employed for performing transient measurements of the cross-sectional averaged transient void fraction distribution resulting from the combined effects of pressure, flow rate, and power for the following four operational transients: (a) turbine trip without bypass; (b) one pump trip; (c) re-circulation pump tripped; and (d) malfunction of pressure control system (pressure increase).

3.2.1.2.2 Pressure Drop Measurements

Pressure drop measurements were also performed in the loop facility depicted in Figure 3.06. For this purpose, the loop was operated under normal BWR operational conditions and typical transient conditions. The full-scale 8x8 high burn-up fuel assembly mock-up was installed in the test section. The steady-state pressure drop was measured in both single-phase flow and two-phase flow conditions that cover the normal operational behavior. The bundle pressure drop was monitored at several locations, as depicted in Figure 3.09.

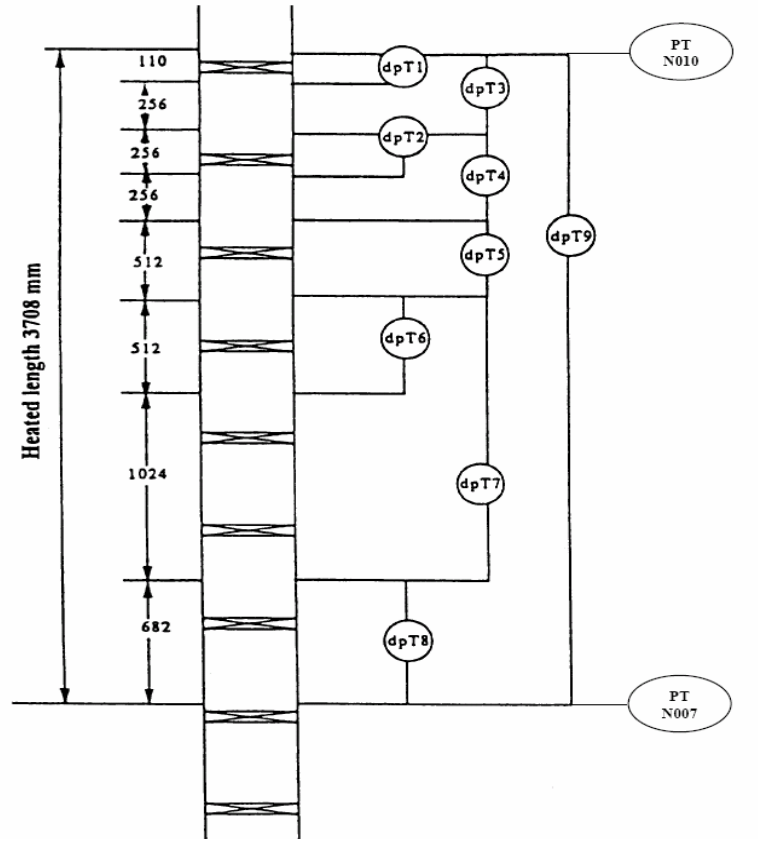

Figure 3.09: Pressure tap locations for pressure drop measurements.

3.2.1.3 **Fuel Assembly Data**

Table 3.03 lists the transversal power profiles for the beginning of operation (type A). Table 3.04 provides geometric information for the 8×8 high burn-up mock-up assembly in addition to the information provided in Table 3.01.

1.15	1.30	1.15	1.30	1.30	1.15	1.30	1.15
1.30	0.45	0.89	0.89	0.89	0.45	1.15	1.30
1.15	0.89	0.89	0.89	0.89	0.89	0.45	1.15
1.30	0.89	0.89			0.89	0.89	1.15
1.30	0.89	0.89			0.89	0.89	1.15
1.15	0.45	0.89	0.89	0.89	0.89	0.45	1.15
1.30	1.15	0.45	0.89	0.89	0.45	1.15	1.30
1.15	1.30	1.15	1.15	1.15	1.15	1.30	1.15

Table 3.03: Transversal Power Shape of Type A for the Test Assembly Type 4.

Item	Data
Test assembly 4	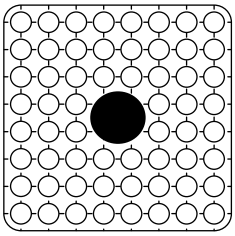
Simulated fuel assembly type	High burn-up 8×8
Number of heated rods	60
Heated rods outer diameter (mm)	12.3
Heated rods pitch (mm)	16.2
Axial heated length (mm)	3708
Number of water rods	1
Water rods outer diameter (mm)	34.0
Channel box inner width (mm)	132.5
Channel box corner radius (mm)	8.0
In channel flow area (mm^2)	9463
Spacer type	Ferrule
Number of spacers	7
Spacer pressure loss coefficients	1.2

Spacer location (mm)	455, 967, 1479, 1991, 2503, 3015, 3527 mm (Distance from bottom of heated length to spacer bottom face)
Transversal power shape	A
Axial power shape	Uniform

Table 3.04: Geometry and Power Shape of the (here used) Assembly Type.

The heated rod is single-ended and electrically grounded. Its structure and dimensions are listed in Table 3.05. The surface temperature of the rod is measured by 0.5 mm-diameter chromel-alumel thermocouples. Additional thermocouples are embedded in the cladding surface, which are positioned axially just upstream of the spacers. Each heated rod is joined to an X-ray transmission section, which is of the same diameter as the heated rod but with cladding made of beryllium in order to facilitate the transmission of X-ray. The thermo-mechanical properties of the heated rod are shown in the Table 3.06 and are based on the MATPRO model used in TRAC code [TRAC-PF1/MOD2 Theory Manual].

Item		Data
Heater	Outer diameter (mm)	7.3
	Material	Nichrome
Insulator	Outer diameter (mm)	9.7
	Material	Boron Nitride
Cladding	Thickness (mm)	1.3
	Material	Inconel 600/Berylium

Table 3.05: Heated rod structure.

	Density ρ (kg/m^3)
Nichrome	8393.4
Boron Nitride	2002
Inconel 600	$16.01846 \times (5.261008 \times 10^2 - 1.345453 \times 10^{-2} T_f - 1.194357 x 10^{-7} T_f^2)$
	Specific heat c_p (J/kg.K)
Nichrome	$110 T_f^{0.2075}$
Boron Nitride	$760.59 + 1.7955 T_f - 8.6704 x 10^{-4} T_f^2 + 1.7955 x 10^{-7} T_f^3$

Inconel 600	$4186.8\times(0.1014+4.378952\times10^{-5}T_f-2.046138\times10^{-8}T_f^{\,2}+$ $1.7955\times10^{-7}T_f^{\,3}-2.060318\times10^{-13}T_f^{\,4}+3.682836\times10^{-16}T_f^{\,5}$ $-2.458648\times10^{-19}T_f^{\,6}+5.597571\times10^{-23}T_f^{\,7})$
	Thermal Conductivity k(W/m.K**)**
Nichrome	$29.18+2.683x10^{-3}\left(T_f-100\right)$
Boron Nitride	$25.27-1.365\times10.3T_f$
Inconel 600	$1.729577\times(8.011332+4.643719\times10^{-3}T_f+1.872857\times10^{-6}T_f^{\,2}-$ $3.914512\times10^{-9}T_f^{\,3}+3.475513\times10^{-12}T_f^{\,4}-9.936696\times10^{-16}T_f^{\,5})$

Table 3.06 Thermo-mechanical properties of heater rod

Spacer grids support the fuel rods in nuclear reactor fuel assemblies. Spacer grids decrease the flow cross sectional area locally, thereby increasing the local velocity pressure drop and heat transfer coefficients. They may have special geometrical features to promote turbulence, the effect of which may propagate further downstream. Spacer grids may provide a larger surface area on which to collect entrained liquid droplets, which may increase the local fluid film flow rate under sub-CHF conditions and may lead to rewetting of the fuel rod cladding under post-CHF conditions. In summary, spacer grids generally have a beneficial effect on critical heat flux (CHF) in typical nuclear reactor assemblies, but the effects depend on their geometrical characteristics pressure, local mass velocity, and quality. Figure 3.10 depicts the ferrule spacer grid used in the BFBT experiments.

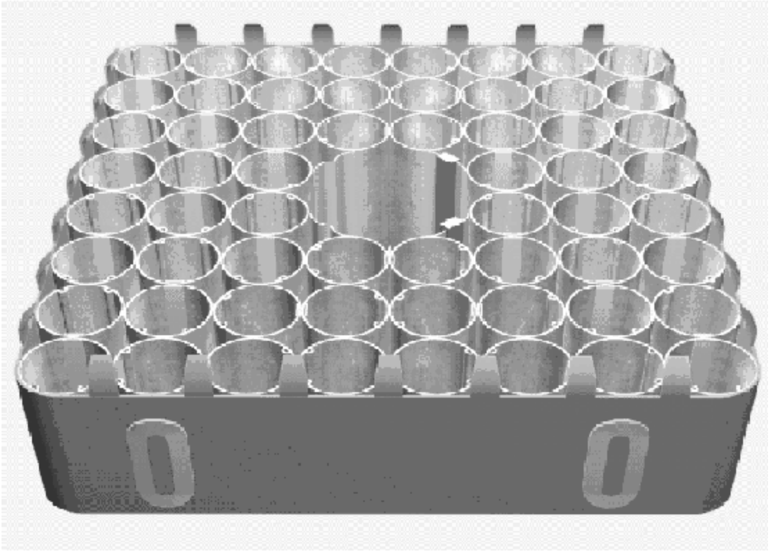

Figure 3.10:.Ferrule spacer grid

3.2.2 Best-Estimate Model Calibration Using the Thermal-Hydraulics Code FLICA4 and Assimilating BFBT Experimental Data

This Section presents the use of selected BFBT experiments within the data assimilation methodology of [Cacuci and Ionescu-Bujor, 2010] to calibrate important parameters in the core thermal-hydraulics code FLICA4 [Fillion et al., 2007, Toumi et al, 2000a, Toumi et al, 2000b, Anyel et al, 2005].

3.2.2.1 FLICA4 Simulations of BFBT Measurements

Using the data described in the Section 3.2.1.3, high fidelity FLICA4 simulations have been performed for 3 classes of measurement benchmarks: (i) pressure drops (steady one-dimensional simulations); (ii) axial void fractions distributions (transient one-dimensional simulations); and (iii) transversal void fraction distributions (steady three-dimensional simulations at sub-channel level with cross-flow). The four rounded corners of the transversal section of the mock-up high burn-up assembly (see Table 3.04) have been modeled using appropriate definitions for the corresponding hydraulic diameter and wet perimeter, respectively, of the channel (for one-dimensional simulations) or sub-channel (for three-dimensional simulations). For three-dimensional simulations, the large central sub-channel was modeled by means of four sub-channels containing cylindrical rods with correspondingly adjusted hydraulic diameters and wet perimeters (see Table 3.04). The steady and, respectively, transient conditions for the benchmark measurements have been modeled in FLICA by designing axial meshes with surfaces that match perfectly the measurement coordinates on the vertical-axis (see Figure 3.11) .

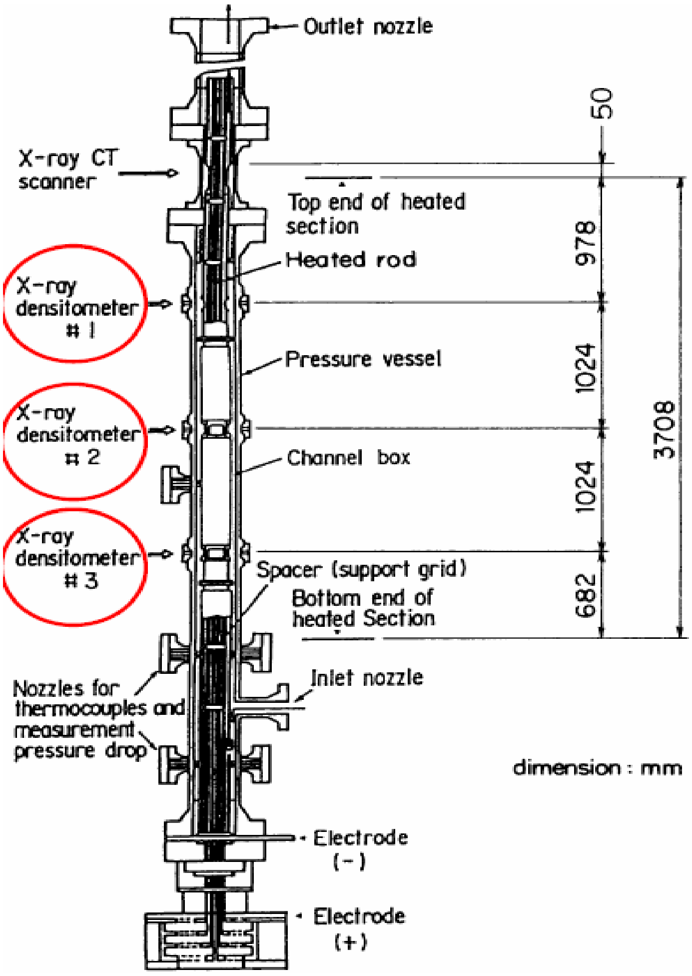

Figure 3.11: Void fraction measurement system.

The specific features of the spatial meshes used in the FLICA4 simulations are as follows:

(A) for the one-dimensional computations of pressure drops and axial void fraction distributions: axial meshes, from bottom to top, as follows: 10 meshes of 64 mm each, followed by one mesh of 42 mm, followed by 46 meshes of 64 mm each, and finally followed by one mesh of 82 mm;

(B) for the three-dimensional computations of transversal void fraction distributions:

(i) axial meshes, from bottom to top, as follows: 50 meshes of 74.16 mm each for modeling the heated length of 3.708 m, followed by 2 meshes of 25 mm each for modeling the X-ray CT-scanner surface (i.e., the unheated length of 50 mm in Figure 3.11); and

(ii) 64 cross-sectional meshes, each modeling one of the sub-channels depicted in the figure inserted in Table 3.04 as follows: (a) four central sub-channels for modeling the center of the mock-up assembly; and (b) 60 sub-channels containing the heated fuel rods. Note that the four corner sub-channels, having one rounded corner and two surfaces facing the exterior, and the 24 lateral sub-channels, having only one surface facing the exterior, have mesh-shapes that differ from those for the interior sub-channels.

The thermo-mechanical properties of the heater rods (see Table 3.06) have also been implemented in FLICA4. These properties play a particularly important role for modeling the transient benchmark, where the thermal coupling between heater rods and fluid is essential for describing correctly the transient behavior. The following correlations have been used in FLICA for simulating the benchmark measurements:

- friction model type F3 [Fillion et al.,2007], corrected by the default model for the wall heating and the biphasic multiplying model of Friedel [Friedel, 1979];
- turbulent mixing and diffusivity coefficients computed with the F3 model [Fillion et al.,2007],
- recondensation model of type F3 [Fillion et al.,2007];
- relative motion between phases described by Ishii's correlation [Ishii, 1977];
- a generic Forster & Greif -like correlation [Forster and Greif, 1958], describing the wall-overheating with respect to saturation, in the regime of completely developed nucleate boiling;
- [Groeneveld-et al., 1996] correlation27 for computing the critical flux and the critical thermal flux ratio (CTFR).

3.2.2.2 Best-Estimate Pressure Drops

The "spacer pressure loss coefficient", K_{loss}, of the ferrule spacer grids of the fuel assembly is a very influential parameter for computing pressure drops in the BFBT experiments, and is also accessible to users of FLICA4 for possible calibration. As listed in Table 3.04, a value of K_{loss} =1.2 was recommended for this coefficient; however, an uncertainty band around this value was not provided. To validate this recommended value, and simultaneously obtain an accompanying standard deviation (uncertainty) for K_{loss}, the BFBT experiments P70031, P70032, and P70033 were selected for use in the data assimilation procedure summarized in the previous Section, in order to obtain a calibrated best-estimate predicted value for K_{loss} , along with the best-estimate uncertainty for this predicted value. The experiments labeled P70031, P70032, P70033 provide single-phase pressure drop measurements for the defining conditions (outlet pressure, inlet temperature, and flow rate) listed in the Table 3.07. The relative standard deviations of these measurements are taken to be 4%.

In order to initiate the calibration of K_{loss} , a starting nominal value of K_{loss} =1.10, together with a relative uncertainty (standard deviation) of 10%, have been deliberately used in FLICA4 to compute the pressures along the mock-up assembly for the experimental conditions listed in Table 3.07. The FLICA4-results, computed using K_{loss} =1.10, are depicted in Figure 3.12 for the three benchmark experiments. The pressure drops corresponding to the upper seven spacer grids (see Figure 3.09) are apparent from the respective discontinuities.

Experiment number	Outlet pressure (MPa)	Inlet temperature (^{0}C)	Flow rate (t/h)	Reynolds number x 10^2
1 (BFBT P70031)	7.16	285.6	39.70	15.81
2 (BFBT P70032)	7.16	285.3	44.60	17.75
3 (BFBT P70033)	7.16	258.7	55.00	21.86

Table 3.07: Defining conditions for pressure drop measurements

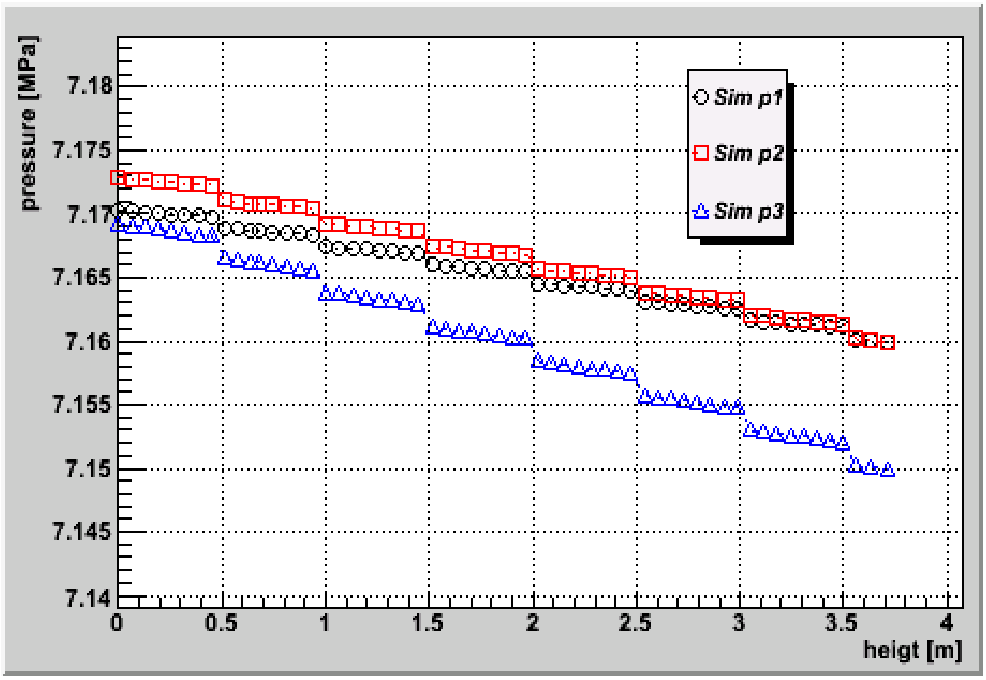

Figure 3.12: FLICA4-computed nominal pressures along the mock-up assembly for the three benchmarks considered in Table 3.07.

The hollow markers in Figure 3.13 represent the normalized ratios between the nominal values of the computed and measured responses. In this figure, the marker-labels 1, 2, and 3 correspond to the BFBT-benchmark experiments P70031, P70032, and P70033 listed in Table 3.08, respectively. Except for "response number 3", which corresponds to the ratio "computation-to-measurement" between elevations 3342 mm and 3708 mm, the other hollow markers in Figure 3.13 clearly indicate a systematic bias, in that the computations yield pressure drops that are smaller than the corresponding measurements. In turn, this systematic bias indicates that the chosen nominal value of $K_{loss} = 1.10$ needs to be calibrated.

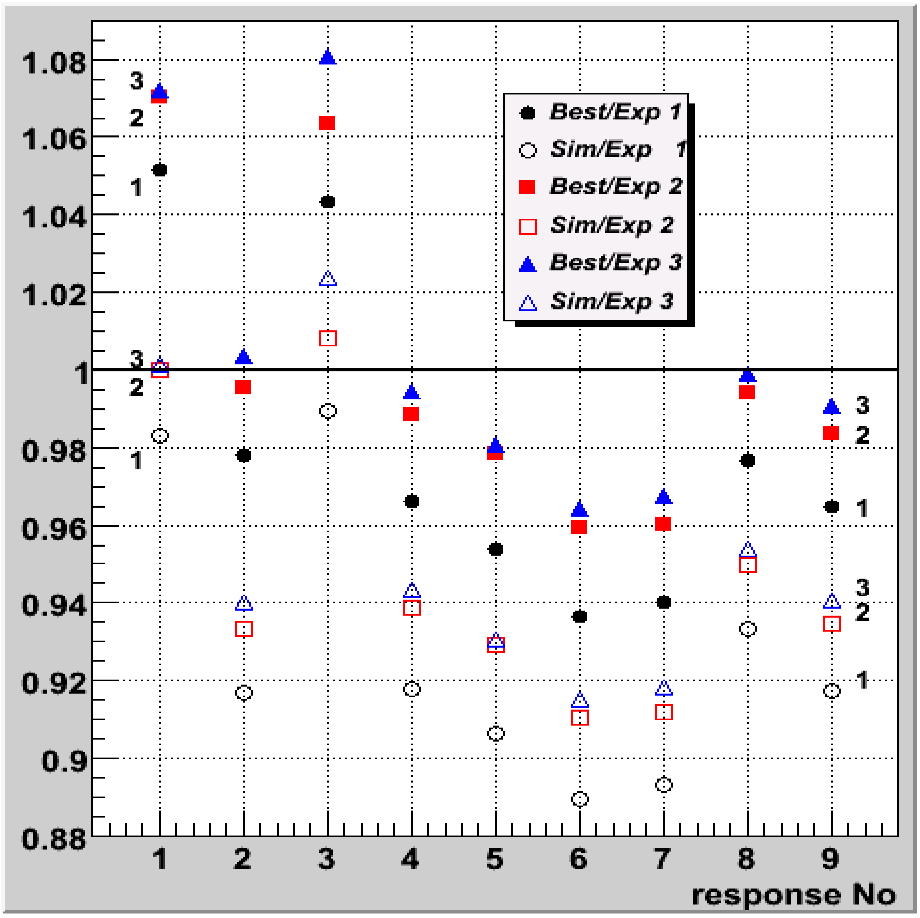

Figure 3.13: Normalized nominal (before calibration) and best estimate (after calibration) pressure drop responses for the 3 benchmark experiments.

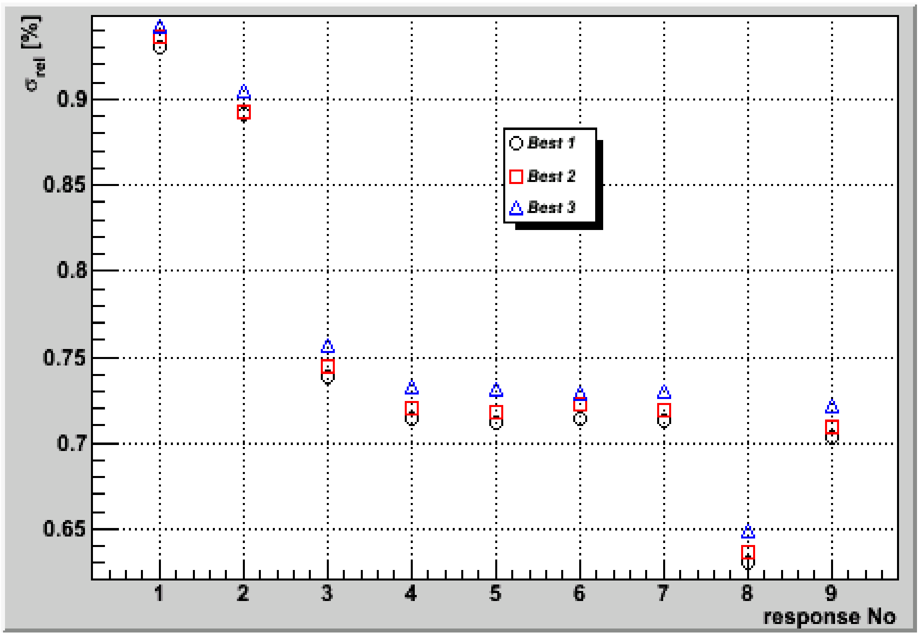

Figure 3.14: Relative standard deviations of the best-estimated pressure drop responses for the three benchmark-experiments.

The spacer pressure loss coefficient K_{loss} will now be calibrated using the data assimilation procedure of [Cacuci and Ionescu-Bujor, 2010] applied simultaneously to all three benchmarks listed in Table 3.07, using the computational module BESTEST. As shown in Table 3.08, the relative sensitivities of the FLICA4-computed responses to K_{loss} are fairly uniformly important for all 27 responses, ranging from 51.09% for response number 8 (measured between elevations 0 and 682 mm) of experiment number 1, to 78.11% for response number 1 (measured between elevations 3598 mm and 3708 mm) of experiment number 3.

Resp. No. Exp. No.	1	2	3	4	5	6	7	8	9
P70031	77.04	73.65	60.25	58.21	57.97	58.21	58.14	51.09	57.26
P70032	77.64	73.78	60.80	58.71	58.51	58.90	58.66	51.61	57.82
P70033	78.11	74.85	61.87	5976	59.63	59.50	59.62	52.58	58.83

Table 3.08: Relative (%)-sensitivities for K_{loss}

The above sensitivities were used together with the standard deviation of the parameter K_{loss} in Eq. (3.11), within BESTEST, to obtain the covariance matrix, C_{rc}, of the computed responses. This covariance matrix is shown in Figure 3.15, which underscores the fact that covariance matrices usually obscure somewhat the extent of correlations among its elements. Actually, the elements of C_{rc} are expected to be fully correlated since a single model parameter (namely K_{loss}) is considered in FLICA4 for data assimilation and calibration. This expectation is confirmed by the results for the correlation matrix of the computed responses, which is depicted in Figure 3.16: as expected, all of its entries are unity. The results for the relative standard deviations of the computed responses are listed in Table 3.09. The absolute values of the respective standard deviations can be obtained by using the relative values in conjunction with the nominal computed response values shown in Figure 3.12.

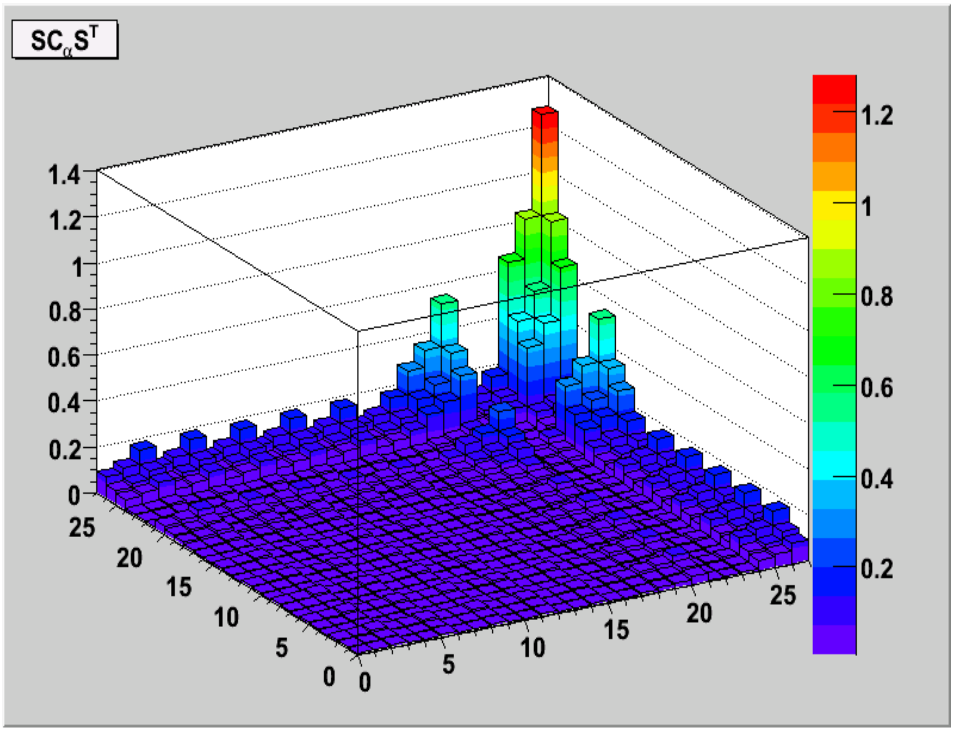

Figure 3.15: Covariance matrix for the computed responses for the three experiments described in Table 3.07.

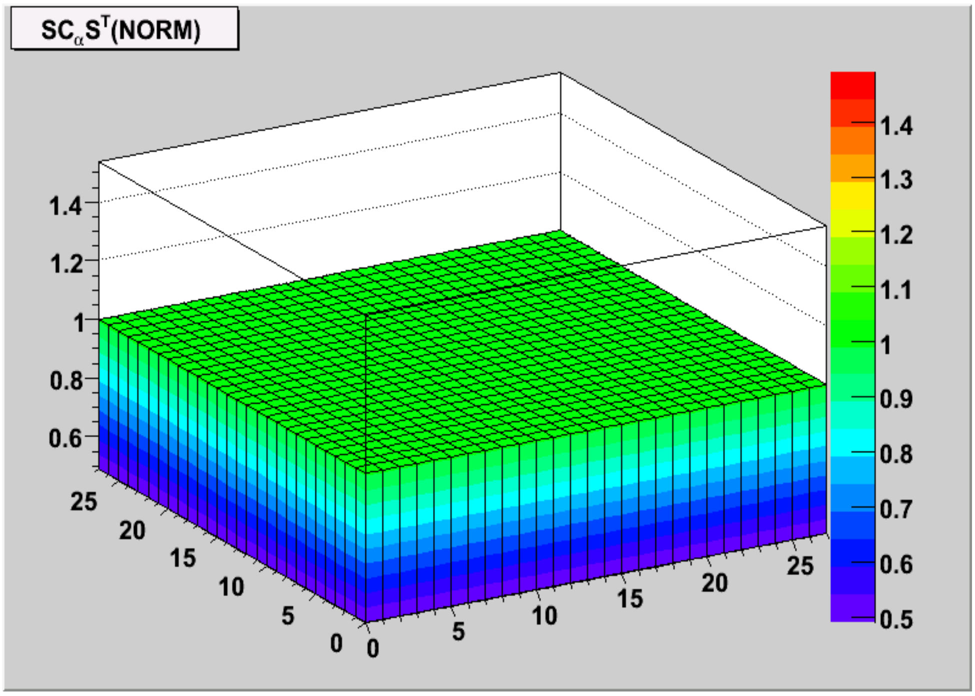

Figure 3.16: Correlation matrix for the computed responses for the three experiments described in Table 3.07.

Resp. No. / Exp. No.	1	2	3	4	5	6	7	8	9
P70031	7.57	6.75	5.96	5.34	5.25	5.18	5.19	4.77	5.25
P70032	7.76	6.88	6.13	5.51	5.44	5.36	5.35	4.90	5.40
P70033	7.82	7.04	6.33	5.64	5.55	5.44	5.47	5.01	5.53

Table 3.09: Relative standard deviations (in %) of computed responses.

The above sensitivities together with the a priori covariance matrices for the measured responses and standard deviation (of 0.11) for K_{loss} were used to compute the value of the consistency indicator. The value thus obtained was $\chi^2 = (29.241/27) = 1.083$, which is very close to 1.0, thereby indicating that the data considered for data assimilation and calibration of K_{loss} is highly consistent overall, free of discrepant values. The denominator (27) in the expression of χ^2 accounts for the number of experimental responses (i.e., 9 pressure drops times 3 benchmarks) used in the assimilation and calibration procedure.

The best-estimate value computed by BEST-EST for the spacer pressure loss coefficient is $K_{loss}^{be} = 1.119$, while its accompanying best-estimate relative standard deviation obtained from Eqs. (3.15) is 1.2%. Reassuringly, the best-estimate value $K_{loss}^{be} = 1.119$ is very close to the recommended value for FLICA4. The use of highly consistent experimental data has resulted in a very strongly reduced, and ultimately very small (1.2%), best estimate relative standard deviation. The best-estimate value $K_{loss}^{be} = 1.119$ will be henceforth used for the spacer pressure loss coefficient for all of the analyses to be presented in subsequent sections of this work.

The results the best estimate response values computed using BEST-EST are indicated by the filled-in (black) markers in Figure 3.13. The initial bias, which has characterized the original un-calibrated responses (computed using K_{loss}=1.1), has been drastically reduced after data assimilation and model calibration; the best estimate responses are much closer to the measured ones. Table 3.10 and Figure 3.14 present the corresponding best-estimate (relative) standard deviations. Since a single model parameter (namely K_{loss}), has been considered for data assimilation and calibration, the normalized (to the corresponding variances) best-estimate correlation matrices for the responses and also the best-estimate correlations for the parameters-responses are all unity (fully correlated). Figure 3.17 highlights the excellent agreement between the best estimate responses and the response-values obtained by re-computations using FLICA4 with the best estimate value $K_{loss}^{be} = 1.119$ for the spacer pressure loss coefficient. This excellent agreement indicates that the simulation model (FLICA4) behaves almost linearly with respect to variations in K_{loss}^{be} .

Resp. No. / Exp. No.	1	2	3	4	5	6	7	8	9
P70031	0.930	0.892	0.738	0.714	0.711	0.714	0.713	0.631	0.703
P70032	0.936	0.893	0.744	0.719	0.718	0.722	0.719	0.637	0.709
P70033	0.942	0.905	0.757	0.732	0.730	0.729	0.731	0.648	0.721

Table 3.10: Best estimate relative (%)-standard deviations for best estimate responses.

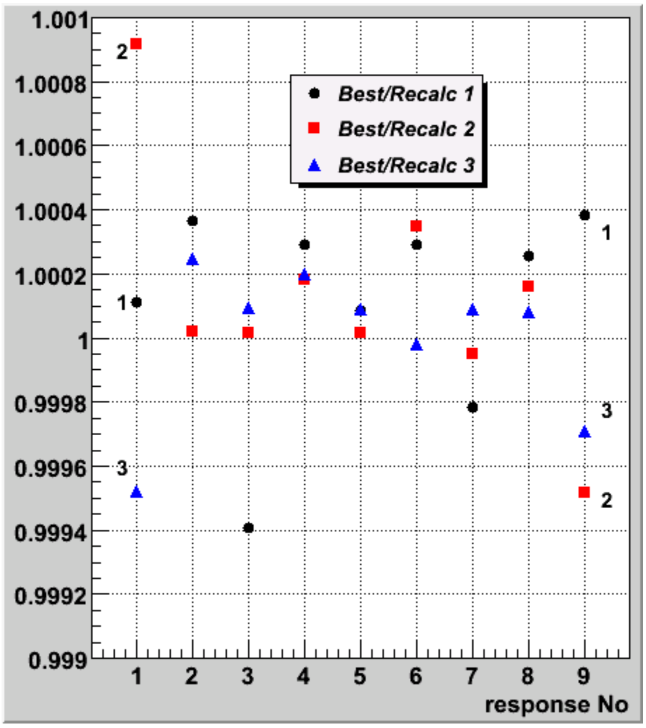

Figure 3.17: Normalized best estimate and recalculated (using $K_{loss}^{be} = 1.119$) pressure drop responses.

3.2.2.3 **Best-Estimate Transient Axial Void Fraction Distributions**

A large variety of transient tests were performed in the BFBT facility in order to measure the transient void fraction distributions as functions of pressure, flow, and power changes representative of operational transients important for reactor safety, namely turbine trip without bypass, one pump trip, re-circulation pump tripped, and malfunction of pressure control system (pressure increase). The void fraction distributions were measured using the X-ray densitometer as indicated in Figure 3.11. This Section will present the results of using the experimental data provided by the "turbine trip without bypass" (TTWB) test number 4102-001~009 in order to calibrate selected model parameters in the one-dimensional version of FLICA4 for obtaining best-estimate predictions from the numerical simulation of the transient axial void fraction distribution for this TTWB-test. The parameters *pressure*, *flow*, and *power* play a primordial role for the envisaged model calibration and will therefore be called "*defining conditions*" for the resulting axial void fraction distributions, in order to distinguish them from other parameters that will be calibrated in FLICA4.

The TTWB transient was simulated with FLICA4, including thermal coupling, using the calibrated value $K_{loss}^{be} = 1.119$ (see previous section). The nominal values of the "defining conditions" (i.e., flow rate, power and outlet pressure) for the TTWB measurements are depicted in Figure 3.18. These "defining conditions" will be calibrated in Section 3.2.2.3.1. Three *system responses* have been considered for data assimilation and calibration, namely the time-dependent cross-sectional (transversal) averaged transient void distributions measured with the X-ray densitometers at three axial elevations: h_1 = (3708 – 978) mm, $h_2 = h_1$ - 1024 mm, $h_3 = h_2$ – 1024 mm (see Fig.3.11). These responses are denoted by R_1, R_2, R_3, respectively, and are depicted in Figure 3.19. Note that the BFBT experimental setup provides experimental information for the TTWB defining conditions (cf., Figure 3.18) and for the system responses (transient void fractions depicted in Figure 3.19) at every 0.02 seconds. As will be discussed in the sequel, such extremely narrow time intervals will not be necessary for the purpose of data assimilation and model calibration; a subset of these measurements will provide sufficiently accurate experimental information for this purpose.

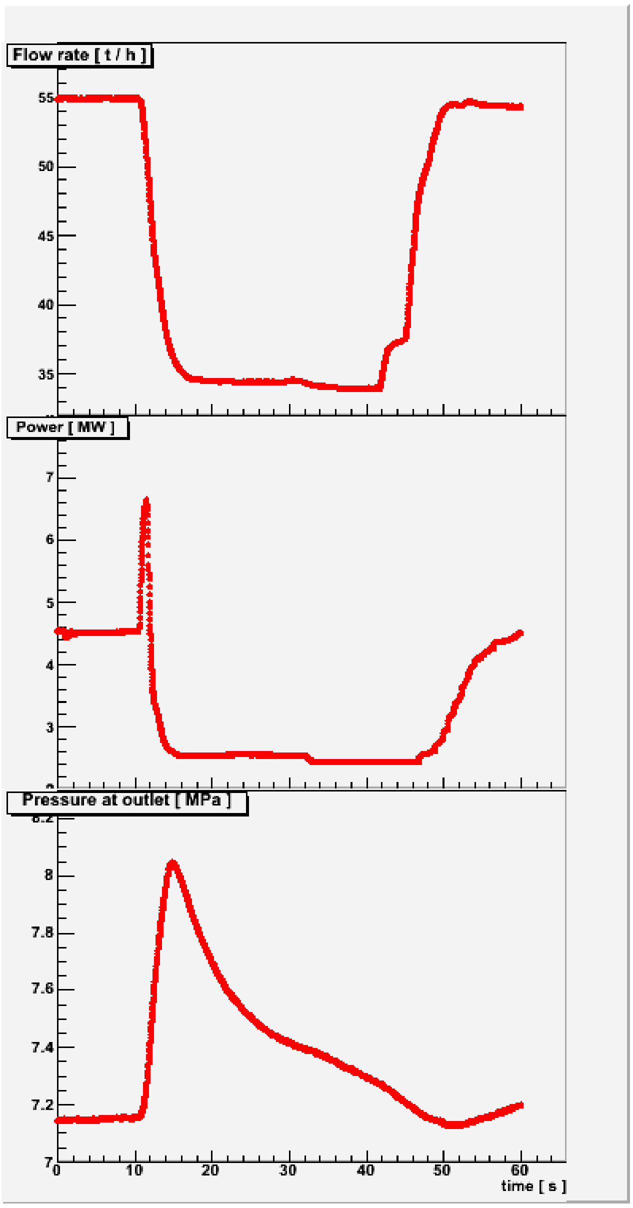

Figure 3.18: Defining conditions (flow rate, power, pressure at outlet) for the TTWB test.

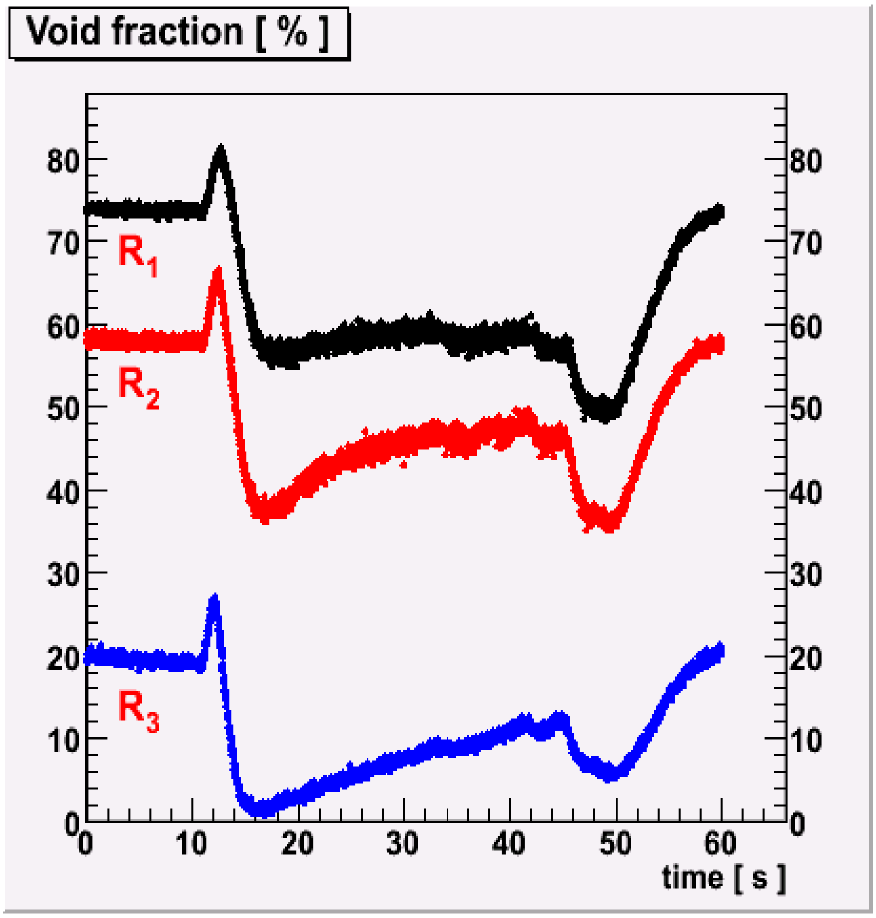

Figure 3.19: Measured void fraction responses for the TTWB test 4102-001~009.

In the forgoing, the outlet pressure, flow rate, and power were called "defining conditions" because these quantities play a key role in defining the transient TTWB test number 4102-001~009. As depicted in Figure 3.18, these defining conditions undergo large variations during the TTWB test, which greatly influence the transient axial void fraction distributions. However, these influences have a relatively local effect, lasting for less than 8 seconds after the instant at which some defining condition (i.e., outlet pressure, flow rate or power) might be perturbed. This localized effect of perturbation is clearly indicated by the typical sensitivities depicted in Figures 3.20 through 3.22. These sensitivities were computed for responses considered at every 0.1 seconds, thus resulting in 500 time nodes per response, and as depicted, they decay very rapidly away from their maximum which corresponds to the instant at which the perturbation was effected in the respective defining condition. The fact that the effect of perturbations in the defining condition is so localized, for all three responses and all three defining conditions, has greatly facilitated the computations of the time-dependent sensitivity matrix for the transient data assimilation process. In particular, this feature has made it possible to neglect the parameter sensitivities for the last 8 seconds of the TTWB transient, so that the number of parameters for the data assimilation/model calibration procedure was limited to 420 per defining condition; hence, the total number of parameters considered for data calibration is 3 x420 = 1260.

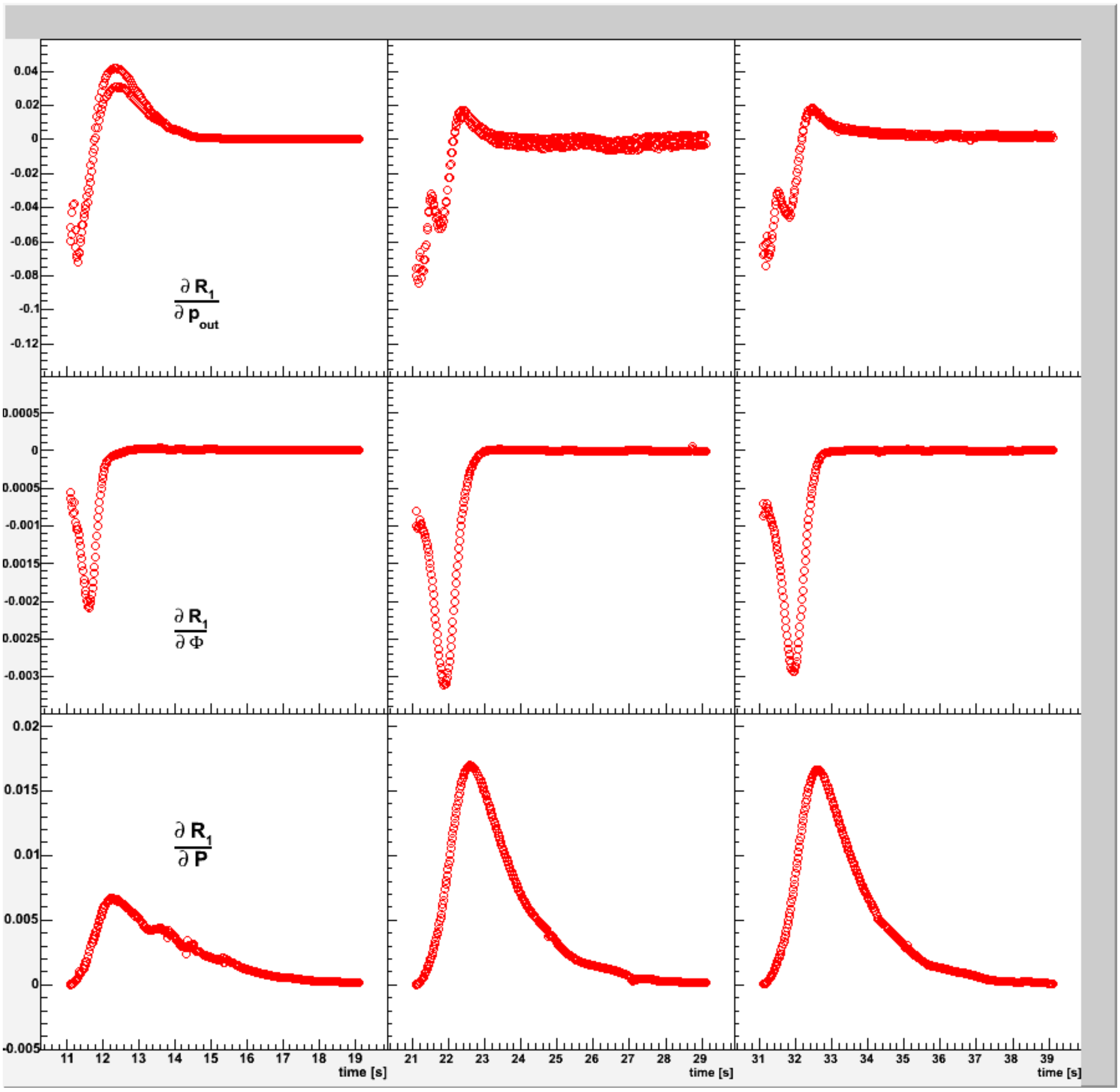

Figure 3.20: Typical time-dependent absolute sensitivities of the void fraction response R_1 (measured in % of void fraction) to outlet pressure (p_{out}), flow rate (Φ), power (P). Parameter perturbations effected at 11.1 s (1st column), 21.1s (2nd column), and 31.1s (3rd column).

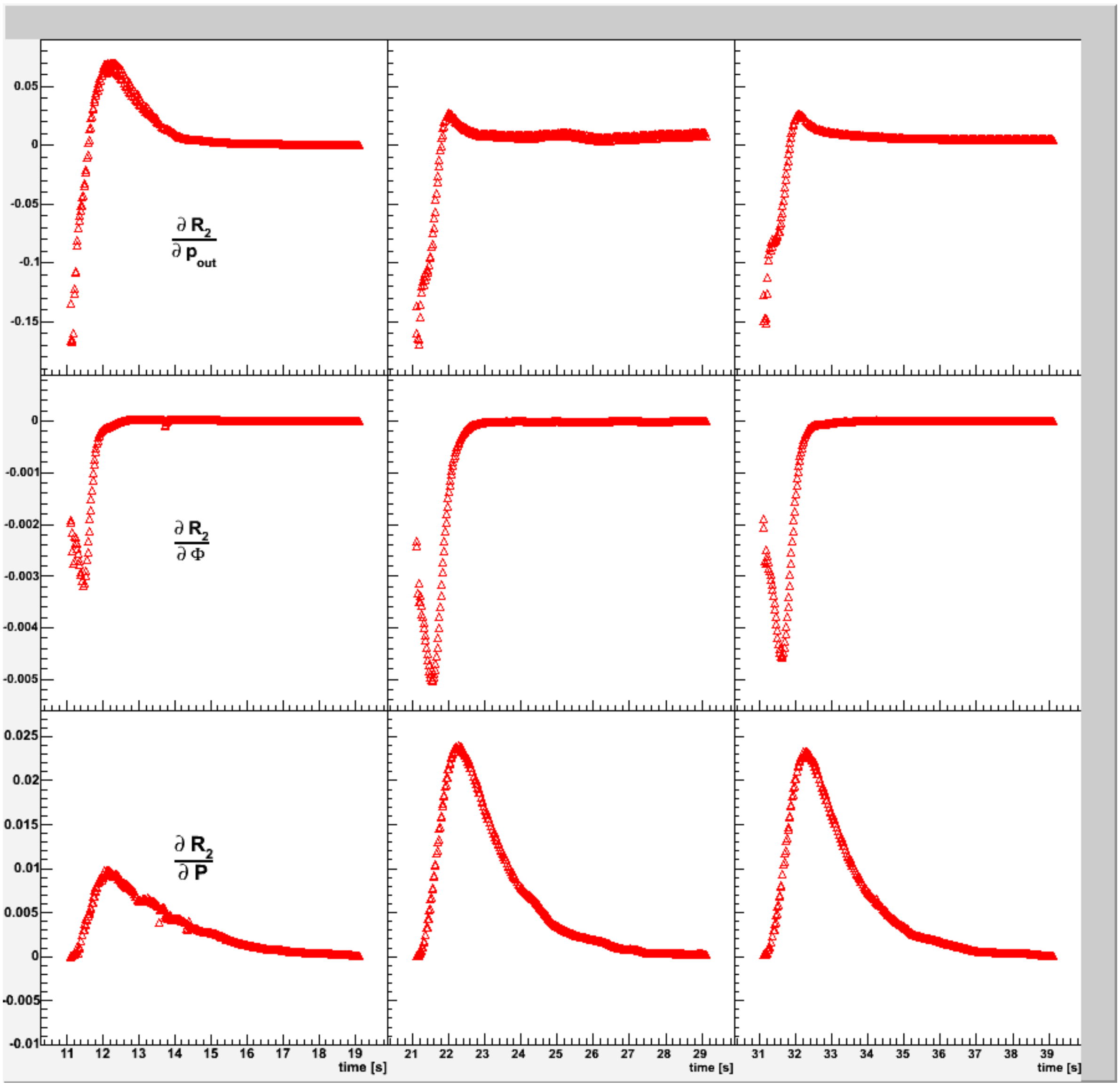

Figure 3.21: Typical time-dependent absolute sensitivities of the void fraction response R_2 (measured in % of void fraction) to outlet pressure (p_{out}), flow rate (Φ), power (P). Parameter perturbations effected at 11.1 s (1stcolumn), 21.1s (2ndcolumn), and 31.1s (3rdcolumn).

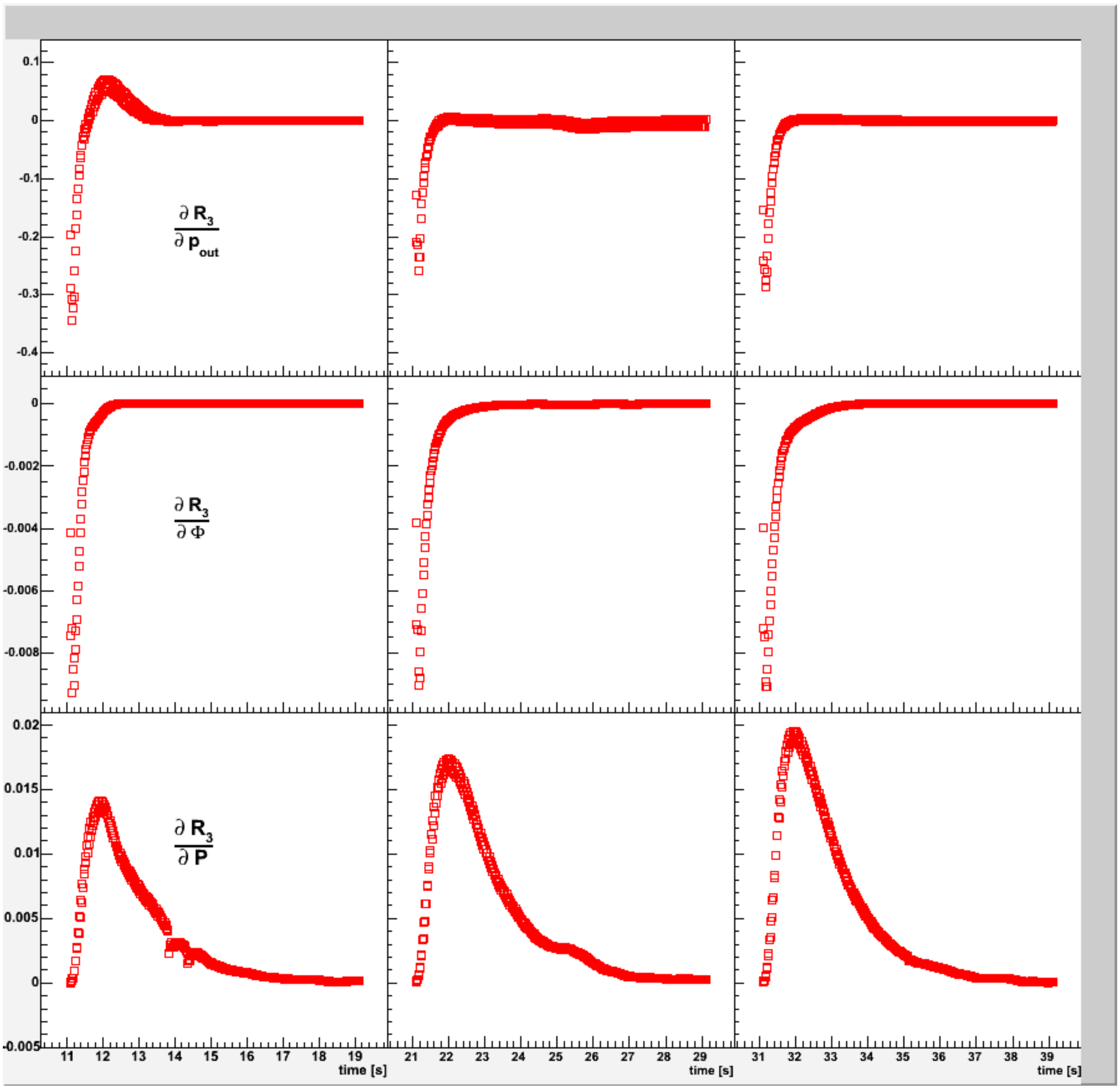

Figure 3.22: Typical time-dependent absolute sensitivities of the void fraction response R_3 (measured in % of void fraction) to outlet pressure (p_{out}), flow rate (Φ), power (P). Parameter perturbations effected at 11.1 s (1stcolumn), 21.1s (2ndcolumn), and 31.1s (3rdcolumn).

As in previous sections, the BEST-EST module has been used for implementing the data assimilation/ model calibration procedure of Section 3.1 for calibrating the TTWB “defining conditions”. Furthermore, a 4% nominal relative standard deviation was considered for the flow rate, while the nominal relative standard deviation for the outlet pressure was taken as 2%. The standard deviations for the void fraction distributions were taken to be 3.5%, independent of time and space.

As in the previous Section, the data assimilation procedure was applied individually to each of the void fraction responses R_1, R_2, and R_3. The values of the corresponding consistency indicators were computed with BEST-EST as $\chi_1^2 = 473.39 \div 500 = 0.95,$ $\chi_2^2 = 243.35 \div 500 = 0.49,$ and $\chi_3^2 = 17.52 \div 500 = 3.5 \times 10^{-3}$, respectively. The black lines in Figure 3.23 depict the best estimate responses, which fall, as expected, between the originally measured and computed values, being closer to the experimental values. The accompanying best estimate error bands for the three individually calibrated responses are depicted in Figure 3.24, which underscores the significant uncertainty reduction after data assimilation and model calibration. Of course, there is a corresponding set of best estimate "defining conditions" for each of the three responses, which allows for an excellent agreement between the best-estimate predictions and the individual transient measurements. Although BEST-EST calibrates the defining conditions parameters only for 420 time steps (since the sensitivities for the remaining time-steps are practically zero), the information is assimilated for the full range of 500 time steps (corresponding to the time interval 10-60 seconds) displayed in Figure 3.23. Figures 3.25 through 3.27 show that the best estimate defining conditions agree well with the corresponding original experiments. Note that the best estimate nominal values presented in these figures were obtained by using only the first 420 time steps in BEST-EST, since the sensitivities for the remaining time steps are negligible due to their "localization" features, as mentioned in the foregoing. As Figures 3.25 through 3.27 indicate, the outlet pressure is most affected by the data assimilation process; this is due to the high sensitivities of the void fraction distributions to the TTWB outlet pressure. Typical best-estimate correlations, after data assimilation, among parameters and responses are displayed in Fig. 3.28, showing that the non-zero values are clustered along the main diagonal of the respective matrix. The corresponding correlations for the other two responses are not displayed since they behave similarly.

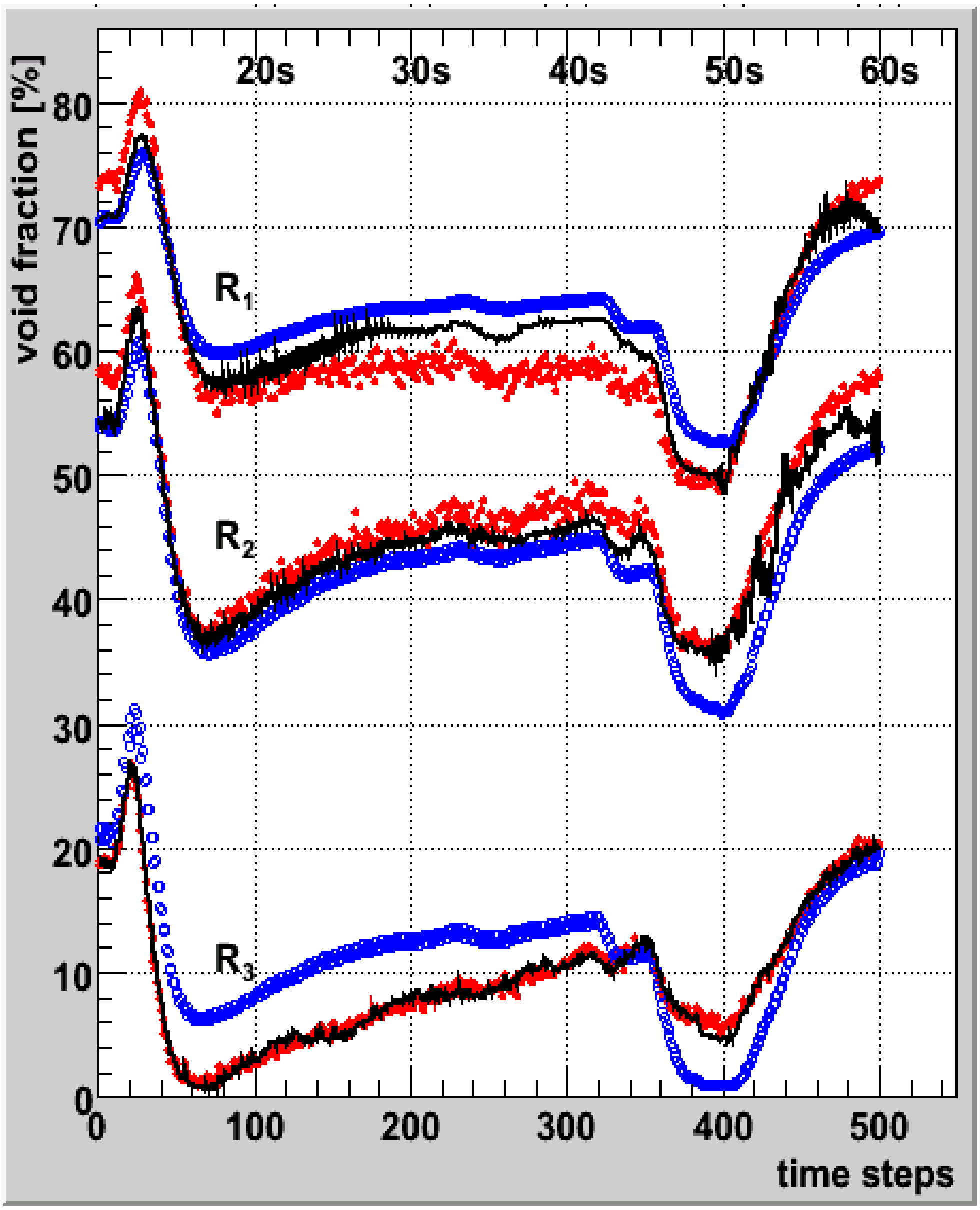

Figure 3.23: Experimental (red), simulated (blue) and best estimate (black) void fraction distributions after data assimilation and individual calibration of responses.

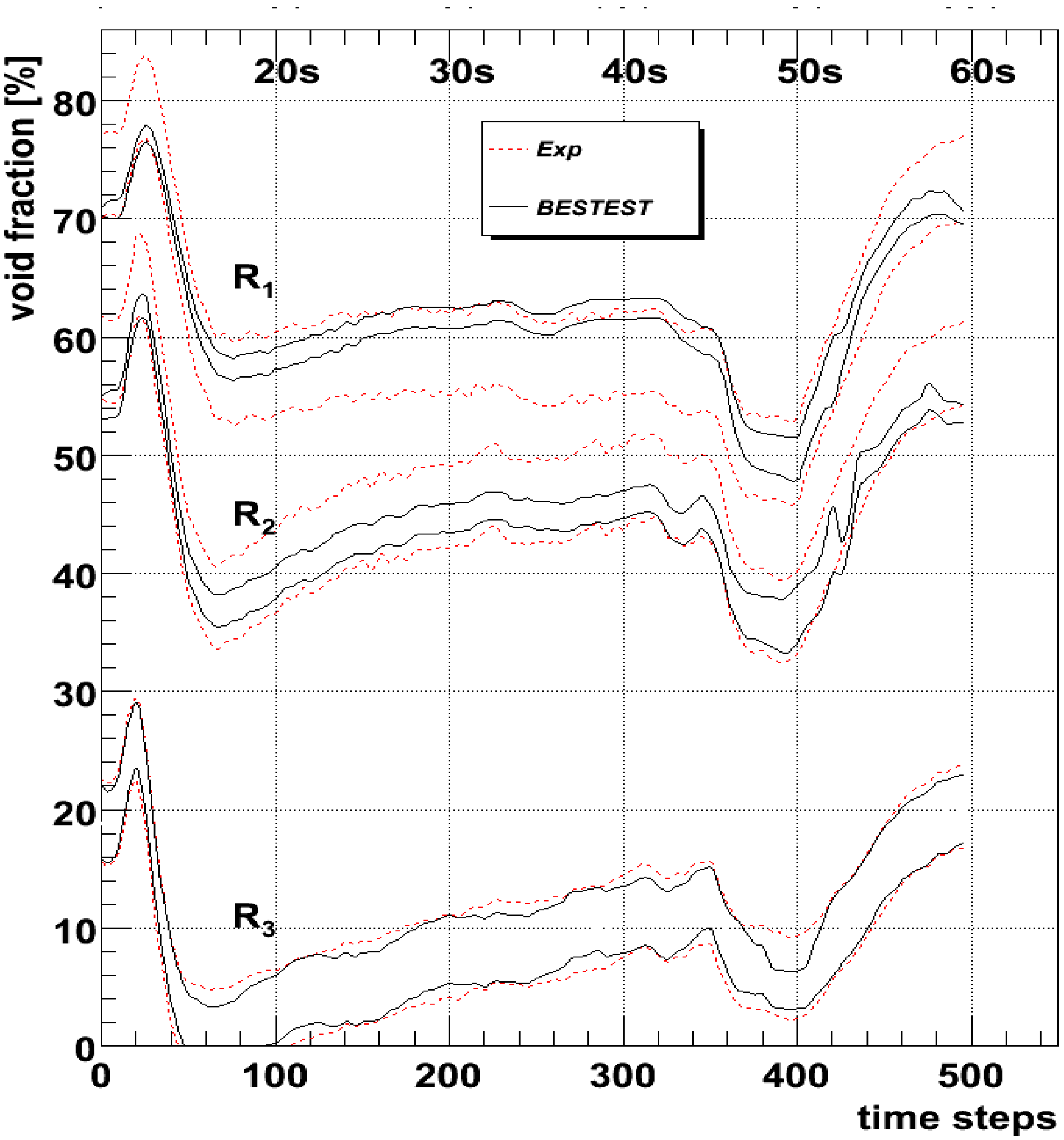

Figure 3.24: Error bands for experimental and best estimate void fraction distributions after data assimilation and individual calibration of responses.

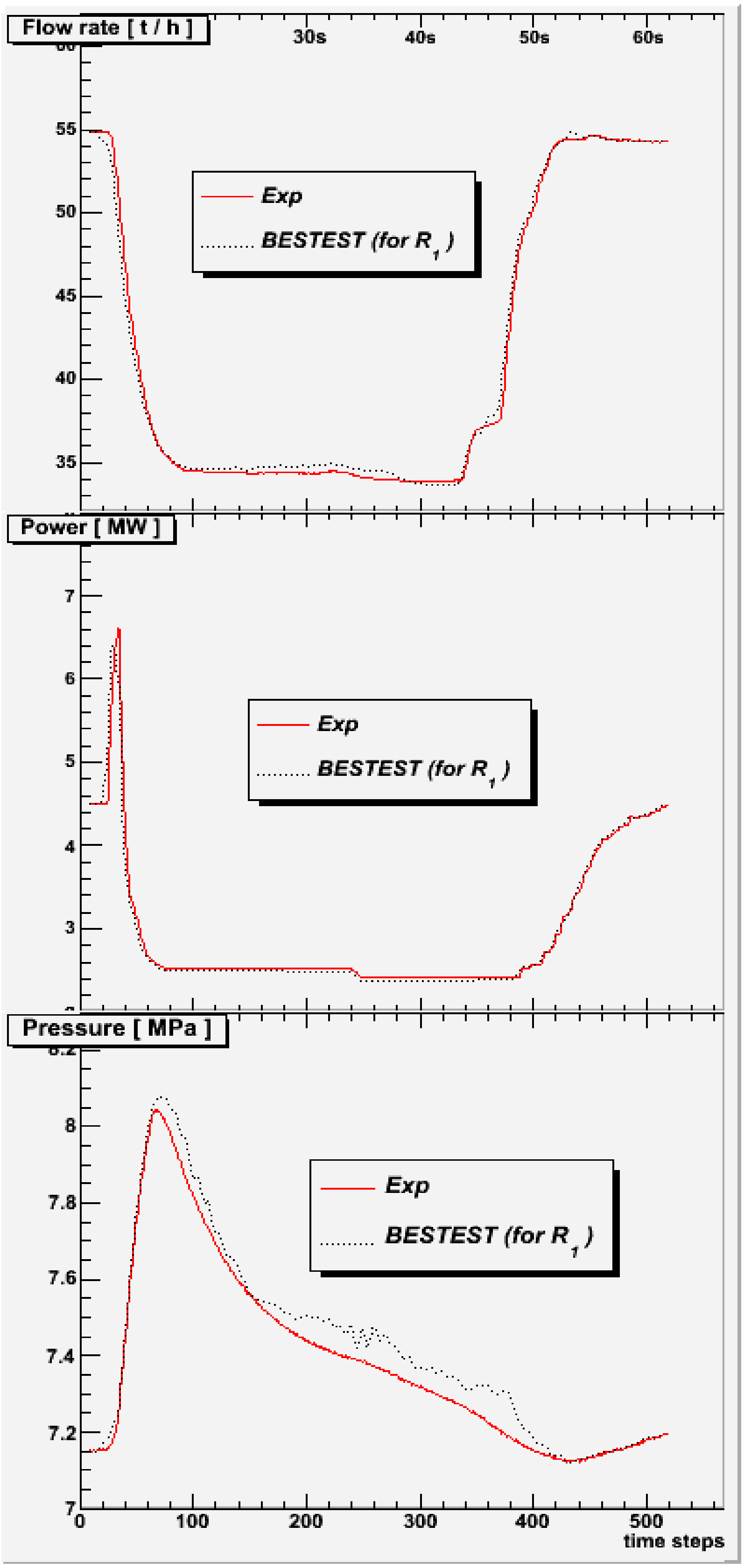

Figure 3.25: Nominal and best estimate TTWB defining conditions assimilating only the experimental data provided by R_1.

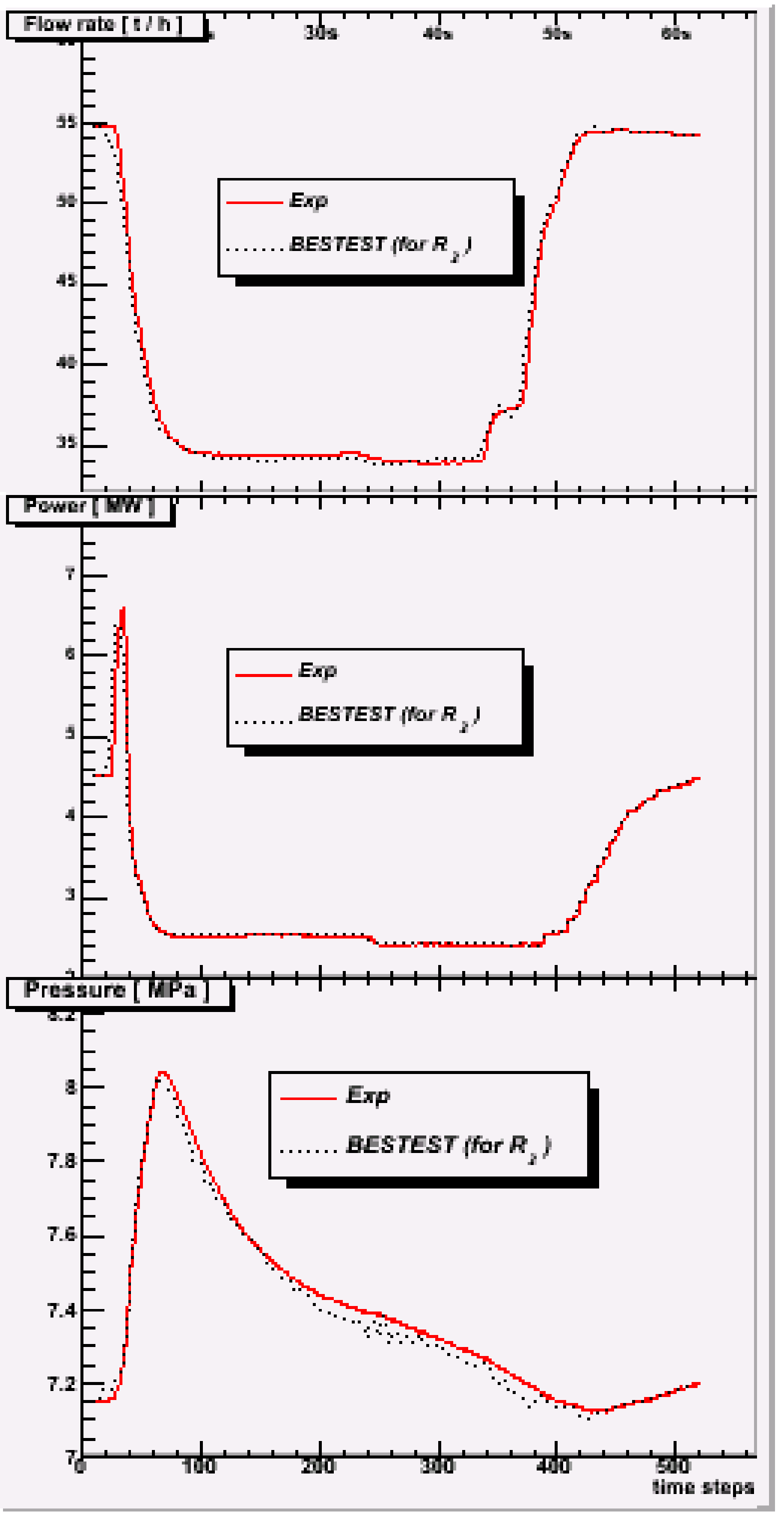

Figure 3.26: Nominal and best estimate TTWB defining conditions assimilating only the experimental data provided by R_2.

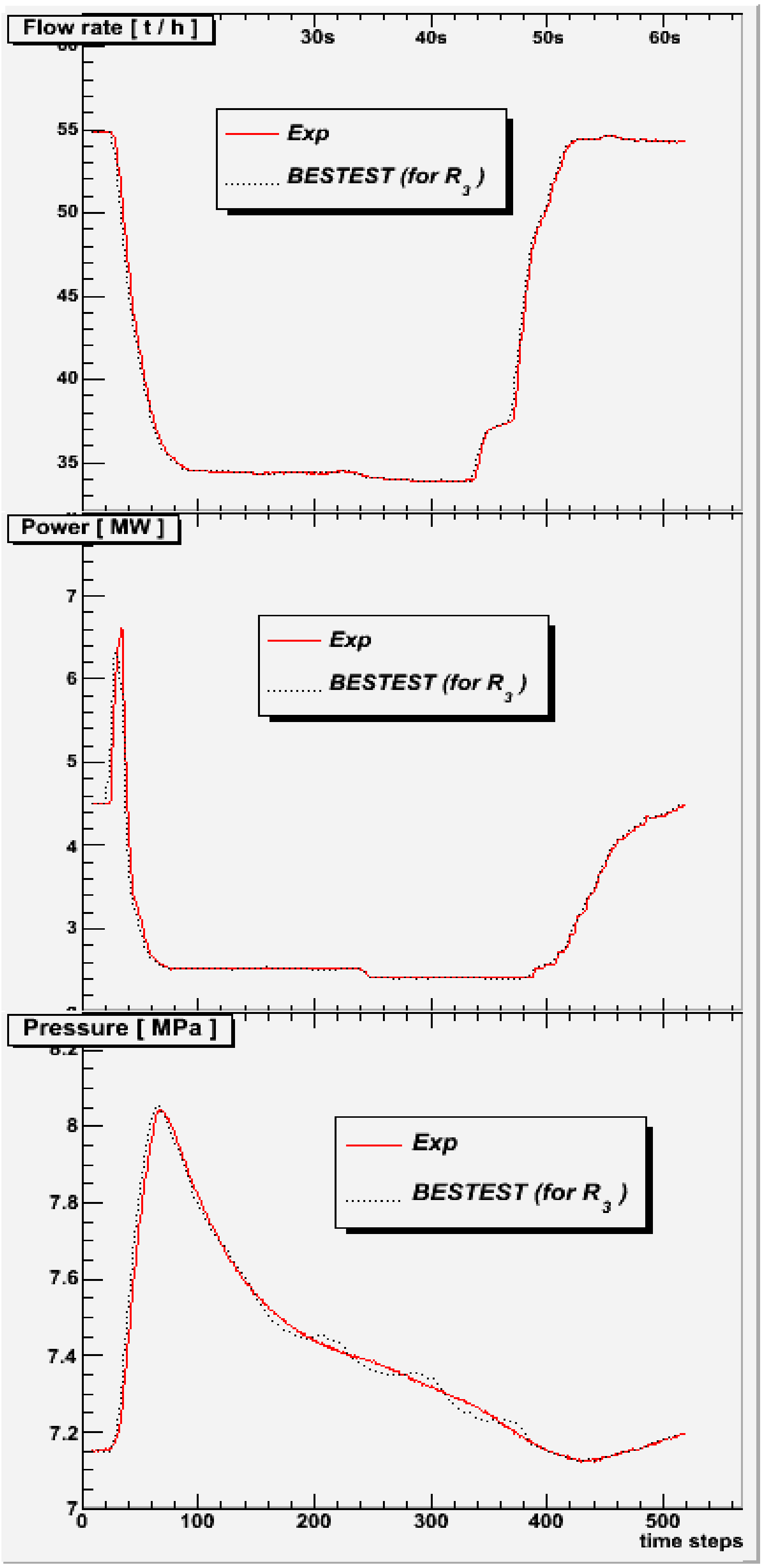

Figure 3.27: Nominal and best estimate TTWB defining conditions assimilating only the experimental data provided by R_3.

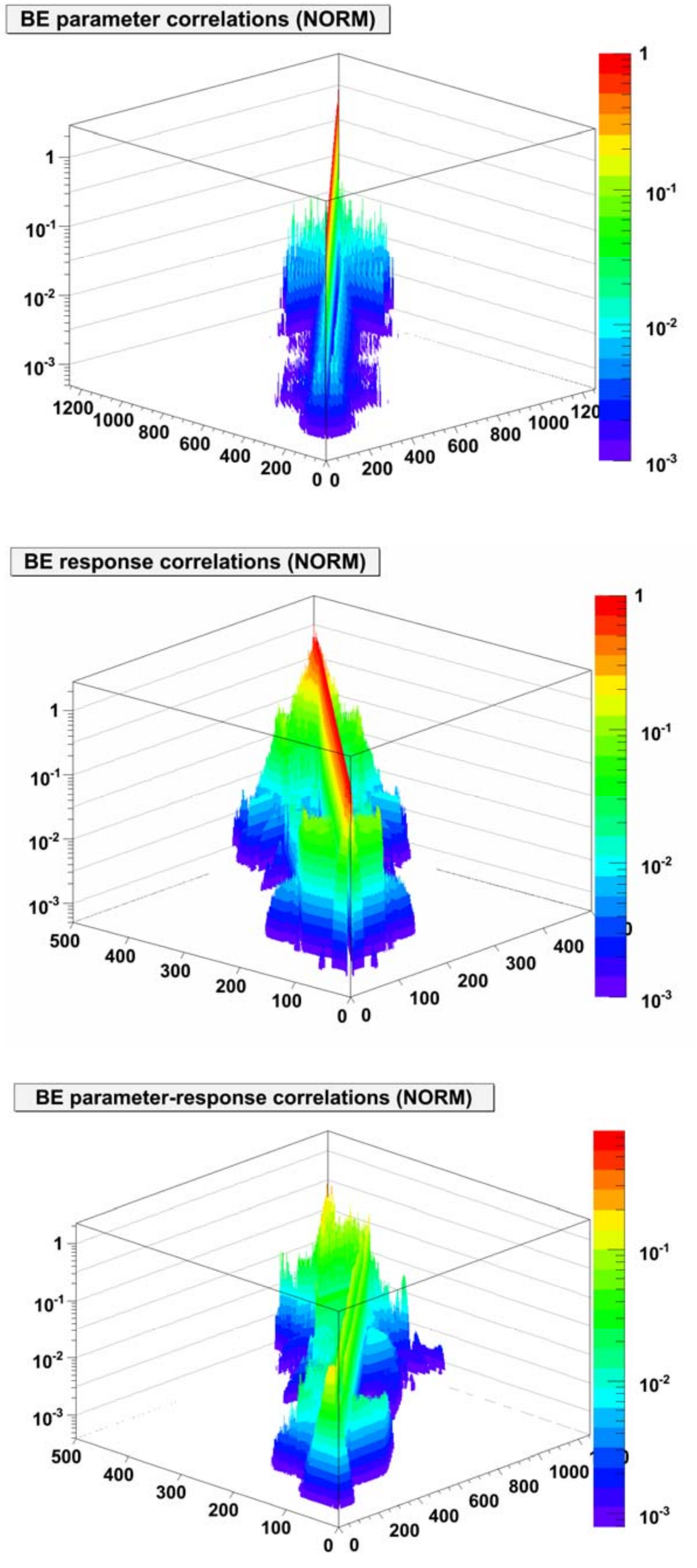

Figure 3.28: Normalized best estimate correlation matrices for R_1

3.2.2.4 Best-Estimate Two-Dimensional Transverse Void Fraction Distributions

Stationary two-dimensional void fraction distributions have been measured using the X-ray CT scanner depicted above the X-ray densitometers positions in Figure 3.11 Such measurements can be used to calibrate the three-dimensional capabilities of FLICA4. The particular measurement selected for data assimilation in this Section is depicted in Figure 3.29

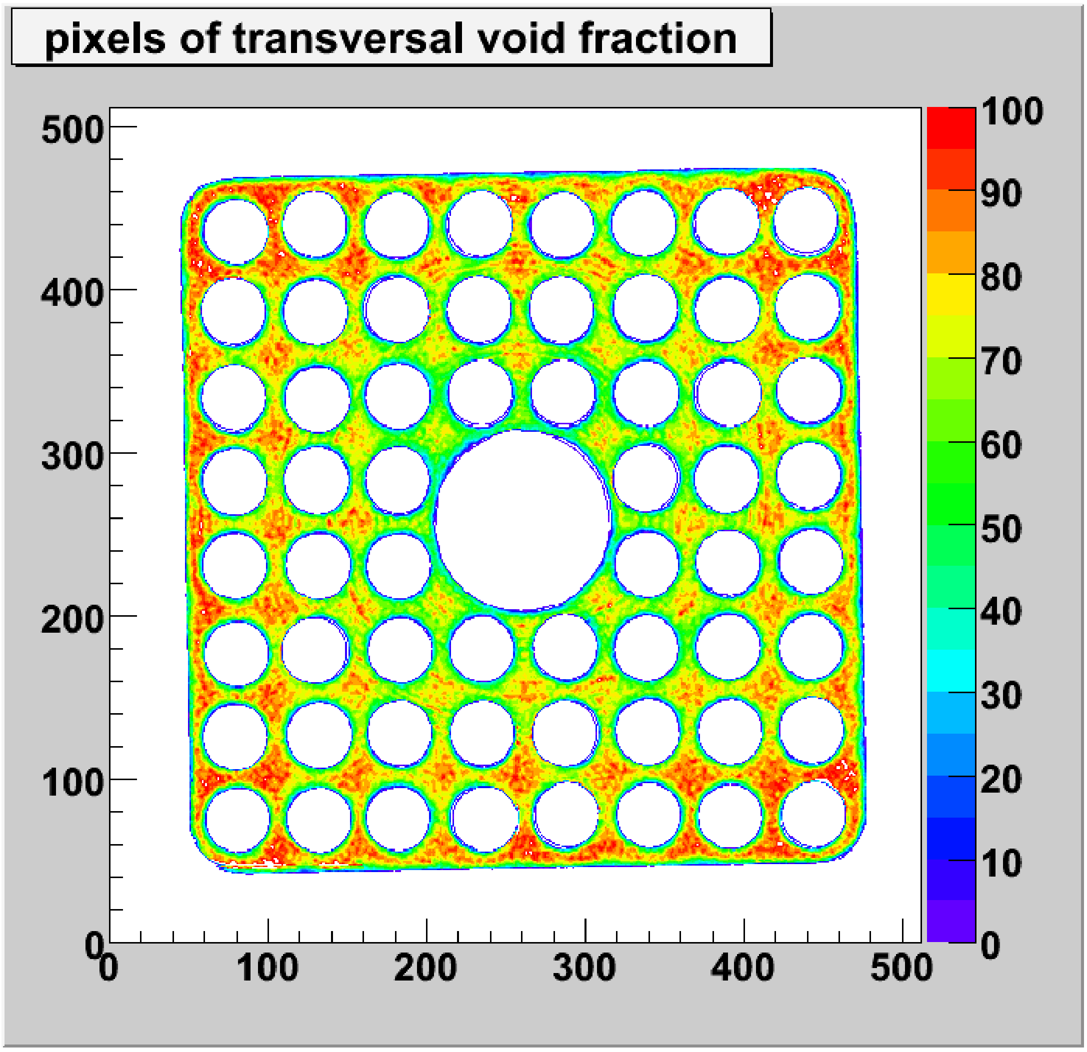

Figure 3.29: Two-dimensional pixels of transversal void fraction distribution measured by the X-ray CT scanner.

The transverse void fractions at “pixel” level shown in Figure 3.29 were collapsed by arithmetical averaging into sub-channel void fraction distributions as shown in Figure 3.30, in order to compare them with three-dimensional calculations FLICA4 performed with cross-flows at sub-channel level. For the FLICA4 computations, the 64 sub-channels depicted in Figure 3.29 were defined by the 7 vertical and 7 horizontal lines which are equidistant to the columns and rows of fuel rods (depicted by the 60 white spots in the Figure 3.29). The outside borders (shown in white in Figure 3.29) of the mock-up assembly enclose the outer 28 sub-channels. The results of the three-dimensional FLICA4 computations (performed with cross-flows at sub-channel level) of the void fraction distribution corresponding to the measurement displayed in Figure 3.30 are shown in Figure 3.31, in “scalar map” and, respectively, “iso-surfaces” representations. Corresponding to the three-dimensional results displayed in this figure, the computed transverse void fraction distribution has nominal values as shown in Figure 3.32. The percentage difference between the experimental and computational results shown in Figure 3.31 and 3.32, respectively, are displayed in Figure 3.33, in relative percentages.

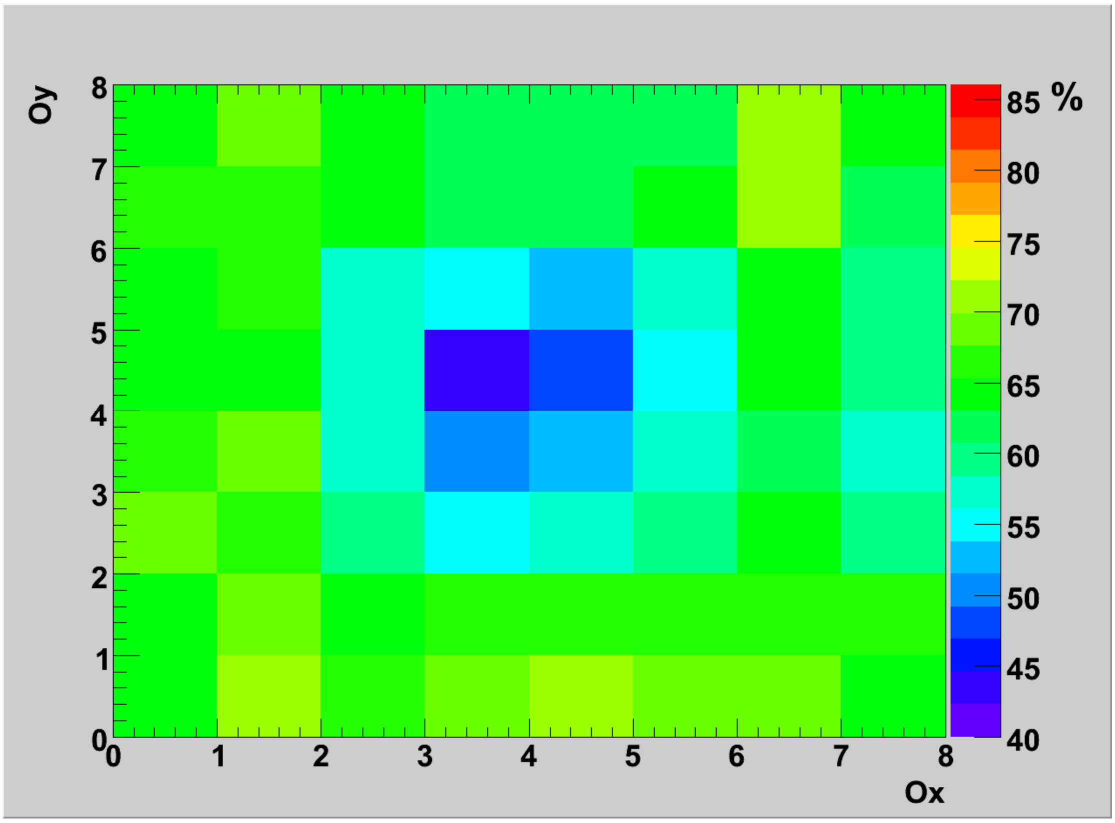

Figure 3.30 : Experimental transversal void fraction distributions

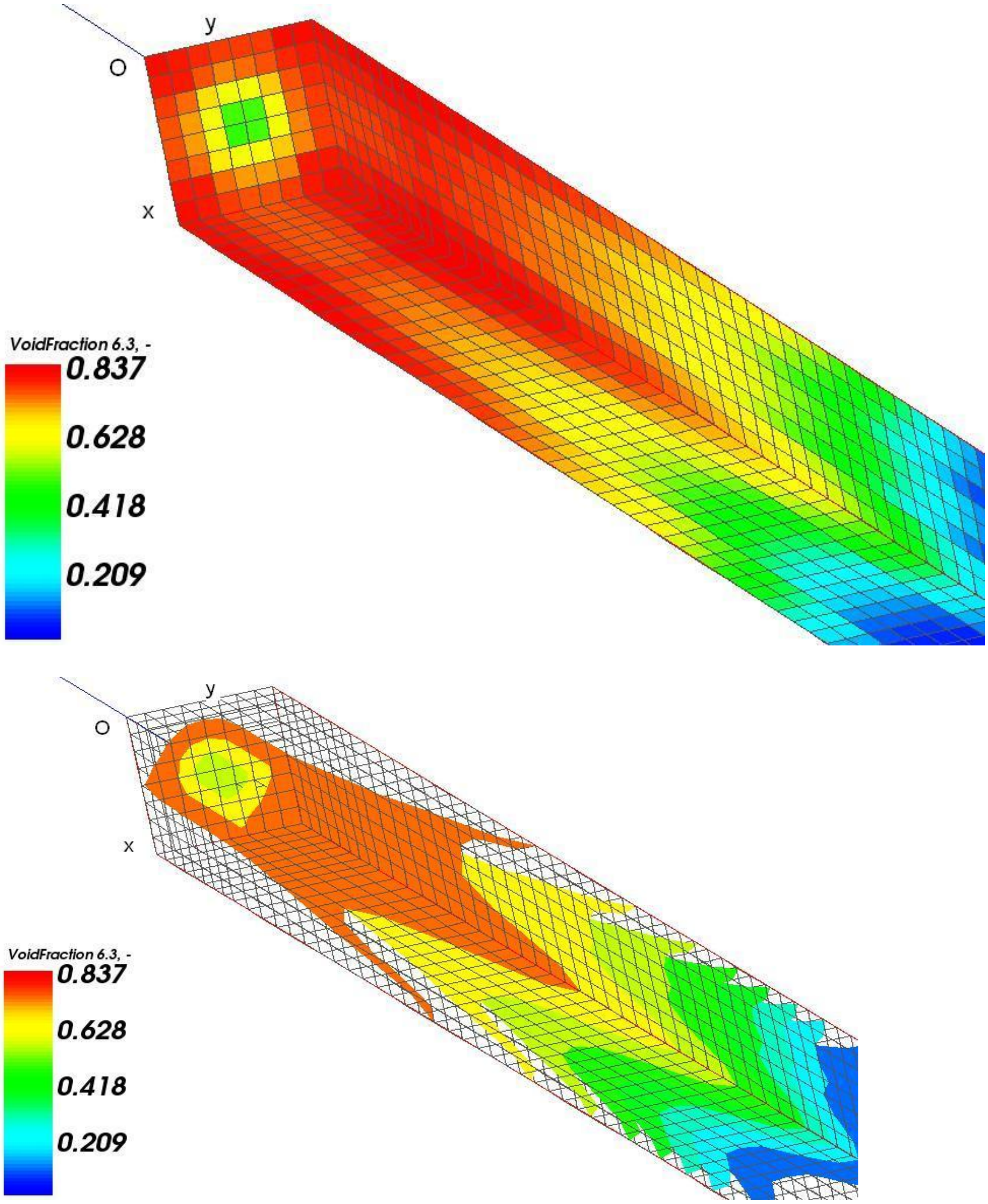

Figure 3.31: 3D transversal void fraction distributions computed with FLICA4. Top view: “Scalar Map” representation; Bottom view: “Iso-surfaces”.

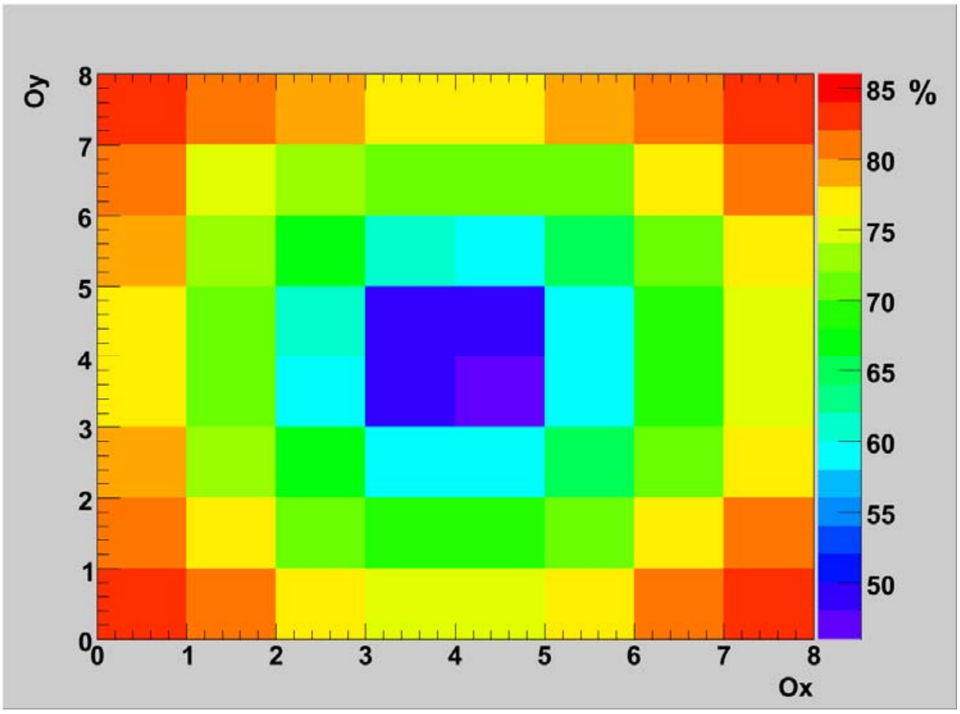

Figure 3.32: Computed nominal values of the transversal void fraction distribution.

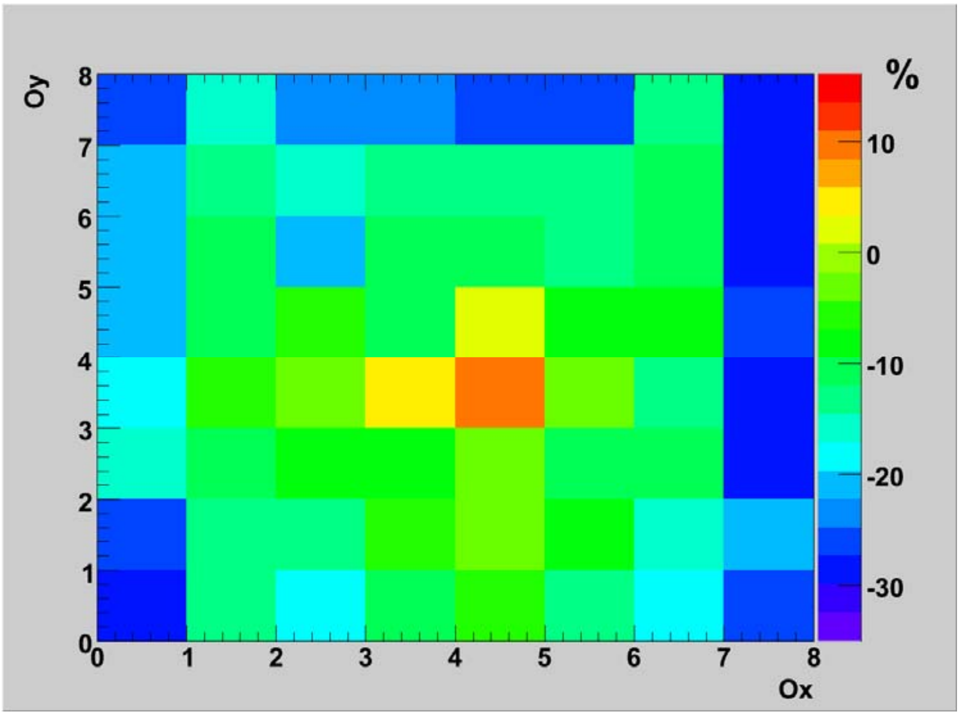

Figure 3.33: Percentage comparison “(Exp-Sim)/Exp” between experimental and computed transversal void fraction distributions.

Table 3.11 lists the nominal values and the accompanying relative standard deviations of the FLICA4-parameters that will be considered for calibration in conjunction with the transversal void fraction distribution measurements. The first four parameters in this table are the "defining conditions" for the measurement under consideration while the fifth parameter in Table 3.11 significantly impacts the lateral void fraction distribution

Parameters	Nominal Values and Standard Deviations
1. Outlet pressure [MPa]	7.19±3%
2. Flow rate [t/h]]	54.80±3%
3. Inlet subcooling [KJ/Kg] (α_1)	128.1±3%
4. Power [MW]	4.68±3%
5. Coefficient for turbulent mixing (BT)	1.00±3%

Table 3.11: Nominal values of system parameters for transversal void fraction calibration.

Figure 3.34 displays sensitivities of the 64 sub-channel void fractions, considered as responses, to the 5 parameters listed in Table 3.11, highlighting, in particular, the large relative sensitivity of the responses to the coefficient for turbulent mixing.

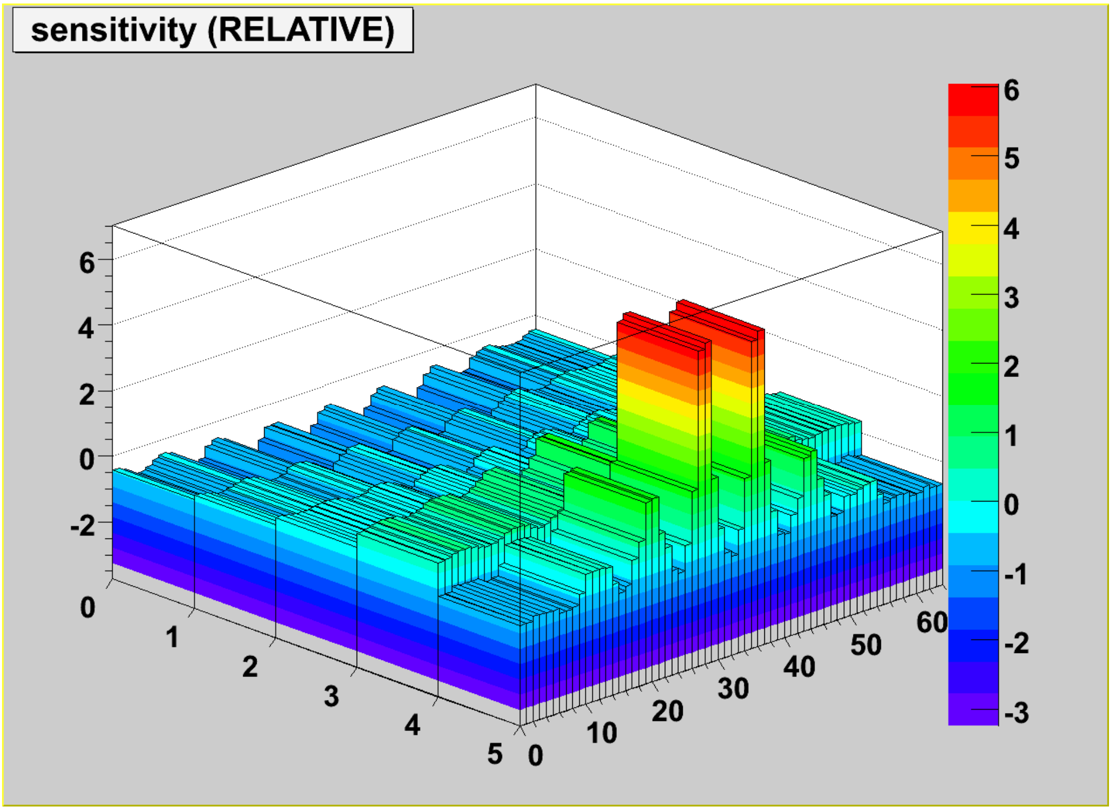

Figure 3.34: Relative sensitivities of the 64 sub-channel void fraction responses to the 5 system parameters listed in Table 3.11.

The 64 experimental sub-channel void fraction responses were assumed to be uncorrelated, with relative standard deviations taken to be 7% for each of the sub-channels. This standard deviation was derived based on the respective pixel-data. Even for this relatively large uncertainty, the consistency indicator was computed by BEST-EST as $\chi^2 = 74.54 \div 64 = 1.16$, indicating consistency among measurements and FLICA4 parameters. The best estimate relative standard deviations of the calibrated parameters are displayed in the 3rd column of Table 3.12, which shows, in particular, that the turbulent mixing coefficient (5th parameter) has undergone the largest uncertainty reduction, as would be expected in view of the (largest) corresponding sensitivity. Figure 3.35 displays the normalized best estimate parameter and response correlations, respectively, produced by BEST-EST following the assimilation procedure. Both matrices display non-zero off-diagonal elements, with particularly strong correlations induced by the assimilation and calibration procedure among the calibrated responses. Figure 3.36 presents the comparison (in percentages) between experimental and best estimate calibrated responses, while Figure 3.37 presents the (best estimate) reduced standard deviations for the calibrated transversal void fraction distributions. The calibrated responses are considerably better balanced with respect to 0.0 than the un-calibrated ones (cf., Figure 3.33), before data assimilation.

Parameters	Nominal Values	BESTEST Values
1. Outlet pressure [MPa]	7.19±3%	7.72±1.86%
2. Flow rate [t/h]]	54.80±3%	57.55±2.58%
3. Inlet subcooling [KJ/Kg] (α_1)	128.1±3%	129.88±2.90%
4. Power [MW]	4.68±3%	4.41±2.85%
5. Coefficient for turbulent mixing (BT)	1.00±3%	1.08±0.63%

Table 3.12: Best estimate nominal values and reduced uncertainties for the calibrated FLICA4 parameters.

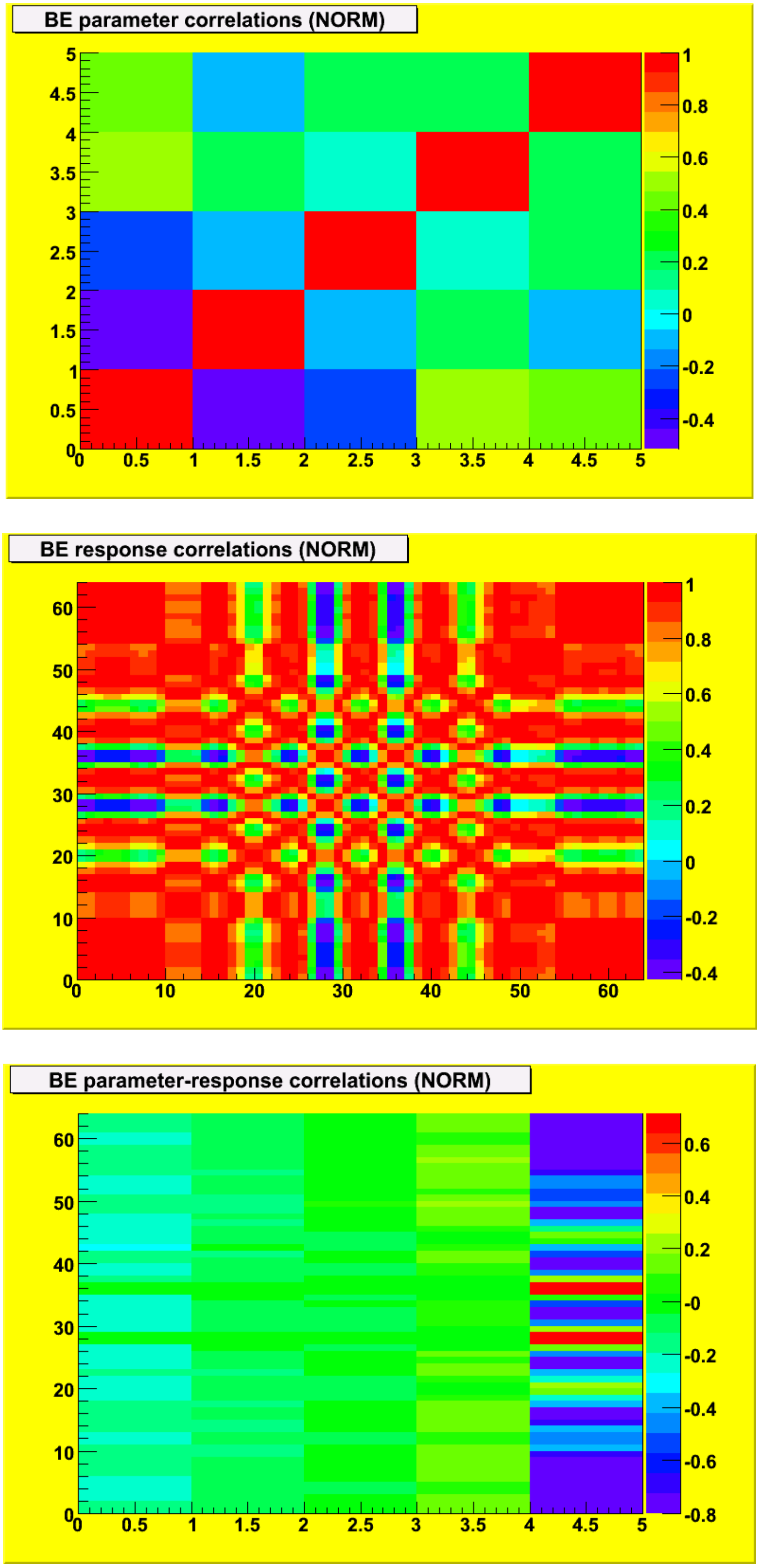

Figure 3.35: Normalized best estimate correlations for parameters (top) and responses (bottom).

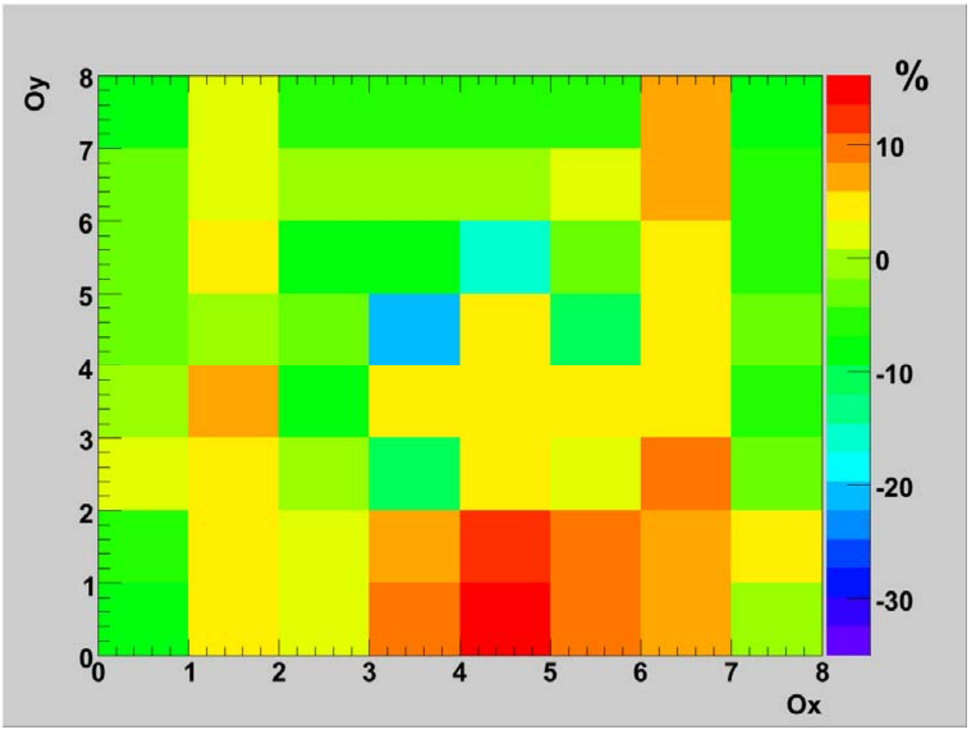

Figure 3.36: Comparison between experimental and BESTEST transversal void fraction responses, 100% (Exp-Best) /Best.

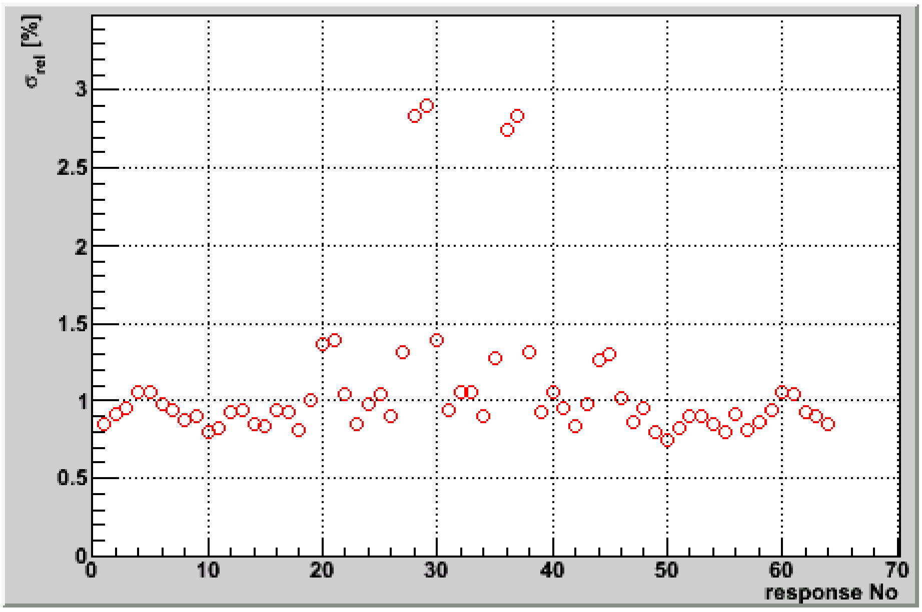

Figure 3.37: Relative standard deviations of the best-estimated transversal void fraction responses.

4 Summary and Conclusions

This work has presented representative applications of a general mathematical framework for simultaneously calibrating model parameters and responses through the assimilation of experimental data, leading to "best-estimate" values with reduced uncertainties for both parameters and responses in a generic time-dependent system. This mathematical framework provides an indication of the agreement between the computed and experimentally measured responses while performing:

(i) Simultaneous calibration of all parameters and responses;
(ii) Treatment of systems involving correlated parameters and responses;
(iii) Simultaneous calibration over all time intervals.

The salient features of the above methodology have been highlighted be presenting a time-independent paradigm neutron diffusion problem and, respectively, a time-dependent radioactive decay problem. These problems have clearly shown that the assimilation of consistent experimental information substantially reduce the uncertainties in the best estimate predictions for both model parameters and responses. The last section of this work has presented, in premiere, a large-scale application of assimilating experimental data from the OECD/NRC BWR Full-Size Fine-Mesh Bundle Tests (BFBT) benchmarks for the calibration of representative model parameters in the three-dimensional thermal-hydraulics code FLICA4, which is routinely used for the analysis and design of light-water reactors (LWR). The BFBT benchmarks were specifically designed by NUPEC to enable a systematic comparison between full-scale experimental data and predictions of numerical simulation models. The BFBT experiments are particularly well suited for quantifying uncertainties in the prediction of detailed sub-channel void fraction distributions and critical powers. In this work, the BFBT measurements have been used for the calibration of model parameters in the thermal-hydraulics code FLICA4, for the following benchmark measurements: (i) pressure drops (steady one-dimensional simulations); (ii) axial void fractions distributions (transient one-dimensional simulations); and (iii) transversal void fraction distributions (steady three-dimensional simulations, at sub-channel level with cross-flows). By calibrating representative FLICA4-parameters, this work has shown that this methodology can be successfully used for reducing systematically uncertainties in large-scale reactor core thermal-hydraulics codes using the BFBT benchmark-grade experiments. Further research is planned towards the consideration of multi-physics code systems comprising coupled thermal-hydraulics and reactor physics numerical simulation tools.

The estimation of the validation domain of the physics underlying the models of interest requires estimation of contours of constant uncertainty in the high-dimensional space that characterizes the application of interest. In practice, this involves the identification of areas where the predictive estimation of uncertainty meets specified requirements for the performance, reliability, or safety of the system of interest. The state-of-the-art in estimation of the validation domain is very early in both the conceptual and mathematical development. Developing predictive experimentally validated "best-estimate" numerical models is particularly important for designing new technologies and facilities based on novel processes, while striving to avoid, as much as possible, the costly and lengthy procedures of building representative mock-up experiments which might confirm—but would not necessarily explain— the predictions of simulation tools. For example, the performance of fuels and materials, in particular fuel irradiation behavior, is dominated by the coupled effects of several phenomena and relies uniquely on very expensive and time-consuming confirmatory mockup experiments (e.g., multiyear irradiations), with little or no predictive capability; improvements in this regard have very high potential payoff. Also, systems-level analysis tools are, by nature, primarily predictive because they are evaluating systems that typically do not exist. When coupled phenomena occur, in particular for safety analyses, validation has been restricted to either mockup or component-level experimental comparison, with little predictive capability. The best-estimate calibrated values for model parameters obtained through the application of the mathematical framework presented in this work can also be used to estimate quantitatively the validation domain of the model under consideration, by computing contours of constant best-estimate uncertainties in the high-dimensional parameter-space. The best-estimate calibrated values an also be used to perform "model extrapolation", by predicting uncertainties in new environments or conditions of interest. Extrapolation of large-scale models would address both untested parts of the parameter space and higher levels of system complexity in the validation hierarchy.

The explicit formulas used in this work are based on the linearized relationship between responses and parameters that customarily underlies the "propagation of moments" method, without explicitly considering nonlinearities and modeling errors. Nevertheless, neither of these limitations is as severe as it may appear at first glance, since: (i) modeling errors can be treated in a manner similar to parameter uncertainties by including the discretization intervals in the vector of model parameters, as shown by Cacuci (2003); and (ii) nonlinear relations between computed responses and model parameters can be treated iteratively. Thus, all of the major formulas used in this work are to be considered as the first step in an iterative procedure which starts with the known nominal values of the quantities involved. The subsequent step of such an iterative procedure would be to use the formulas for the best-estimate mean values and covariances for the parameters and responses presented in Section 1 as the "prior information", and compute the new ("second-generation") best-estimate quantities by using once again formally similar formulas. This iterative procedure would be repeated until the best-estimated values would not change any longer, thereby indicating convergence of the nonlinear iterative procedure.

Computationally, the most intensive aspect of the above-mentioned methodology presented in this work is the computation of the sensitivities of responses to model parameters, which play a crucial role as weighting functions in all of the expressions for the best-estimated predicted values for parameters, responses and their associated best-estimated reduced uncertainties. For large-scale systems, the most efficient method for computing these sensitivities is the adjoint sensitivity procedure (ASAP). Another computationally intensive aspect in the assimilation and calibration methodology presented in Section II is the inversion of the covariance matrix associated with the vector of deviations between the respective computed and experimentally-measured responses. Methods for efficiently inverting of this matrix, as well as for reducing its dimension through "reduced-order modeling" using proper orthogonal decomposition methods are of substantial interest.

Ongoing research is currently devoted to the explicit treatment of modeling errors, and to extending the formulas used in this work by including not only the sensitivities (i.e., first-order information) but also the Hessians (i.e., second-order information) of the responses. Additional work is also ongoing to remove the current restriction to Gaussian distributions. Actually, the de-facto limitation to Gaussian distribution is characteristic of all of the state-of-the-art procedures for data assimilation and model calibration, as evidenced by the scientific literature published thus far. Removing these limitations would contribute significantly to understanding the validation of coupled nonlinear multi-physics models (e.g., of two or more physical phenomena that were not coupled in the initial validation database), particularly the accompanying increase of uncertainty. Developing predictive experimentally validated “best-estimate” numerical models is particularly important for designing new technologies and facilities based on novel processes, while striving to avoid, as much as possible, the costly and lengthy procedures of building representative mock-up experiments, which might confirm - but would not necessarily explain- the predictions of simulation tools.

The costs of “validation, verification, and model calibration through data assimilation” must be weighed against the costs of incorrect or improper decisions based on possibly faulty computational modeling and simulation. Analogous to probabilistic risk assessment activities, risk is typically defined as the product of the probability of the occurrence of the event and the consequence of the event. If erroneous conclusions based on modeling and simulations are made on high-consequence events, decision makers could place their constituency at extreme risk. This is especially true for systems that cannot be tested. For such systems, the only path to progress is to improve drastically the confidence and understanding of computational simulations, while continually relaxing their limitations and enlarging their validation domains.

ACKNOWLEDGMENTS: This work has been partially funded by the EC Commission under the 7th EURATOM Framework Program, within the Integrated and Collaborative Project NURISP "Nuclear Reactor Integrated Simulation Project" under contract 232124 (FI7O), and the Collaborative Project for an European Sodium Fast Reactor (CP-ESFR) .

First of all, I would like to thank to my advisor, Prof. Dr. Dr. h.c. mult. D.G.Cacuci for his immense and constant support, help and advice.

I would also like to thank to Prof. Dr.-Ing E. Schnack for agreeing to be the co-examiner on my dissertation committee.

I wish to express my sincere appreciation to all those who have contributed, directly or indirectly, to this doctoral research through their technical, scientific and other suport. I want to thank all my colleagues in IKR for many fruitful discussions and assistance during this research.

I wish to thank the Dean of Mechanical Engineering, Prof. Dr.-Ing M. Gabi, as well as the faculty council, for allowing me to present my work in English.

Special thanks I want to say to my family and my close friends, who supported me during good or bad times while working on this thesis.

APPENDIX

SUMMARY DESCRIPTION OF THE CORE THERMAL-HYDRAULICS CODE SYSTEM FLICA4

The three-dimensional (3D) two-phase flow code [Fillion et al., 2007, Toumi et al, 2000a, Toumi et al, 2000b, Anyel et al, 2005] models the transient and steady-state thermal-hydraulic phenomena in a reactor core. The two-phase mixture is modeled by a set of four 3D balance equations, expressing the conservation of mass, momentum, and energy of mixture, and mass of vapor respectively. The non-equilibrium of the phase-velocities is modeled by a drift flux correlation. A one-dimensional (1D) model is used to simulate the conduction in solids (fuel). Depending on the fluid, the geometry and operating conditions (e.g. pressure), the user has a choice of closure laws (correlations) for wall friction, drift flux, heat transfer and critical heat flux. The numerical procedure used for solving the conservation equations is a finite volume method, comprising an extension of Roe's approximate Riemann solver for defining convective fluxes, and the VF9 scheme[28][ROOT] for estimating the diffusive fluxes. The forward stepping in time is based on a linearized conservative implicit integrating step together with a Newton iterative method. FLICA4 employs a technological description of the objects (e.g., fuel rods) and an automatic computation of homogenized properties (e.g., hydraulic diameter). The computational mesh is first defined in the radial direction, followed by an extrusion in the axial direction. The FLICA4 code system has been very widely used to model many installations, ranging from the simulation of experimental facilities to the modeling, design, and safety analysis of almost all types of reactors including BWR, PWR, RBMK, VVER.

Physical Model

The two-phase flow model in FLICA4 is based on a Eulerian description of the mixture of liquid and vapor. Thermal and kinematical non-equilibrium between the two phases are modeled by two closure laws. Several sets of closure laws are available for different applications. Although the conservation equations in the FLICA4 code are unrestrictedly 3D, several particular physical models are restricted to a particular direction of flow.

Four-equation model

The mixture mass properties are defined using void fraction and volumetric mass, as follows

$$\chi = \left(\alpha_v \rho_v \chi_v + (1-\alpha_v)\rho_l \chi_l\right)/\rho = \left(\sum_{k=v,l} \alpha_k \rho_k \chi_k\right)/\rho ,$$

where χ denotes any fluid variable while the subscripts l and v are used to denote the "liquid" and "vapor" phases, respectively.

The three balance equations for the mixture are:

Mass: $$\frac{\partial}{\partial t}\rho + div \rho u = 0 ;$$

Momentum: $$\frac{\partial}{\partial t}\rho u + div\left(\sum\left(\rho_k \alpha_k u_k \otimes u_k + \alpha_k \Pi_k\right)\right) = \rho g + \tau ;$$

Energy: $$\frac{\partial}{\partial t}\rho E + div\left(\sum\left(\rho_k \alpha_k u_k E_k - \alpha_k \Pi_k u_k\right) - q\right) = Q_{tot} + \rho u g .$$

In the above conservation equations, E denotes the total energy, Π_k denotes the stress tensor, q denotes the heat flux accounting for molecular and turbulent conductivity, τ denotes the friction force, and Q_{tot} denotes the volumetric source term of thermal power.

The non-equilibrium between phases is modeled by employing:

(i) a balance equation for vapor mass:

$$\frac{\partial}{\partial t}\rho c + div\left(\rho c u_v - K_{cv} grad c\right) = \Gamma ,$$

where K_{cv} is a diffusion coefficient and Γ is the source term (vapor generation on wall Γ_w and evaporation or condensation within the bulk flow Γ_{lv}); and

(ii) a closure law for relative velocity between the two phases $u_r = u_v - u_l$.

In particular, sub-cooled boiling is modeled using the vapor mass conservation equation. The relative velocity is classically defined by a drift flux model. In addition, a second closure law is necessary for energy: the vapor is supposed to remain at saturation in the presence of liquid, except for the particular case of boiling crisis.

Closure laws

In FLICA4 [Fillion et al., 2007], the user can customize the model by selecting each closure relationship (e.g. heat transfer coefficient) and adjusting the respective parameters. The heat transfer between fluid and wall is modeled in FLICA4 to cover several regimes: single-phase liquid, nucleate boiling, film boiling, and single-phase vapor. For the single-phase conditions, the heat transfer coefficient is defined as:

$$H_k = \Phi / \left(T_w - T_K\right),$$

where Φ and T_w are respectively the wall heat flux and the wall temperature. Usually, the correlations define the Nusselt number:

$$Nu = H_k D_h / \lambda_{w,k},$$

where D_h is the hydraulic diameter. Three cases are considered, as follows:

(i) for laminar conditions (Re < 2000), the Nusselt number is constant, and specified by the user,

$$Nu = Nu_{lam};$$

(ii) for turbulent conditions (Re > 5000), the Nusselt number is a function of Reynolds and Prandtl numbers,

$$Nu = \left(Nu_0 + a\, Re^b\, Pr_l^c\right) \cdot \left(\frac{\mu(T_l)}{\mu(T_w)}\right)^d;$$

(iii) for transition between laminar and turbulent conditions, a linear interpolation based on Reynolds number is used.

The Dittus-Boelter correlation uses the following values for the parameters: Nulam = 4.36, $Nu_0 = 0$, $a = 0.023$, $b = 0.8$, $c = 0.4$, $d = 0$. This model is well adapted for axial flow in rod bundle.

For two-phase conditions in nucleate boiling, the wall temperature is assumed to be constant for a given heat flux and pressure:

$$T_w = T_{sat} + \Delta T_{sat}.$$

There are two correlations available in FLICA4, namely:

(a) Jens & Lottes, 1951,

$$\Delta T_{sat} = 7.91 \cdot \frac{\Phi^{0.25}}{10^4} \cdot exp\left(\frac{-P}{62 \cdot 10^5}\right);$$

(b) Forster & Greif, 1958,

$$\Delta T_{sat} = 4.44 \cdot \frac{\Phi^{0.385}}{10^4} \cdot \frac{P^{-0.23}}{10^5}.$$

For Critical Heat Flux (CHF), FLICA4 provides choices of many correlations, including W3[Fillion et al., 2007], [Groeneveld et al., 1996], and [Sudo et.al., 1993]. Beyond CHF, the correlation of [Bishop, Sandberg, and Tong, 1965] is used for film boiling:

$$H = \frac{\lambda_f}{D_h} \cdot 0.0193 \cdot \left(\frac{D_h \cdot G}{\mu_f} \right)^{0.80} \cdot \left(\frac{\mu_f \cdot C_{pf}}{\lambda_f} \right)^{1.23} \cdot \left(\frac{\rho_v}{\rho} \right)^{0.68} \cdot \left(\frac{\rho_v}{\rho_l} \right)^{0.068},$$

where the film temperature is defined by: $T_f = 0.5 \cdot (T_w + T_{sat})$.

Transitions between the conditions mentioned in the foregoing are triggered by the heat flux or the wall temperature, as follow: (a) **liquid convection:** when $T_w < T_{sat} + \Delta T_{sat}$, (b) **nucleate boiling:** when $\Phi < \Phi_{CHF}$, (c) **film boiling**: when $T_w > T_w(CHF)$.

The vapor generation Γ_w on the heated wall is defined as $\Gamma_w = \frac{4\chi\Phi}{D_{heat}L}$, where L denotes the latent heat, and χ denotes the heat flux fraction; $\chi = 0$ means that all the heat flux is used to heat up the liquid (single-phase), while $\chi = 1$ means that the liquid is fully saturated. Between these two extreme conditions, the heat flux fraction is defined from the wall temperature, as follows:

$$\chi = \frac{T_{w,lc} - T_{sat} - \Delta T_{sat}}{T_{w,lc} - T_l - \Delta T_{sat}},$$

where $T_{w,lc}$ is the wall temperature consistent with the heat transfer coefficient for liquid convection.

The interfacial mass transfer, (i.e. condensation or flashing) Γ_{lv} is deduced from the heat transfer between liquid and vapor $\Gamma_{lv} = \frac{\Phi_{lv}}{L}$.

The momentum transfer mainly models the friction on solids, such as fuel rods, plates, or mixing grids. The τ friction force reads:

$$\tau = -\frac{1}{2}\rho u \|u\| \left(\frac{\overline{\overline{\Lambda_w}}}{D_h} + \overline{\overline{K_s}} \right),$$

where $\overline{\overline{\Lambda_w}}$ and $\overline{\overline{K_s}}$ account respectively for the distributed wall friction, and the singular pressure drops. $\overline{\overline{K_s}}$ is provided by the user when defining the geometry, whereas $\overline{\overline{\Lambda_w}}$ is calculated by correlations. For one direction (e.g. *z*) FLICA4 uses a combination of three coefficients: $\Lambda_w^i = f_{iso} \cdot F_w \cdot Y_0$, where f_{iso} is the isothermal friction coefficient, $f_{iso} = a\,Re^{-b}$, and F_w is the correction for wall heating, and Y_0 is the two-phase correction. The coefficients *a* and *b* in f_{iso} depend on the Reynolds number (laminar or turbulent conditions) and on the channel type (tube, rod bundle, etc.).

The stress tensor for viscous and turbulent effects is defined for each phase by:

$$\Pi_k^{ij} = P\delta_{ij} - \mu_k\left(1 + M_k^t\right)\left(\frac{\delta u_k^i}{\delta x_j} + \frac{\delta u_k^j}{\delta x_i} - \frac{2}{3}\frac{\delta u_{kl}}{\delta x_l}\delta_{ij}\right),$$

where $\mu_k M_k^t$ is a turbulent viscosity (*i* and *j* account for the *X*, *Y* and *Z* directions). In practice, the turbulent viscosity is only taken into account for the liquid phase. The standard formulation used for turbulent conditions is $M_l^t = M_0 \cdot \left(Re - Re_t\right)^b \cdot Y_0$, where M_0 is a constant defined by the user.

The relative velocity between vapor and liquid is defined by a correlation for the **slip ratio** $\gamma = \frac{u_v^z}{u_l^z} = f\left(P, \rho_l, ...\right)$, or the **drift flux** $u_v = C_0 \cdot J + u_{v,lim}$, where J is the volumetric velocity and $u_{v.lim}$ is the limit velocity of the vapor when the flow is stagnant. The drift flux models are preferably used since the liquid velocity can be zero or negative. Ishii[25] and Zuber & Findlay[34] models are implemented because they are suitable for many flow conditions, and they can be extended to three-dimensional formulation.

When thermal power boundary conditions are not directly known for the fluid, but only for the fuel elements, the heat conduction in the fuel (rods or plates) is solved in order to compute the source term Q_{tot}. The fuel temperature is obtained from the heat balance equation $\left(\rho c_p\right)_s \delta T_s / \delta t = div\left(\lambda_s \vec{\nabla} T_s\right) + Q_s$, where the solid properties (heat capacity, $(\rho c_p)_s$ and conductivity, λ_s) are defined by the user as function of the solid temperature T_s and the material (e.g. UO_2). The boundary conditions for the heat conduction equation are $T_s = T_w$, at fuel wall, and $\vec{\nabla} T_s \cdot \vec{n} = 0$, at the center of the fuel.

The heat conduction equation is solved in one dimension, assuming that axial conduction is much lower than radial conduction within the fuel element. For transient computations, the wall heat flux and wall temperature are solved implicitly, using the heat transfer coefficient.

In preparation for spatial discretization the two-phase flow equations are written in the form

$$\frac{\partial}{\partial t}U + grad \cdot \left(F\left(U\right) + G\left(U, gradU\right)\right) = S\left(U\right),$$

where U denotes the vector of conservative variables, F and G denote the inviscid (convection) and the viscous flux (diffusion) respectively, and S denotes the source term.

Applying the finite volume method, the two-phase flow equations are integrated over each cell of the chosen spatial mesh, assuming the conservative variables are constant over each individual cell. This integration leads to a system of ordinary differential equations in time, in which the unknowns are the fluxes at each interface between two adjacent cells.

The numerical method developed in FLICA4 for computing the convective fluxes is based on an approximate Riemann solver [Toumi et al, 2000b], requiring the solution of a one-dimensional Riemann problem at each cell interface and uses the characteristics directions within a conservative framework. This method is applicable to any spatial mesh, structured or not, conformal or not. The diffusive fluxes are computing using a VF9-type [Faille, 1992] scheme which is a nine points finite volume technique applicable to either structured or unstructured meshes.

The time discretization of the finite-volume averaged two-phase equations can be performed either explicitly or fully implicitly. Since explicit discretization leads in practice to very small time steps (10s or less), it is not used. The system of nonlinear algebraic equations that results from the implicit time discretization is solved using a Newton method, which ensures the preservations of conservative properties. The convergence of the steady-state calculations is accelerating by employing a procedure of the form $U^{n+1} = U^{n} + \omega \delta U^{n+1}$, where the superscript n denotes the iteration number.

The application of Newton's method in conjunction with the implicit time discretization requires at each time step the solution of a linear system of the form $A\left(U^{n}\right)\delta U^{n+1} = B\left(U^{n}\right)$, where $\delta U^{n+1} = U^{n+1} - U^{n}$. The matrix A is sparse, non-symmetric, and structured in 6x6 blocks (stemming from the 6 conservative scalar variables). Several pre-conditioning techniques are implemented in FLICA4 to allow the use of large time steps, including incomplete decomposition ILU(0) and ILU(1) in conjunction with conjugate gradient square, bi-CGSTAB, and generalized minimal residual methods. Domain decomposition is used with parallel linear solvers for very large problems.

REFERENCES

1. Anyel S. et al., "FLICA4: Status of numerical and physical models and overview of applications", *The 11th International Topical Meeting on Nuclear Thermal-Hydraulics (NURETH-11*), Popes' Palace Conference Center, Avignon, France, October 2-6, 2005.

2. Barhen J, Cacuci D.G. et al, "Uncertainty Analysis of Time-Dependent Nonlinear Systems: Theory and Application to Transient Thermal Hydraulics", *Nucl. Sci. Eng., 81*, 23-44, 1982.

3. Bishop A.A., Sandberg R.O.,Tong L.S., "Forced convection heat transfer high pressure after the critical heat flux", *New York, ASME*, 1965

4. Cacuci, D.G., Sensitivity and Uncertainty Analysis. Theory, *Volume I, Chapman & Hall/CRC,* 2003.

5. Cacuci, D. G. and M. Ionescu-Bujor (2010a),"On the Evaluation of Discrepant Scientific Data with Unrecognized Errors", *Nucl. Sci. Eng., 165,* 1-17, 2010.

6. Cacuci, D.G. and Ionescu-Bujor, M. (2010b), "Best-Estimate Model Calibration and Prediction through Experimental Data Assimilation: Theory", *Nucl. Sci. Eng*., **165**, 18, 2010.

7. Cacuci D. G. , "Sensitivity Theory for Nonlinear Systems: I. Nonlinear Functional Analysis Approach", *J. Math. Phys*., **22**, 2794-2802 , 1981.

8. Cacuci D.G., "Sensitivity Theory for Nonlinear Systems: II. Extensions to Additional Classes of Responses", *J. Math. Phys*., **22**, 2803-2812 ,1981.

9. Cacuci D.G., Navon M.I., and Ionescu-Bujor M., “Computational Methods for Data Analysis and Assimilation,” *Chapman & Hall/CRC*, Boca Raton, 2011.

10. Cacuci D.G. and Ionescu-Bujor M., “Model Calibration and Best-Estimate Prediction Through Experimental Data Assimilation: I. Mathematical Framework”, *Nucl. Sci. Eng,* **165**, 18-44, 2010.

11.Cecchini, U. Farinelli, A.Gandini, and M. Salvatores, A/Conf. 28/, Proc. 3rd Int. Conf. on Peaceful Uses of Atomic Energy, Vol. 2, p. 627, Geneva, 1964.

12 Collier J.G. and Thome J.R., “Convective boiling and condensation”, *third ed. Oxford, Clarendon Press*. 1994.

13. Dragt J.B, et al, “Methods of Adjustment and Error Evaluation of Neutron Capture Cross Sections”, *Nucl. Sci. Eng*., **62**, 117, 1977.

14. Faille, I. “A control volume method to solve an elliptic equation on a two-dimensional irregular meshing” *Computational Methods Applied Mechanical Engineering*, 100, 275–290, 1992.

15. Fillion P.H.et al., “FLICA4: Reference manual of modules and procedures”, *User Guide, Version V1.10.1*, CEA, 2007.

16. E. Forster E. and Greif R., “Heat transfer to a boiling liquid; mechanism and correlations”, *Progress Report 7*, US, 1958.

17. Friedel L, “Improved friction pressure drop correlations for horizontal and vertical two phase pipe flow”, *European Two Phase Flow Group Meeting*, Ispra, 5-8 June 1979.

18. Gandini A and Petilli M, “AMARA: A Code Using the Lagrange Multipliers Method for Nuclear Data Adjustment”, CNEN-RI/FI(73)39, Comitato Nazionale Energia Nucleare, Casaccia/Rome, Italy, 1973.

19. Groeneveld D.G. et al., “The 1995 look-up table for critical heat flux in tubes”, *Nuclear Engineering and Design*, 163, 1–23, 1996.

20. Humi, J.J. Wagcschal, and Y. Yeivin, “Multi-group Constants From Integral Data”, Proc. 3rd Int. Conf. on Peaceful Uses of Atomic Energy, **Vol. 2,** p. 398, Geneva, 1964.

21. Ishii M, “One dimensional drift-flux model and constitutive equations for relative motion between phases in various two-phase flow”, *Technical Report ANL-77-47*, Argonne Nat. Lab., October 1977.

22. Inoue A, Kurosu T, Aoki T, and Yagy M, “Void Fraction Distribution in BWR Fuel Assembly and Evaluation of Sub-channel Code”, *Journal of Nuclear science and Technology, July*, 1995.

23. Kuroi H and Mitani H, “Adjustment to Cross-Section Data to Fit Intregral Experiments by Least Squares Method”, *J. Nuc. Sci. Technology*, **12**, 663, 1975.

24. Lahoz W, Khattatov B., and Ménard R., Editors, “Data Assimilation: Making Sense of Observations”, *Springer Verlag*, 2010.

25. Lewis J. M, Lakshmivarahan S., and. Dhall S.K, “Dynamic Data Assimilation: A Least Square Approach,” *Cambridge University Press*, Cambridge , 2006.

26. Neykov B et al., “NUPEC BWR Full-size Fine-mesh Bundle Test (BFBT) Benchmark, Nuclear Science”, *NEA/NSC/DOC(2005)5, ISBN 92-64-01088-2, NEA No. 6212, OECD* 2006.

27. Petruzzi A, Cacuci D. G., and D’Auria F., “Best-Estimate Model Calibration and Prediction Through Experimental Data Assimilation: Application to a Blowdown Benchmark Experiment”, *Nucl. Sci. Eng*., **165**, 45-100, 2010

28. Rowlands J, et al, “The Production and Performance of the Adjusted Cross-Section Set FGL5”, *Proc. Int. Symposium “Physics of Fast Reactors*”, Tokio, 1973.

29. ROOT: CERN http://www.cern.ch/root

30. Sudo Y and Kaminaga M, “A New CHF Correlation Scheme Proposed for Vertical Rectangular Channels Heated From Both Sides in Nuclear Research Reactors”, *Journal of Heat Transfer, 115*, May, 1993

31. Toumi I et al., "Advanced numerical methods for two-phase flow simulation", *OECD/NEA/CSNI workshop*, Barcelona, 10-13 April, 2000a.

32.Toumi I et al., "FLICA4: a three-dimensional two-phase flow computer code with advanced numerical methods for nuclear applications", *Nuclear Engineering and Design*, 200, 139–155, 2000b.

33 Tong L.S., and Weisman J., . "Thermal analysis of pressurized water reactors", *American Nuclear Society*, 1996

34.TRAC-PF1/MOD2 Theory Manual, Appendix B, Material Properties, *NUREG/CR-5673*, 1993.

35. Usachhev L.N., "Perturbation Theory for the Breeding Ratio and for Other Number Ratios Pertaining to Various Reactor Processes", *J. Nuc. Energy Part A/B*, **18**, 571, 1964.

36 C.R. Weisbin C.R., et al., "Application of Sensitivity and Uncertainty Methodology to Fast Reactor Integral Experiment Analysis", *Nucl. Sci. Eng*., **66**, 307, 1978.

37. Zuber N and Findlay J.A., "Average volumetric concentration in two-phase flow systems", *Journal of Heat Transfer*, 87, 453–468, 1995.